Doctoral Dissertation

Application of Multi-temporal Differential Interferometry SAR to Long-term Monitoring Subsidence in Semarang, Indonesia and Volcanic Deformation in Sakurajima, Japan

（インドネシア・スマランの地盤沈下，および，桜島の火山変形の長期監視に対する時系列差分干渉 SAR の適用に関する研究）

March, 2019

Putu Edi Yastika

Graduate School of Science and Engineering

Yamaguchi University

Summary

Monitoring ground surface displacements related to geological hazards is an important task for understanding their behavior. Geological hazards, in this case, can be land subsidence, landslides, volcanic activity, etc. Displacement monitoring results comprise one type of information among many that is required to assess the stability of the ground, to make countermeasure and mitigation plans, and to reduce the risks in those hazardous areas. A monitoring method that is able to provide the spatial distribution of displacements and its transition over time is highly required. The method should be economical and effective, and able to continuously provide accurate measurement results over extensive areas. Differential Interferometry Synthetic Aperture Radar (DInSAR) has the potential to be a powerful technique that can meet the above demands.

The first objective of this dissertation is to explain how to utilize the DInSAR method for long-term spatio-temporal continuous displacement monitoring. The study aims to overcome the limitation of the SAR satellite lifespan by applying a multi-sensor SAR data set. The hyperbolic method (HM) with multi-temporal DInSAR is employed in this dissertation. Semarang, Indonesia is taken as the research area for the long-term subsidence monitoring.

The second objective of this dissertation is to improve the DInSAR accuracy for practical applications. DInSAR is severely affected by tropospheric delays when applied to areas with a large difference in height of the topography. Two methods to remove tropospheric delays from the multi-temporal DInSAR results are proposed in this dissertation. Sakurajima Volcano in Japan is chosen for this purpose.

Finally, the third objective of this dissertation is to confirm the reliability of the DInSAR method and its characteristic results so that it can be applied to various cases related to geotechnical issues. Therefore, the monitoring results from six different sites, namely, Seoul in South Korea, Denpasar in Indonesia, Mitake in Japan, Sidoarjo mudflow in Indonesia, the Black Sea coast in Bulgaria, and Yabakei in Japan, are presented and discussed.

The dissertation consists of six chapters.

Chapter 1 presents the background and scientific motivation, problem setting, and construction of the dissertation.

Chapter 2 gives outlines of SAR and DInSAR, as well as brief reviews of applications of DInSAR to displacement monitoring.

The three objectives of this dissertation are sequentially discussed in chapters 3, 4, and 5. A summary of each chapter is given below.

Chapter 3 discusses the application of multi-temporal DInSAR for long-term subsidence monitoring in Semarang, Indonesia. Land subsidence is a critical issue that large cities located in coastal areas, such as Semarang, must address. The monitoring of land subsidence is vital for predicting and mitigating the disasters that such subsidence may cause. DInSAR has been applied to monitor the subsidence in Semarang, but it was only for a limited period before 2012. In order to clarify the transition of the long-term subsidence behavior in Semarang, the Small Baseline Subset (SBAS) method, which is one type of multi-temporal DInSAR, is employed in this research. Sets of data from Envisat-ASAR (2003-2007), ALOS-PALSAR (2007-2011), and Sentinel-1A (2015-2017) are utilized for the analyses. Then, the validity of the SBAS results is discussed from the viewpoints of both spatial distribution and temporal transition using GPS displacement measurement results and the geological conditions of the ground. On the other hand, as the lifespan of SAR satellites is commonly designed to be around 5-7 years, an appropriate method, which can connect the subsidence provided independently by the unlinked time-series data sets of the three different SAR satellite data, is required. This study uses the hyperbolic method (HM) to connect the above unlinked SBAS results. The HM is often used in practice as a geotechnical tool to fit the monitored subsidence. The temporal behavior of the subsidence in Semarang, monitored over a period of 14 years, is evaluated with this method. It is found that the transition of the subsidence differs depending on the location, and that the subsidence rate is still increasing in the north and northeast parts of the coastal area. This study shows that SBAS DInSAR can be a useful tool for long-term continuous subsidence monitoring.

Chapter 4 discusses the application of multi-temporal DInSAR for deformation monitoring induced by the volcanic activity of Sakurajima Volcano in Japan. Monitoring the deformation due to volcanic activity is important for understanding volcanic behavior. The Global Navigation Satellite System (GNSS) is sometimes used for such purposes. However, the system requires the installation of sensors at the site, and the installation and maintenance of these sensors are usually difficult and dangerous when volcanoes in the area are very active. On the other hand, DInSAR can be used to measure the surface deformation of volcanoes without the installation of any devices on the ground. Moreover, the time-series DInSAR analysis has the potential to reveal

the deformation behavior of volcanoes at the pre- and post-eruption stages. However, the DInSAR results can be greatly affected by the temporal variation in the refractivity of the tropospheric layer, especially when there are large differences in height in the target area of the measurements. Although it is a fundamental issue of DInSAR, it is still difficult and there are only a few methods for removing the errors caused by the tropospheric delays of radar pulse waves. The present dissertation discusses this issue and the proposal of two simple methods for improving the measurement accuracy. The proposed methods were applied and the ground surface deformation was observed for three years, from November 2014 to August 2017, by a time-series DInSAR analysis using Sentinel-1 data (operated by the European Space Agency). In this way, the effect of the tropospheric delays was successfully reduced.

Chapter 5 addresses the various applications of SBAS DInSAR to six different study sites. The size of the sites varies, from a large megapolitan city, Seoul, South Korea, to a local slope in Yabakei, Japan. Also, the ground conditions and factors that lead to ground deformation are different for each site. This variation creates different challenges when employing SBAS DInSAR. The application of SBAS DInSAR for long-term displacement monitoring is found to be very useful. However, there are some limitations, such as the size and geometry of the monitoring area and the vegetation that covers the site. The issues that are raised in this chapter may comprise a future work related to this research.

Chapter 6 provides a summary of the conclusions to this research and ideas on the future role of multi-temporal DInSAR.

Preface

This dissertation is hereby submitted to the Graduate School of Science and Engineering of Yamaguchi University, Japan in partial fulfillment of the requirements for the degree of Doctor of Engineering. The manuscript is an original contribution by the author, except where references are made to previous studies. The publications written by the author during his doctoral studies are listed below; they correspond to different chapters of this dissertation.

1. Peer-reviewed journal article

   a. **Yastika, P.E.,** Shimizu, N., Abidin, H.Z., 2019. Monitoring of long-term land subsidence from 2003 to 2007 in coastal area of Semarang, Indonesia by SBAS DInSAR analyses using Envisat-ASAR, ALOS-PALSAR, and Sentinel-1A SAR data. Advances in Space Research, 63, pp. 1719-1736. (https://doi.org/10.1016/j.asr.2018.11.008).

   This journal article summarizes our study on subsidence monitoring in Semarang. The procedure for long-term subsidence monitoring by multi-temporal DInSAR, incorporating the hyperbolic method, is fully discussed in it. Thus, the article is the main part of chapter 3 of this dissertation.

2. Peer-reviewed proceedings papers

   a. **Yastika, P.E,** Shimizu, N., 2016. Monitoring deformation of ground surface over extensive area by multi-temporal DInSAR. Rock Mechanics and Rock Engineering: From the Past to the Future, 2, pp. 1219-1224.

   This paper is part of chapter 3. The idea of bridging the fields of remote sensing and geotechnical engineering first appeared in this paper. It was presented by the co-author at the 2016 ISRM (International Society for Rock Mechanics and Rock Engineering) International Symposium (EUROCK 2016), Cappadocia, Turkey, August 2016.

   b. **Yastika, P.E.,** T. Ibara, N. Shimizu, N. Iwata, Y. Takahashi., Y. Araki., 2018. Application of DInSAR for monitoring the ground deformation due to volcanic activity: a case study of Sakurajima, Japan. Proceedings of 10th Asian Rock Mechanics Symposium.

   This paper is the main part of chapter 4 of this dissertation. Two methods for tropospheric delay correction are proposed in this paper. It was presented by the

first author at the 10th Asian Rock Mechanics Symposium, Singapore, October 2018, held as the Regional Symposium of ISRM.

3. Proceedings papers not yet reviewed

    a. **Yastika, P.E.,** Shimizu, N., 2016. Applications of DInSAR for ground surface deformation measurements - case studies of subsidence measurements and deformation detections due to an earthquake. Proceedings of the 37th West Japan Symposium on Rock Engineering, pp. 91-97.

    Part of this paper is part of chapter 3 of this dissertation. It was presented by the first author at the 37th West Japan Symposium on Rock Engineering, Ube, Japan, September 2016. The aim of this paper was to introduce the DInSAR application to the rock engineers attending the symposium.

    b. **Yastika, P.E.,** Shimizu, N., 2017. Discussions on procedure of long-term land subsidence monitoring by multi-temporal DInSAR. Proceedings of the 2017 ISRM Young Scholars' Symposium on Rock Mechanics (YSRM 2017 – an ISRM Specialized Conference) and the 2017 International Symposium on New Developments in Rock Mechanics and Geotechnical Engineering (NDRMGE 2017), pp. 172-175.

    *This paper discusses the procedure of multi-temporal DInSAR for long-term monitoring of subsidence and is part of chapter 3 of this dissertation. This paper was presented by the first author at the 2017 International Symposium on New Developments in Rock Mechanics and Geotechnical Engineering (NDRMGE 2017), Jeju, South Korea May 2017. At the conference, the first author was awarded a prize for "**YSRM Outstanding Oral Presentation**". The first author was one of only two participants to receive the award, and he was the only Asian participant to receive the award.*

4. Extended abstract

    a. **Putu Edi Yastika**, Norikazu Shimizu, 2018. Long-term monitoring of subsidence in Semarang by using SBAS DInSAR. The 73rd Annual Conference of the Japan Society of Civil Engineers.

    *This extended abstract is part of chapter 3 of this dissertation. It was presented by the first author at the 73rd Annual Conference of the Japan Society of Civil, Sapporo, Japan, August 2018. The first author received the "**Excellent Presentation Award**" from the awarding committees of that conference.*

Acknowledgments

Ube, March 2019

Author

Table of contents

List of Figures

List of Tables

List of Acronyms

ALOS   : Advanced Land Observation Satellite
ASAR   : Advanced Synthetic Aperture Radar
AT-InSAR   : Along Track-InSAR
APS   : Atmospheric Phase Screen
BPS   : Badan Pusat Statistik
CT-InSAR   : Cross Track-InSAR
CVM1   : Correction Value of Method1
CVM2   : Correction Value of Method2
DEM   : Digital Elevation Model
DInSAR   : Differential Interferometry SAR
Envisat   : Environmental Satellite
ERS   : European Remote Sensing
ESA   : European Space Agency
GCP   : Ground Control Point
GNSS   : Global Navigation Satellite System
GPS   : Global Positioning System
GSI   : Geospatial Information Authority of Japan
HM   : Hyperbolic method
InSAR   : Interferometry SAR
IQ   : In-Phase and Quadrature
JERS-1   : Japanese Earth Resources Satellite-1
JMA   : Japan Meteorological Agency
JPL   : Jet Propulsion Laboratory
LOS   : Line of Sight
NASA   : National Aeronautics and Space Administration
PALSAR   : Phased Array type L-band Synthetic Aperture Radar
PSI   : Permanent Scatterer Interferometry
SAR   : Synthetic Aperture Radar
SBAS   : Small Baseline Subset
SIR-C   : Spaceborne Imaging Radar-C
SLC   : Single Look Complex
SPN   : Stable Point Network
SRTM3   : Shuttle Radar Topography Mission 3
ZTD   : Zenith Tropospheric Delay

List of Symbols

A	: Amplitude
B	: SBAS matrix B
C	: Speed of light
τ	: Radar pulse width
Δx	: Ground range resolution
ΔR	: Slant range resolution
H	: Satellite altitude
θ	: SAR look angle
L	: Antenna length
Ls	: Synthetic aperture length
W	: Illumination width
β	: Radar beam width
β_s	: Synthetic Radar beam width
R	: Slant range distance
ΔR_a	: Azimuth resolution
λ	: Wavelength
v	: Velocity
y	: SLC data
e	: Irrational number (Euler's number)
φ	: Phase
ϕ	: Phase angle
B	: Geometrical baseline
$B_\perp$	: Perpendicular baseline
B_c	: Critical perpendicular baseline
Z	: Elevation of the ground
α	: Angle between the baseline and the horizontal plane
d	: LOS displacement
$\Delta\varphi_{disp}$	: Phase difference due to displacement
$\Delta\varphi_{topo}$	: Phase difference due to residual topography

$\Delta\varphi_{orb}$	: Phase difference due to orbit inaccuracy
$\Delta\varphi_{atm}$	: Phase contribution due to the atmospheric artifacts
$\Delta\varphi_{scatt}$	: Phase contribute by changes in scattering behavior
$\Delta\varphi_{noise}$	: Phase noises
N	: Number of SAR data
M	: Number of Interferograms
M	: SBAS matrix M
t	: Time
S	: Subsidence
S_f	: Subsidence at final time
S_{ti}	: Subsidence at time i
θ_i	: Incident angle
α	: HM parameter
β	: HM parameter
h	: Ground elevation

Chapter 1

Introduction

1.1 Background and scientific motivation

Monitoring ground surface displacements that are related to geological hazards is an important task for understanding their behavior. Geological hazards, in this case, can be land subsidence, landslides, and/or volcanic activity. Displacement monitoring results comprise one type of information among many that is required to assess the stability of the ground and then to make countermeasure and mitigation plans in order to reduce the risks in those hazardous areas. A monitoring method that is able to provide the spatial distribution of displacements and its transition over time, and to continuously monitor narrow to extensive areas with high accuracy, is highly required. Additionally, it should be low in cost and easy to handle (Shimizu, 2016).

Many monitoring methods and instruments have been used in the geotechnical field. Those monitoring methods and instruments have proven their ability to provide accurate measurement results. However, they can only be applied to limited areas. Therefore, they are not adequate for monitoring vast areas such as large slopes and large volcanoes. On the one hand, modern satellite technologies, i.e., GPS (Global Positioning System) and SAR (Synthetic Aperture Radar), can overcome the above problem. GPS and SAR have begun to be used for monitoring deformation over extensive areas in the last few decades. One suggested monitoring method using GPS has proven its ability to provide continuous measurement results over the area within 1 km square with mm-order accuracy (Shimizu et al., 2014). However, it requires the installation of devices on the ground. On the other hand, the SAR with Differential Interferometry SAR (DInSAR) method is an attractive tool which does not require any devices on the ground. However, its accuracy is less than that of GPS. Thus, the accuracy of DInSAR needs to be improved to enable its practical application.

Long-term displacement monitoring using multi-temporal DInSAR has been applied for many cases, such as subsidence, volcanoes, landslides, infrastructures, etc. Long-term subsidence monitoring can lead to a better understanding of their behavior including the effects of land use (Du et al., 2018; Minderhoud et al., 2018). Subsidence monitoring has also been extended to mining areas. Research has been conducted for monitoring at several mines (Da Lio et al., 2018; Gonnuru and Kumar, 2018; Ng et al., 2017) and the results were found to be very useful.

Comparing the measurement epochs of GPS and DInSAR, GPS is seen to provide shorter measurement intervals than DInSAR. The measurement intervals of DInSAR rely on the revisiting time of the SAR satellites. That time is in the range of a few days to a few months. In addition, the lifespan of SAR satellites is usually designed to be 5-7 years as opposed to GPS satellites which can last for more than 10 years and work as a constellation consisting of dozens of units. Therefore, the lifespan of SAR satellites is another limitation to their application with DInSAR to long-term displacement monitoring. Thus, monitoring for longer periods should be conducted by employing a multi-sensor SAR data set. Utilization of multi-sensor data has been conducted by Kim et al. (2015) and Liu et al. (2018). However, problems occurred when there were no SAR data from the multi-sensor SAR data set. This means that there was a gap of time for which no SAR data existed.

These two limitations, namely, the accuracy of DInSAR and the lifespan of the SAR satellites, are the remaining issues to be solved for the practical use of the SAR with DInSAR method for long-term monitoring.

Motivated by the above-mentioned background, the main focus of this dissertation is to discuss how to utilize the DInSAR method for practical long-term displacement monitoring. This study aims to overcome the limitations of the SAR satellite lifespan by employing a multi-sensor SAR data set. The hyperbolic method (HM) with multi-temporal DInSAR is utilized in this dissertation. Semarang, Indonesia is taken as the research area for this study on long-term subsidence monitoring.

In addition, the improvement of the DInSAR accuracy is a key issue for practical applications. DInSAR is severely affected by tropospheric delays when applied to areas with rugged topography such as volcanoes. Some methods have been proposed to deal with these issues (Bekaert et al., 2015; Doin et al., 2009; Jolivet et al., 2011). However, problems with its practical application still remain. Two methods to remove the tropospheric delays from DInSAR results are also proposed in this dissertation. Sakurajima Volcano in Japan is chosen for this purpose. In the end, it is necessary to know the reliability of DInSAR methods and the characteristics of the results in order to apply them to various geotechnical issues. Therefore, the monitoring results over six different sites, namely, Seoul in South Korea, Denpasar in Indonesia, Mitake in Japan, Sidoarjo mudflow in Indonesia, Black Sea coast in Bulgaria, and Yabakei in Japan are also presented.

1.2 Formulation of problems

Based on the previously stated background and scientific motivation, the questions raised in this study are as follows:

1. How can long-term subsidence monitoring be conducted with multi-temporal DInSAR and a multi-sensor SAR data set?
2. How is the present behavior of the subsidence in Semarang monitored by multi-temporal DInSAR?
3. How do tropospheric delays affect the multi-temporal DInSAR results and how can they be corrected?
4. How is the behavior of the ground surface displacement of Sakurajima Volcano monitored by multi-temporal DInSAR?
5. What are the characteristics of the monitoring results obtained by multi-temporal DInSAR from various monitoring areas, and what are their limitations and challenges?

1.3 Structure of dissertation

This dissertation consists of six chapters. Chapter 1 presents the background and scientific motivation, problem setting, and construction of the dissertation. A short explanation of the basic theory behind SAR and related methods of displacement monitoring using SAR data, i.e., SAR interferometry, are presented in chapter 2. The recent applications of SAR interferometry for displacement monitoring are also briefly reviewed in this chapter.

Chapter 3 provides the application of multi-temporal DInSAR for long-term subsidence monitoring. Three different SAR data sets are used, and the hyperbolic method is employed to connect the unlinked periods of SAR data. The hyperbolic method is also used to characterize the subsidence behavior in Semarang. The subsidence in Semarang is then discussed by considering the geological conditions existing there. Chapter 4 proposes two methods for the correction of the tropospheric delays in multi-temporal DInSAR (SBAS) results. Multi-temporal DInSAR with the proposed methods were applied to Sakurajima Volcano, Japan. The application of multi-temporal DInSAR is extended to six other sites which are facing geotechnical issues. These applications are presented in chapter 5. Finally, the findings and the conclusions of this dissertation, along with ideas on the future role of multi-temporal DInSAR, are presented in chapter 6.

References

Bekaert, D.P.S., Walters, R.J., Wright, T.J., Hooper, A.J., Parker, D.J., 2015. Statistical comparison of InSAR tropospheric correction techniques. Remote Sens. Environ. 170, 40–47. https://doi.org/10.1016/j.rse.2015.08.035

Da Lio, C., Teatini, P., Strozzi, T., Tosi, L., 2018. Understanding land subsidence in salt marshes of the Venice Lagoon from SAR Interferometry and ground-based investigations. Remote Sens. Environ. 205, 56–70. https://doi.org/10.1016/j.rse.2017.11.016

Doin, M.P., Lasserre, C., Peltzer, G., Cavalié, O., Doubre, C., 2009. Corrections of stratified tropospheric delays in SAR interferometry: Validation with global atmospheric models. J. Appl. Geophys. 69, 35–50. https://doi.org/10.1016/j.jappgeo.2009.03.010

Du, Z., Ge, L., Ng, A.H.-M., Zhu, Q., Yang, X., Li, L., 2018. Correlating the subsidence pattern and land use in Bandung, Indonesia with both Sentinel-1/2 and ALOS-2 satellite images. Int. J. Appl. Earth Obs. Geoinf. 67, 54–68. https://doi.org/10.1016/j.jag.2018.01.001

Gonnuru, P., Kumar, S., 2018. PsInSAR based land subsidence estimation of Burgan oil field using TerraSAR-X data. Remote Sens. Appl. Soc. Environ. 9, 17–25. https://doi.org/10.1016/j.rsase.2017.11.003

Jolivet, R., Grandin, R., Lasserre, C., Doin, M.P., Peltzer, G., 2011. Systematic InSAR tropospheric phase delay corrections from global meteorological reanalysis data. Geophys. Res. Lett. 38, 1–6. https://doi.org/10.1029/2011GL048757

Kim, J.W., Lu, Z., Jia, Y., Shum, C.K., 2015. Ground subsidence in Tucson, Arizona, monitored by time-series analysis using multi-sensor InSAR datasets from 1993 to 2011. ISPRS J. Photogramm. Remote Sens. 107, 126–141. https://doi.org/10.1016/j.isprsjprs.2015.03.013

Liu, Y., Zhao, C., Zhang, Q., Yang, C., Zhang, J., 2018. Land Subsidence in Taiyuan, China, Monitored by InSAR Technique With Multisensor SAR Datasets From 1992 to 2015. IEEE J. Sel. Top. Appl. Earth Obs. Remote Sens. 11, 1–11. https://doi.org/10.1109/JSTARS.2018.2802702

Minderhoud, P.S.J., Coumou, L., Erban, L.E., Middelkoop, H., Stouthamer, E., Addink, E.A., 2018. The relation between land use and subsidence in the Vietnamese Mekong delta. Sci. Total Environ. 634, 715–726. https://doi.org/10.1016/j.scitotenv.2018.03.372

Ng, A.H.-M., Ge, L., Du, Z., Wang, S., Ma, C., 2017. Satellite radar interferometry for monitoring subsidence induced by longwall mining activity using Radarsat-2, Sentinel-1 and ALOS-2 data. Int. J. Appl. Earth Obs. Geoinf. 61, 92–103. https://doi.org/10.1016/j.jag.2017.05.009

Shimizu, N., Nakashima, S., Masunari, T., 2014. ISRM suggested method for monitoring rock displacements using the global positioning system (GPS). Rock Mech. Rock Eng. 47, 313–328. https://doi.org/10.1007/s00603-013-0521-5

Shimizu, N., 2016. Challenge of continuous spatio-temporal displacement monitoring in geotechnical engineering. Proc. of VARAZDIN2016 -7th Conference of Croatian Geotechnical Society.2016, 13-23.

Chapter 2

Basic theory and methodology

2.1 Brief history and development of SAR

"SAR" is the acronym for Synthetic Aperture Radar; it is a radar device mounted on an aircraft or artificial satellite that generates high-resolution remote sensing imagery all day and all night (Hanssen, 2001). SAR is one type of active remote sensing that uses microwave radiation with wavelengths from about one centimeter to a few tens of centimeters enabling observations in all weather conditions. This is an advantage that is not possible with visible and/or infrared remote sensing. However, the need for sophisticated data analysis is the disadvantage of using microwave remote sensing. Radar bands and designations are presented in Table 2.1. The most commonly used bands for radar remote sensing are marked by an asterisk (*) in the table (Lusch, 1999).

Table 2.1 Frequency and wavelength of microwave bands (Lusch, 1999).

Band Designation	Wavelength range (cm)	Frequency range (GHz)
Ka	$0.75 - 1.10$	$40.0 - 26.5$
K	$1.10 - 1.67$	$26.5 - 18.0$
Ku	$1.67 - 2.40$	$18.0 - 12.5$
X*	$2.40 - 3.75$	$12.5 - 8.0$
C*	$3.75 - 7.50$	$8.0 - 4.0$
S	$7.50 - 15.0$	$4.0 - 2.0$
L*	$15.0 - 30.0$	$2.0 - 1.0$
P	$30.0 - 130.0$	$1.0 - 0.23$

The SAR system was invented in 1953 by Carl Wiley and then developed for fine resolution mapping and other remote sensing applications. Table 2.2 shows the highlights of SAR history.

Table 2.2 Highlights of SAR history (Apel and Jackson, 2004) and some added developments from 1990's-present.

Year	Development
1951	Carl Wiley of Goodyear postulates the Doppler beam-sharpening concept.
1952	University of Illinois demonstrates the beam-sharpening concept.
1957	University of Michigan produces the first SAR imagery using an optical correlator.
1964	Analog electronic SAR correlation demonstrated in non-real time (University of Michigan).

Table 2.2 (continued)

1969	Digital electronic SAR demonstrated in non-real time (Hughes, Goodyear, Westinghouse).
1972	Real-time digital SAR demonstrated with motion compensation (for aircraft systems).
1978	First space-borne SAR NASA/JPL SEASAT satellite. Analog downlink; optical and non-real-time digital processing.
1981	Shuttle Imaging Radar series starts-SIR-A. Non-real-time optical processing on ground.
1984	SIR-B digital downlink; non-real-time digital processing on ground.
1986	Space-borne SAR Real-time processing demonstration using JPL Advanced Digital SAR processor (ADSP)
1987	Soviet 1870 SAR is placed in earth orbit.
1990	Magellan SAR image Venus.
1990-present	Evolution of SAR begins in space (excluding the military reconnaissance satellites); Soviet ALMAZ (1991), European ERS-1 (1991), Japanese JERS-1 (1992), SIR-C (1994), ERS-2 (1995), Canadian RADARSAT-1 (1995), SRTM (2000), ENVISAT (2002), Japanese ALOS (2006), Chinese Yaogan-1 (2006), Italia COSMO-Skymed 2007, Germany TerraSAR-X 2007, India RISAT-1 (2009), South Korea KOMSAT-5 (2013), Japanese ALOS-2 (2014), Sentinel-1A (2014), Sentinel-1B(2016)

The development of SAR Earth Observation (EO) satellites began in 1978. The first civilian space-borne SAR was SEASAT (USA) in 1978, followed by Almaz (USSR/Russia), ERS-1 (Europe), JERS-1 (Japan), ERS-2 (Europe), and RADARSAT-1 (Canada). Nowadays, there are many satellites orbiting the Earth carrying radar sensors on board. These satellites provide incredible amounts of data for studying the Earth.

SAR sensors carried by satellites in polar orbits generally make right-looking observations, except for ALOS2, which can be controlled to make either right- or left-looking observations. Given the orbital inclination, these side-looking sensors can image the North Pole (actually an area within a few square kilometers of it), but not the South Pole (unless the satellite is overturned) (Henri, 2008).

All satellites equipped with SAR sensors orbit the earth on a near-polar orbit at an altitude ranging from 500 to 800 km above the Earth's surface, depending on the satellite platform hosting the SAR sensor. The angle between true north-south and the satellite orbit varies slightly, depending on the satellite, but it generally lies in the range of 10 degrees.

2.2 Basic concepts and image formation of SAR

2.2.1 Observation geometry and overview of SAR theory

Figure 2.1 depicts the configuration of the side-looking radar. The antenna is mounted on a platform (usually an aircraft or satellite) moving with a velocity (v) with respect to the Earth at a constant altitude; the flight direction is generally called azimuth. The radar illuminates along the direction perpendicular to the flight path, the slant range, with an inclination (look angle) with respect to the vertical.

1. Off-nadir angle
2. Depression angle
3. Range beam width
4. Incidence angle
5. Azimuth beam width
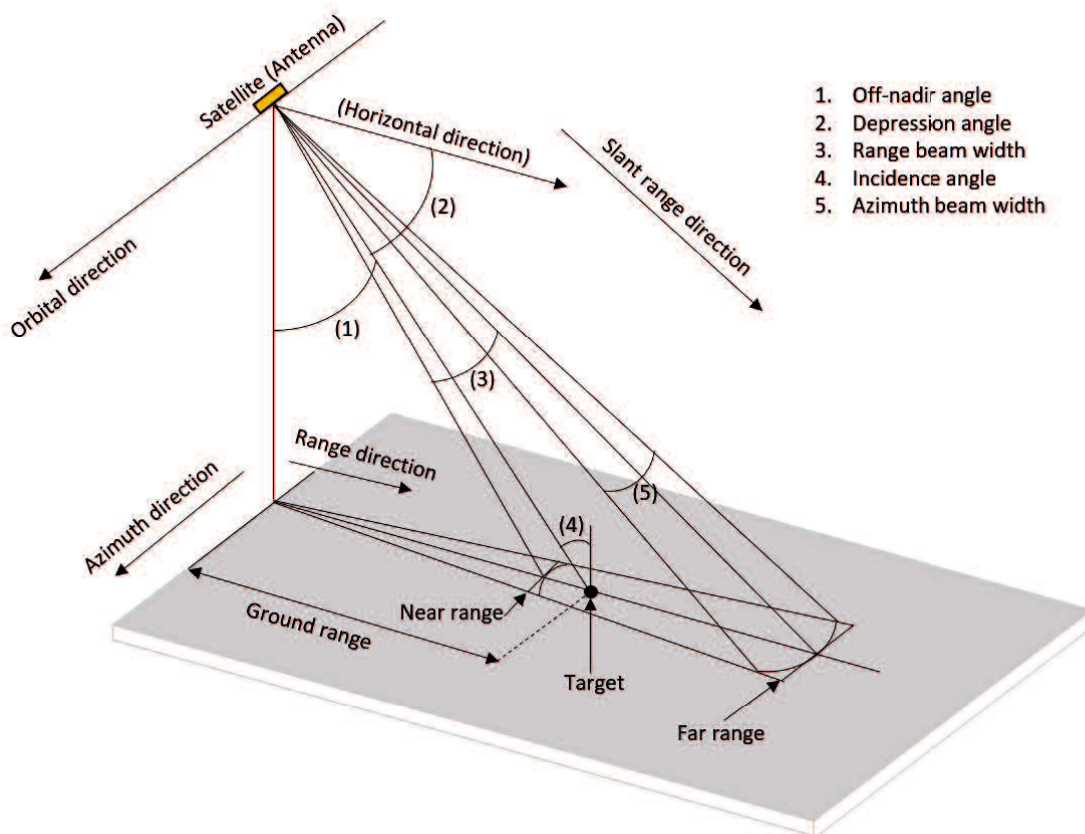
Figure 2.1 SAR geometry (Restec, 2014).

In order for a radar system to make an image based on the echoes it receives, it requires knowledge of two things, namely, where each echo came from on the ground and how bright each echo should be in the image. Figure 2.2 shows an illustration of the principles of SAR for radar imagery. An antenna emits the microwave energy to the target, and the backscatter (echo) from the target will be received. Since the antenna is side-looking, there is a difference in time acquisition between the far range and the near range. The energy backscatter received by the antenna will vary depending on the properties of the target. High backscattered energy yields bright pixels in the image, and vice versa.
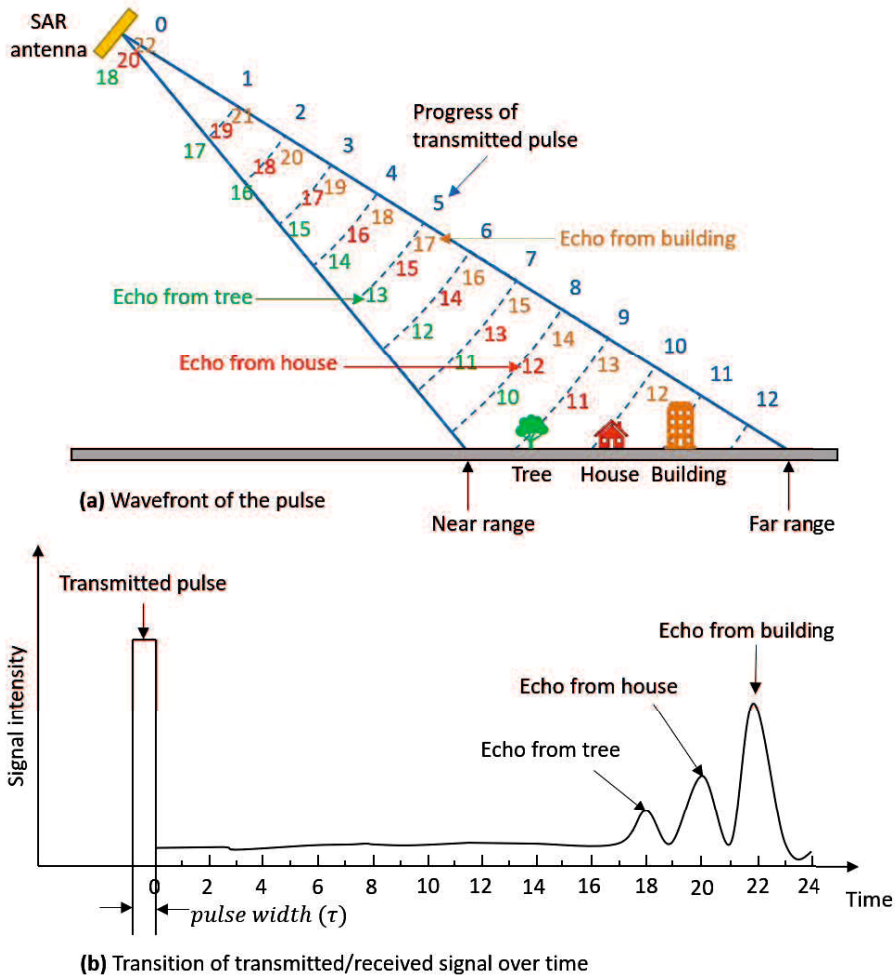
Figure 2.2 Illustration of how SAR works to make radar imagery (Restec, 2014).

2.2.2 Geometric resolution of SAR

Simply speaking, the geometric resolution is the ability of a system to localize nearby objects. More precisely, the resolution length is the minimum spacing between two objects that are detected as separate entities, and are therefore resolved (Franceschetti and Lanari, 2000). In the SAR system, the term "range resolution" and "azimuth resolution" are introduced.

The range resolution of SAR is determined by the built-in radar and the processor constraints which act in the slant range domain. The radar emits short pulses that reflect off the surface of the Earth and return to the antenna. The amplitude versus return time of each pulse is recorded as the reflectivity of the surface. If adjacent reflectors appear as two distinct peaks in the return waveform, then they can be distinguished in the SAR image (see Figure 2.2). This is because they will be in different pixels of the SAR image. If the distance between them is less than $\frac{c\tau}{2}$, they will not be distinguishable in the SAR image.

The relationship between the ground range resolution (Δx) and the slant range resolution (ΔR) is expressed as $R = \dfrac{C\tau}{2\sin\theta}$, where θ is the SAR look angle, τ is the pulse width, and C is the speed of light. The factor of the two accounts for the 2-way travel time of the pulse. Figure 2.3 shows how the ground range resolution is geometrically related to the slant range resolution.
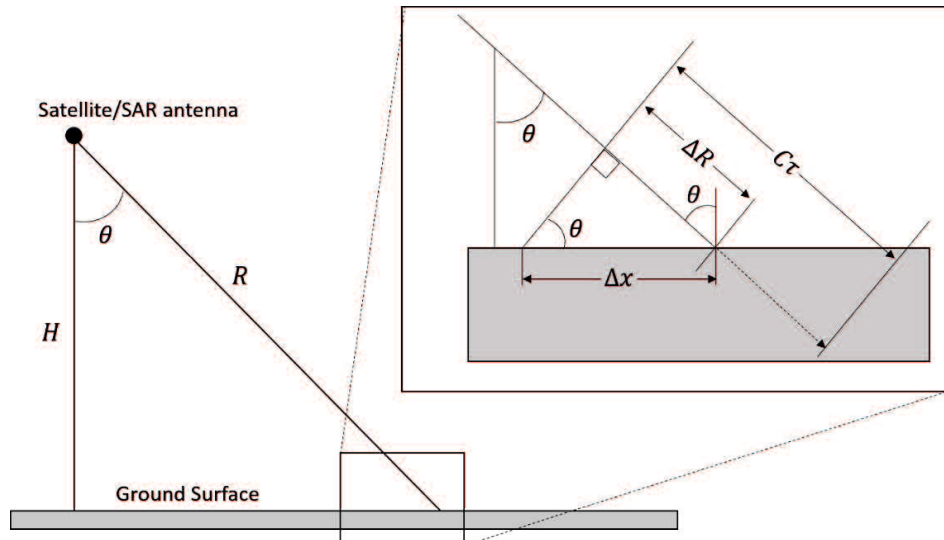
Figure 2.3 Relationship between ground range resolution Δx and slant range resolution (ΔR). The distance (height) of the spacecraft from the ground surface is represented as H (modified from Curlander and McDonough, 1991).

From Figure 2.3, it is seen that the range resolution is independent of the height of the spacecraft, H. It should be noted that the ground range resolution is infinite when the look angle is zero and improves as the look angle is increased. The range resolution can be improved by increasing the bandwidth of the radar. Usually, the radar bandwidth is a small fraction of the carrier frequency. Thus, a shorter wavelength radar does not necessarily enable a higher range resolution. In many cases, the bandwidth of the radar is limited by the speed at which the data can be transmitted from the satellite to a ground station (Sandwell et al., 2011).

For real aperture radar, the azimuth resolution is determined by the angular beam width of the terrain strip illuminated by the radar beam. For two objects to be resolved, they must be separated in the azimuth direction by a distance greater than the width of the beam on the ground. SAR gets its name from azimuth processing and can achieve an azimuth resolution which may be hundreds of times smaller than the width of the transmitted antenna beam. To understand the azimuth resolution, a single point reflector (P) on the ground, that is illuminated as the radar passes overhead, should be considered (Figure 2.4).
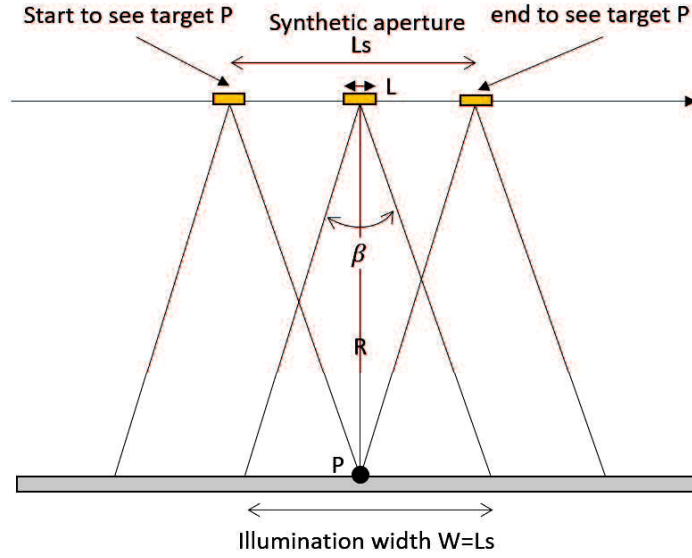
Figure 2.4 Top views of SAR antenna imaging point reflector P. The reflector remains within the illumination pattern over the real aperture length of W (Sandwell et al., 2011).

Considering an antenna with length L, the beam width of the real aperture is given by Eq. (2.1).

$$\beta = \frac{\lambda}{L} \qquad (2.1)$$

where β is the beam width and λ is the wavelength. Thus, the illumination of real aperture W is given by

$$W = \beta R = \frac{\lambda R}{L} \qquad (2.2)$$

Since the length of the synthetic aperture is $L_s = W$, the beam width of the synthetic aperture (Ls) is expressed as

$$\beta_s = \frac{\lambda}{2L_s} \qquad (2.3)$$

Counting the phase difference two times, to and from the satellites, the spatial resolution in the azimuth direction, ΔR_a, can be written as follows:

$$\Delta R_a = \beta_s R \qquad (2.4)$$

Substituting Eq. (2.3) into Eq. (2.4) yields

$$\Delta R_a = \frac{\lambda}{2L_s} R = \frac{L}{2} \qquad (2.5)$$

The maximum spatial resolution in the azimuth direction is L/2; it is independent of the distance and the wavelength.

The final output of the SAR data processing is a SAR image that can be seen as a mosaic of small picture elements (pixels). Each pixel corresponds to a small area of the Earth's surface that can be defined as a resolution cell. Each pixel contains a complex number that carries amplitude and

phase information about the microwave field backscattered by all objects in corresponding resolution cells projected on the ground. These kinds of information are stored in a complex format by adapting the IQ (In-phase and Quadrature) data format. Therefore, the SAR image is also known as a single look complex (SLC) that is composed of a regular grid with complex values or phasors (Hanssen, 2001) and can be decomposed into amplitude (A) or real (R) and phase (φ) or imaginer (I) components, as expressed in the following equation:

$$y = Ae^{j\phi} \tag{2.6}$$

where y is the SLC that represents the electric field of a plane electromagnetic wave, A is the amplitude of the electromagnetic pulse, and ϕ is the phase angle. The amplitude represents the amount of electromagnetic field scattered back by the radar targets grouped in each SAR image-sampling cell or pixel, whereas the phase angle represents an ambiguous measure of the distance between the sensor and each area on the ground corresponding to an image pixel (Raucoules et al., 2007).

2.2.3 Characteristic and geometrical effects in SAR images

Since it is side looking, SAR is limited by the presence of geometric distortion to the range imaging mode (Franceschetti and Lanari, 2000) These effects are demonstrated in Figure 2.5 where SAR imaging along the range direction is shown.
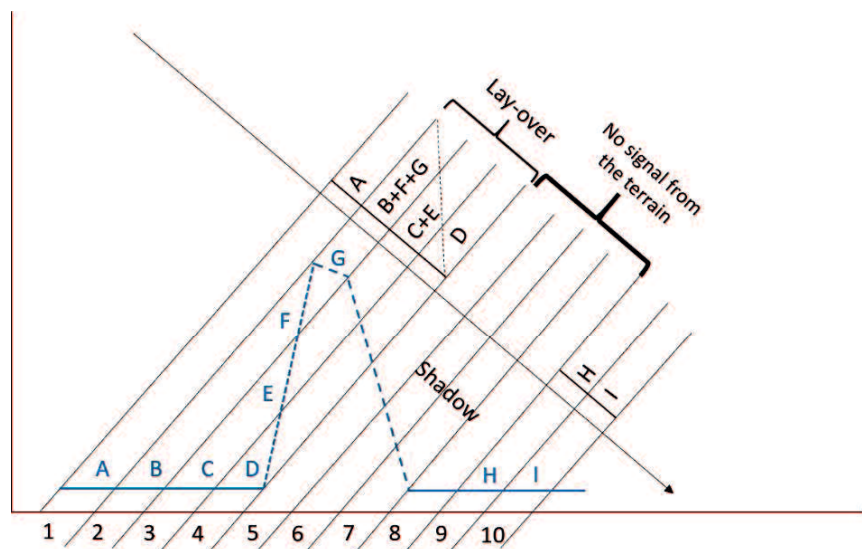
Figure 2.5 Schematic illustration showing how mountainous terrain can create noise through layover and shadow effects (Farretti et al., 2007).

When the terrain slope exceeds the radar local incidence angle, the scatters are imaged in reverse order and superimposed on the contribution coming from other areas. In this case, the top

of the feature will be displaced, or "laid over", relative to its base when it is processed into an image. In Figure 2.5, cell numbers 2, 3, and 4 show examples of layovers. Reflections B, F, and G, coming from parts of the ground, are all superimposed on top of each other in cell number 2. Cell numbers 3 and 4 show the same pattern. In general, the layover is more prevalent for viewing geometries with small incident angles, such as from satellites.

When an object in a scene blocks the radar wave from reaching other portions of the scene, shadows occur in the SAR imagery, as shown in cell numbers 5, 6, 7, and 8 in Figure 2.5. Radar shadows in SAR imagery indicate areas on the ground surface that are not illuminated by the radar. Since no return signals are received, the radar shadows appear to be very dark in tone on the imagery. Radar shadows occur in the down-range direction behind tall objects. They are a good indicator of the radar illumination direction if the annotation is missing or incomplete. Since the incident angle increases from near-range to far-range, the terrain illumination becomes more oblique. As a result, shadowing becomes more prominent toward the far-range. Information on the scene, such as an object's height, can also be obtained from radar shadows. Shadowing in radar imagery is an important key for terrain relief interpretation.

The last effect is foreshortening; it occurs as long as the slope of the terrain is smaller than the local incidence angle. Foreshortening in a radar image is the appearance of the compression of those features in the scene which are tilted toward the radar. This effect is illustrated in Figure 2.6. Foreshortening leads to the relatively brighter appearance of these slopes and must be accounted for by the interpreter. Foreshortening is at a maximum when a steep slope is orthogonal to the radar beam. In this case, the local incident angle is zero. As a result, the base, slope, and top of a hill are imaged simultaneously. Therefore, they occupy the same position in the image.
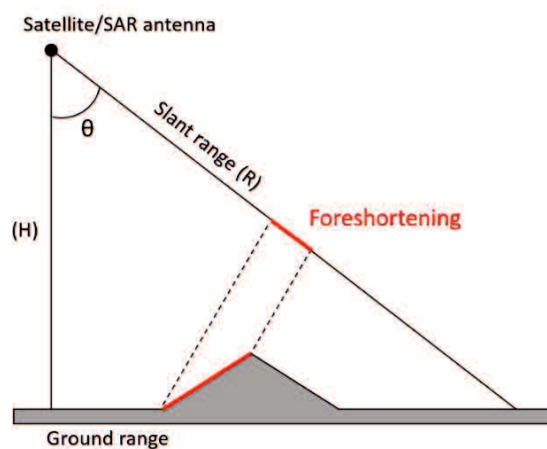
Figure 2.6 Illustration of foreshortening effect on radar imaging system. The foreshortening effect occurs as long as the slope of the terrain is smaller than the local incidence angle (modified from Franceshetti and Lanari, 2000).

For a given slope or hillside, the foreshortening effects are reduced with an increase in the incident angles. At the grazing angle, where the incident angles approach 90°, the foreshortening effects are eliminated, but severe shadowing may occur. In selecting an incident angle, there is always a trade-off between the occurrence of foreshortening and the occurrence of shadowing in the image.

2.2.4 SAR data processing
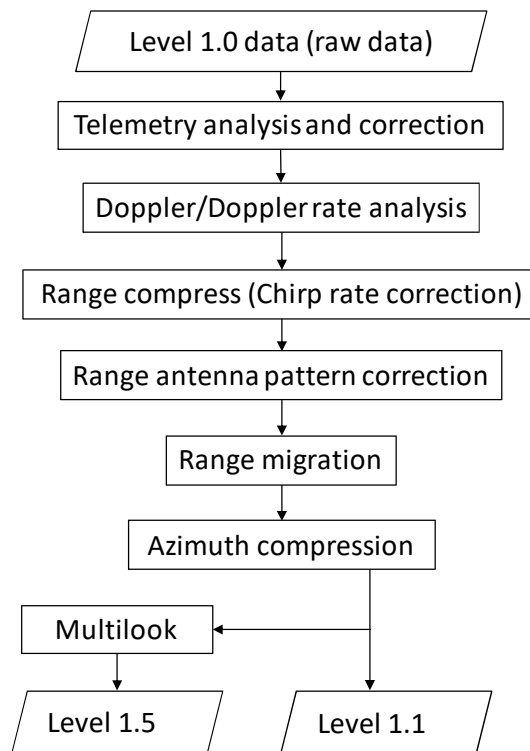
Figure 2.7 Process flow chart of Phased Array type L-band Synthetic Aperture Radar (PALSAR) image generation (modified from Shimada, 2019).

From the signals that are transmitted into SAR images, the data processing should be conducted several times. Based on the processing level, SAR data can generally be classified into three levels. The first is called raw data. Raw data consist of raw signal data before the reconstruction of the SAR images. Raw data are also known as data level 1.0. The second is SLC data, SLC meaning single look complex. These data contain phase and amplitude information in a complex style. SLC data are also known as data level 1.1. The third is image data, also known as data level 1.5, for which each pixel consists of a real value (usually a 2-byte short integer). No phase information is preserved at this level. The processing steps for the SAR (ALOS-PALSAR)

image generation are shown in Figure 2.7. A detailed explanation of SAR data processing can be found in Curlander and McDonough (1991).

2.3 Outline of SAR interferometry

2.3.1 Outline of InSAR and DInSAR

Interferometry SAR (InSAR) is a method for taking the signal phase changes (interference) from two sets of SAR data. A SAR satellite can observe the same area from slightly different look angles. This can be done either simultaneously (with two radar devices mounted on the same platform) or at different times by exploiting repeated orbits of the same satellite. For the InSAR involving the acquisition of two different images, the term "baseline length" is introduced. The baseline length is the distance between the SAR satellite orbits for the first and second observations. The first observation is called "master" and the second is called "slave".

Based on the position of two antennas/sensors among others when taking the data, two kinds of InSAR are introduced, namely, Along Track (AT) InSAR (AT-InSAR) and repeat pass Cross Track (CT) InSAR (CT-InSAR). AT-InSAR consists of placing two (or more) antennas along the body of an aircraft platform and taking data in a single pass. CT-InSAR consists of taking the data from the same area by using a single antenna with two or more passes. In this research, only the repeat pass, CT-InSAR, is used. Its basic concepts are explained in this section.

Interferometric phase φ (the phase difference between master and slave) is composed of two distinctive terms, as expressed by Eq. (2.7) (Pepe and Calo, 2017).

$$\varphi \simeq -\frac{4\pi}{\lambda} B \sin(\theta_0 - \alpha) - \frac{4\pi}{\lambda} \frac{B_\perp}{R \sin\theta} Z \qquad (2.7)$$

where λ is the wavelength of the microwave transmitted from SAR, B is the distance between satellite locations of the first and second visits, $B_\perp$ is the perpendicular baseline, θ is the SAR look angle, α is the angle between the baseline and the horizontal plane, and R is the slant range distance between SAR and the ground surface (see Figure 2.8). The first term on the right-hand side of Eq. (2.7) represents the so-called flat-Earth phase contribution, i.e., the phase that is obtained when the topographic profile is entirely flat ($Z = 0$). The second term relates the interferometric phase to surface height Z.

14
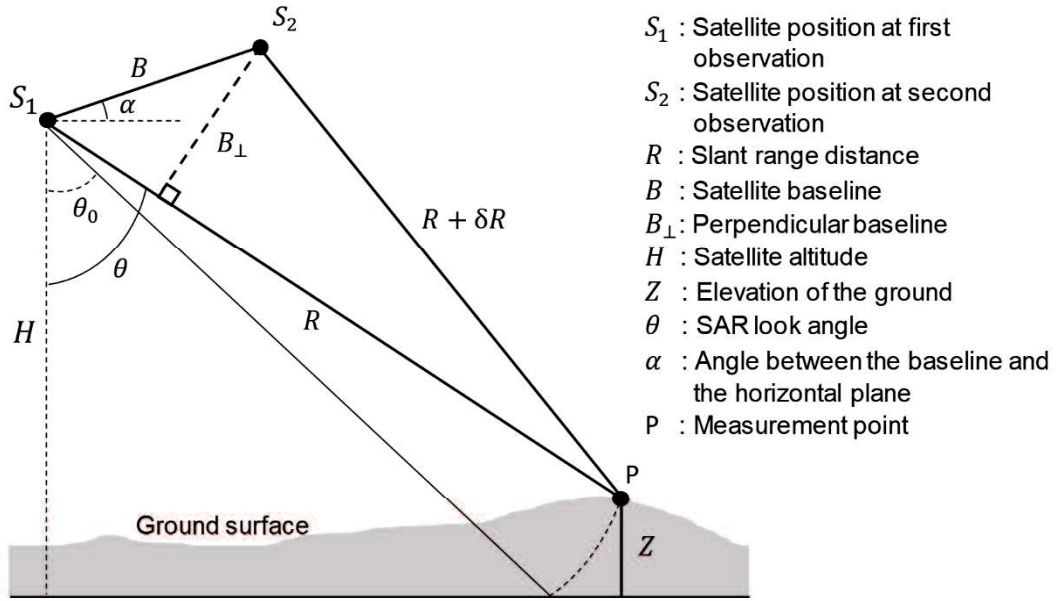
Figure 2.8 Geometrical configuration of InSAR (Pepe and Caló, 2017).

The production of interferograms, from which the topographic contribution has been removed, is called Differential InSAR (DInSAR) (Ferretti et al., 2007). The topographic contribution in Eq. (2.7) can be removed by using the elevation information from other sources, such as the Digital Elevation Model (DEM). Generally, the interferograms computed by the master and slave SAR data contain the ground surface deformation component, $\Delta\varphi_{disp}$, and some phase terms arising from certain inaccuracies of the DEM and the orbital parameters ($\Delta\varphi_{topo}$ and $\Delta\varphi_{orb}$) after removing the above two terms from the right-hand side of Eq. (2.8). The variation in interferometric phase $\Delta\varphi$ can be expressed by Eq. (2.8) (Pepe and Caló, 2017):

$$\Delta\varphi = \Delta\varphi_{disp} + \Delta\varphi_{topo} + \Delta\varphi_{orb} + \Delta\varphi_{atm} + \Delta\varphi_{scatt} + \Delta\varphi_{noise} \tag{2.8}$$

where $\Delta\varphi_{disp} = \frac{4\pi}{\lambda}d$ accounts for the change in distance d between the satellite and the ground surface along the transmitting direction of the pulse wave (namely, LOS: line of sight). Therefore, d is called the LOS displacement, and it is an unknown variable. The phase component induced by the residual topography is represented by $\Delta\varphi_{topo} = -\frac{4\pi}{\lambda}B_\perp \cdot \frac{\Delta Z}{R\sin\theta}$. Residual topography ΔZ occurs due to the non-perfect knowledge of the actual height profile. $\Delta\varphi_{orb}$ accounts for the residual fringes brought about by the use of inaccurate orbital information in the synthesis of the topographic phase. $\Delta\varphi_{atm}$ is the phase contribution due to the variation in the microwave propagation conditions (atmospheric conditions including ionospheric and tropospheric delays)

15

between master and slave acquisitions. $\Delta\varphi_{scatt}$ and $\Delta\varphi_{noise}$ denote the phase components caused by the changes in scattering behavior and in all phase noise contributions, respectively.

DInSAR is the method based on Eq. (2.8). It is employed to compute LOS displacement d from the observed deferential interferometric phase $\Delta\varphi$ by removing the terms from the right-hand side of Eq. (2.8) considering the phase component due to the above residuals, scatters, and noises.

2.3.2 Outline of SBAS

The SAR data are sometimes severely affected by noises. In order to improve the accuracy of the DInSAR results, the SBAS (Small Baseline Subset) method was proposed (Berardino et al., 2002). The key features of the SBAS method are its ability to reduce all of the phase noises and errors from many interferograms and its capacity to isolate only the phases that were contributed by the deformation.

In order to reduce the effect of spatial decorrelation, only the interferograms with small orbital baselines are selected for further time-series analyses. In addition, a procedure is implemented to reduce the decorrelation effect caused by the noises and to prevent their negative impact when computing the LOS displacement. The SBAS method is very robust for providing the results for both large-scale deformation phenomena and more localized displacement effects (Lanari et al., 2007).

The SBAS method is employed in this study (Berardino et al., 2002), and it is outlined below. It is supposed that $N+1$ data of the same SAR are acquired in the same area and that those data are recorded at the ordered times of $t_0, \dots, t_N$. When only the interferograms with small orbital baselines are selected, M differential interferograms can be generated as $\Delta\varphi_1, \dots, \Delta\varphi_M$. The fundamental equation is expressed as follows:

$$\mathbf{B}v = \Delta\varphi \tag{2.9}$$

where $\mathbf{B}$ is an $M \times N$ matrix (M and N are the numbers of involved interferograms and SAR data, respectively, as described above). $\Delta\varphi = \{\Delta\varphi_1, \dots, \Delta\varphi_M\}^T$ is a known vector computed with the SAR data. v is a vector consisting of N unknown phase velocities between adjacent times, as follows:

$$\mathbf{v^T} = \left[v_1 = \frac{\phi_1}{t_1 - t_0}, \dots, v_N = \frac{\phi_N - \phi_{N-1}}{t_N - t_{N-1}} \right] \tag{2.10}$$

16

where $\phi_1, \dots, \phi_N$ are the unknown phases. For the mth interferogram, $\Delta\varphi_m = \phi_j - \phi_k$ (k: master and j: slave), and the element of matrix **B**, namely, b_{mn} (m: rows, n: columns, and $n = 1, 2, \cdots N$), is equal to time interval $t_j - t_k$ ($k + 1 \leq n \leq j$); otherwise ($n \leq k,\ j + 1 \leq n$), it is equal to zero (Berardino et al., 2002). Moreover, any additional time-model information could be encompassed in the fundamental SBAS equation, i.e., Eq. (2.10). For instance, if model parameter vector **p** exhibits a linear relationship with velocity vector $\boldsymbol{v}$, i.e.,

$$\mathbf{v} = \mathbf{Mp} \tag{2.11}$$

where the columns of M describe the vector components of $\boldsymbol{v}$, then Eq. (2.9) can be substituted as follows:

$$\mathbf{BMp} = \Delta\boldsymbol{\varphi} \tag{2.12}$$

The solution to Eq. (2.11) could easily be solved by the left inverse matrix. For example, assuming quadratic behavior for the time variation of the phase signal, for the generic j-component, leads to

$$\phi(t_i) = \bar{v}(t_i - t_0) + \frac{1}{2}\bar{a}(t_i - t_0)^2 \tag{2.13}$$

where $\bar{v}$ and $\bar{a}$ are two unknown parameters accounting for the mean velocity and the mean acceleration, respectively. In this model, the term **p** in Eq. (2.12) is obtained from the following expression:

$$\mathbf{p^T} = [\bar{v}, \bar{a}] \tag{2.14}$$

while **M** is

$$\mathbf{M} = \begin{bmatrix} 1 & \frac{t_1 - t_0}{2} \\ 1 & \frac{t_2 + t_1 + 2t_0}{2} \\ \dots & \dots \\ 1 & \frac{t_N + t_{N-1} + 2t_0}{2} \end{bmatrix} \tag{2.15}$$

2.4 Brief review of SAR interferometry applications for ground deformation monitoring

The first application of SAR interferometry (InSAR) was for topographic mapping (Graham, 1974). Along with its development, InSAR was proposed for use in mapping the ground deformation due to earthquakes (Massonnet and Rabaute, 1993). By this time (the 1990s), it was found that deformation monitoring by InSAR could complement or, in certain cases, replace

ground-based techniques. One of these measurement techniques is known as DInSAR; it enables the continuous analysis of very small ground movements over large areas and has the advantages of high resolution, all-weather adaptability, low cost, and inaccessible area coverage (Wang et al., 2013).

During the last two decades, various types of research on land deformation have been done by many scientists by employing DInSAR techniques. When compared to the results of other methods, like GPS, the DInSAR results show a good agreement. However, improvements to DInSAR are still needed to better its accuracy. For a feasibility analysis, Hanssen (2003) determined two main groups of interferometric parameters, namely, design parameters and environmental parameters. The design parameters include the wavelength, baseline, temporal baseline, number of images, and incidence angle or inclination, while the environmental parameters include atmosphere, surfaces, and deformation. All of the parameters influence the feasibility of deformation monitoring using satellite InSAR.

As with other methods, DInSAR also has limitations in terms of land displacement monitoring. As mentioned by Raucoules et al. (2007), the main limitations in the detection of motion by means of the radar interferometry technique are linked to the loss of coherence with time, the influence of atmospheric artifacts, the presence of uncompensated topography, and instrumental limitations, such as the orbital cycle or the pixel size. Among them, the main limitations are the so-called temporal and geometrical de-correlations as well as the atmospheric artifacts. However, the high precision of the DInSAR results depends not only on the quality of the SAR images, but also on the data processing method used (Chen et al., 2013). The development of the interferometric technique for land displacement monitoring is not yet in the final stages. Improvements to enhance the accuracy of DInSAR are being developed. There are two popular methods for providing more highly accurate results by DInSAR, namely, PSI (Ferretti et al., 2001) and SBAS (Berardino et al., 2002). Both methods exploit a collection of SAR data taken during certain periods. Thus, time-series analyses of the surface displacement can also be conducted. The methods are usually referred to as multi-temporal DInSAR.

The trend of applying DInSAR has been increasing in recent years, especially for long-term subsidence monitoring (Castellazzi et al., 2017; Da Lio et al., 2018; Gao et al., 2016; Hu et al., 2014; Huang et al., 2016; Milillo et al., 2018; Osmanoğlu et al., 2016). Significant improvements in the spatial and temporal resolution of the current SAR satellites drive this enthusiasm. For example, ESA, with their two Sentinel-1 satellites, provides SAR data with a

moderate spatial resolution every 6 days over almost the entire world. Furthermore, the Sentinel-1 SAR data are easy to access through the ESA website and are available at no cost.

The application of multi-temporal DInSAR is also increasing for monitoring landslide areas (Bayer et al., 2017; Colesanti and Wasowski, 2006; Dong et al., 2018; Schlögel et al., 2015; Singhroy et al., 1998; Wang et al., 2013). Its application in landslide areas is challenging due to the geometries and the conditions of the measurement areas. One challenge is the interpretation of the multi-temporal results obtained from slope monitoring. A method has been proposed (Eriksen et al., 2017), but a detailed investigation and records of its application at various sites are still needed.

The application of multi-temporal DInSAR has also been extended to infrastructure monitoring, such as dams, railways, and bridges (Huang et al., 2017; Milillo et al., 2018; Selvakumaran et al., 2018; Sousa et al., 2014; Wang et al., 2018). Although some issues remain to be solved, they will be addressed in studies on future applications of multi-temporal DInSAR.

References

Apel, J.. R., Jackson, C.. R., 2004. Principles of synthetic aperture radar. Synth. aperture radar Mar. user's Man. 20–32.

Bayer, B., Simoni, A., Schmidt, D., Bertello, L., 2017. Using advanced InSAR techniques to monitor landslide deformations induced by tunneling in the Northern Apennines, Italy. Eng. Geol. 226, 20–32. https://doi.org/10.1016/j.enggeo.2017.03.026

Berardino, P., Fornaro, G., Lanari, R., Sansosti, E., 2002. A new algorithm for surface deformation monitoring based on small baseline differential SAR interferograms. IEEE Trans. Geosci. Remote Sens. 40, 2375–2383. https://doi.org/10.1109/TGRS.2002.803792

Castellazzi, P., Garfias, J., Martel, R., Brouard, C., Rivera, A., 2017. InSAR to support sustainable urbanization over compacting aquifers: The case of Toluca Valley, Mexico. Int. J. Appl. Earth Obs. Geoinf. 63, 33–44. https://doi.org/10.1016/j.jag.2017.06.011

Chen, J., Wu, J., Zhang, L., Zou, J., Liu, G., Zhang, R., Yu, B., 2013. Deformation trend extraction based on multi-temporal insar in shanghai. Remote Sens. 5, 1774–1786. https://doi.org/10.3390/rs5041774

Colesanti, C., Wasowski, J., 2006. Investigating landslides with space-borne Synthetic Aperture Radar (SAR) interferometry. Eng. Geol. 88, 173–199. https://doi.org/10.1016/j.enggeo.2006.09.013

Curlander, J.C., McDonough, R.N., 1991. Synthetic aperture radar- Systems and signal processing. John Wiley & Sons, Inc, New York.

Da Lio, C., Teatini, P., Strozzi, T., Tosi, L., 2018. Understanding land subsidence in salt marshes of the Venice Lagoon from SAR Interferometry and ground-based investigations. Remote Sens. Environ. 205, 56–70. https://doi.org/10.1016/j.rse.2017.11.016

Da Lio, C., Tosi, L., 2018. Land subsidence in the Friuli Venezia Giulia coastal plain, Italy: 1992–2010 results from SAR-based interferometry. Sci. Total Environ. 633, 752–764. https://doi.org/10.1016/j.scitotenv.2018.03.244

Dong, J., Zhang, L., Tang, M., Liao, M., Xu, Q., Gong, J., Ao, M., 2018. Mapping landslide surface displacements with time series SAR interferometry by combining persistent and distributed scatterers: A case study of Jiaju landslide in Danba, China. Remote Sens. Environ. 205, 180–198. https://doi.org/10.1016/j.rse.2017.11.022

Eriksen, H.Ø., Lauknes, T.R., Larsen, Y., Corner, G.D., Bergh, S.G., Dehls, J., Kierulf, H.P., 2017. Visualizing and interpreting surface displacement patterns on unstable slopes using multi-geometry satellite SAR interferometry (2D InSAR). Remote Sens. Environ. 191, 297–312. https://doi.org/10.1016/j.rse.2016.12.024

Ferretti, A., Prati, C., Rocca, F., 2001. Permanent scatterers in SAR interferometry. IEEE Trans. Geosci. Remote Sens. 39, 8–20. https://doi.org/10.1109/36.898661

Ferretti, A., Monti-guarnieri, A., Prati, C., Rocca, F., 2007. InSAR Principles: Guidelines for SAR Interferometry Processing and Interpretation (TM-19, February 2007), Esa. https://doi.org/10.1787/9789264101630-5-en

Franceschetti, G., Lanari, R. 2000. Synthetic Aperture Radar Processing. CRC Press LLC, Florida.

Gao, M., Gong, H., Chen, B., Zhou, C., Chen, W., Liang, Y., Shi, M., Si, Y., 2016. InSAR time-series investigation of long-term ground displacement at Beijing Capital International Airport, China. Tectonophysics 691, 271–281. https://doi.org/10.1016/j.tecto.2016.10.016

Graham, L.C., 1974. Synthetic Interferometer Radar For Topographic Mapping. Proc. IEEE 62, 763–768. https://doi.org/10.1109/PROC.1974.9516

Hanssen, R.F., 2001. Radar Interferometry: Data Interpretation and Error Analysis. Kluwer Academic Publishers, Dordrecht

Hanssen R.F. 2003. Subsidence Monitoring Using Contiguous and PS-InSAR: Quality Assessment Based on Precision and Reliability. Proceedings, 11th FIG Symposium on Deformation Measurements. Santorini, Grace

Henri, M. 2008. Processing of Synthetic Aperture Radar Images. John Wiley & Sons, Inc, Hoboken.

Hu, B., Wang, H.S., Sun, Y.L., Hou, J.G., Liang, J., 2014. Long-term land subsidence monitoring of Beijing (China) using the small baseline subset (SBAS) technique. Remote Sens. 6, 3648–3661. https://doi.org/10.3390/rs6053648

Huang, M.H., Bürgmann, R., Hu, J.C., 2016. Fifteen years of surface deformation in Western Taiwan: Insight from SAR interferometry. Tectonophysics 692, 252–264. https://doi.org/10.1016/j.tecto.2016.02.021

Huang, Q., Crosetto, M., Monserrat, O., Crippa, B., 2017. Displacement monitoring and modelling of a high-speed railway bridge using C-band Sentinel-1 data. ISPRS J. Photogramm. Remote Sens. 128, 204–211. https://doi.org/10.1016/j.isprsjprs.2017.03.016

Lanari, R., Casu, F., Manzo, M., Zeni, G., Berardino, P., Manunta, M., Pepe, A., 2007. An overview of the Small BAseline Subset algorithm: A DInSAR technique for surface deformation analysis. Pure Appl. Geophys. https://doi.org/10.1007/s00024-007-0192-9

Lusch, P.D. 1999. Introduction to Microwave Remote Sensing. Michigan University, Michigan.

Massonnet, D., Rabaute, T., 1993. Radar Interferometry: Limits and Potential. IEEE Trans. Geosci. Remote Sens. 31, 455–464. https://doi.org/10.1109/36.214922

Milillo, P., Giardina, G., DeJong, M.J., Perissin, D., Milillo, G., 2018. Multi-temporal InSAR structural damage assessment: The London crossrail case study. Remote Sens. 10, 20–22. https://doi.org/10.3390/rs10020287

Osmanoğlu, B., Sunar, F., Wdowinski, S., Cabral-Cano, E., 2016. Time series analysis of InSAR data: Methods and trends. ISPRS J. Photogramm. Remote Sens. 115, 90–102. https://doi.org/10.1016/j.isprsjprs.2015.10.003

Restec, 2014. Principle of Synthetic Aperture Radar, Japan.

Raucoules, D., Colesanti, C., Carnec, C., 2007. Use of SAR interferometry for detecting and assessing ground subsidence. Comptes Rendus - Geosci. 339, 289–302. https://doi.org/10.1016/j.crte.2007.02.002

Sandwell, T.D., Mellors, R., Tong, X., Wei, M., Wessel, P. 2011. GMTSAR: An InSAR Processing System Based on Generic Mapping Tools. Topex [online]. Available at: http://topex.ucsd.edu/gmtsar/tar/GMTSAR.pdf (Accessed: 30 October 2014).

Schlögel, R., Doubre, C., Malet, J.P., Masson, F., 2015. Landslide deformation monitoring with ALOS/PALSAR imagery: A D-InSAR geomorphological interpretation method. Geomorphology 231, 314–330. https://doi.org/10.1016/j.geomorph.2014.11.031

Selvakumaran, S., Plank, S., Geiß, C., Rossi, C., Middleton, C., 2018. Remote monitoring to predict bridge scour failure using Interferometric Synthetic Aperture Radar (InSAR) stacking techniques. Int. J. Appl. Earth Obs. Geoinf. 73, 463–470. https://doi.org/10.1016/j.jag.2018.07.004

Shimada, M., 2019. Imaging from spaceborne and airborne SARs, calibration, and applications. CRC Press, Florida.

Singhroy, V., Mattar, K.., Gray, a. ., 1998. Landslide characterisation in Canada using interferometric SAR and combined SAR and TM images. Adv. Sp. Res. 21, 465–476. https://doi.org/10.1016/S0273-1177(97)00882-X

Sousa, J.J., Hlaváčová, I., Bakoň, M., Lazecký, M., Patrício, G., Guimarães, P., Ruiz, A.M., Bastos, L., Sousa, A., Bento, R., 2014. Potential of Multi-temporal InSAR Techniques for Bridges and Dams Monitoring. Procedia Technol. 16, 834–841. https://doi.org/10.1016/j.protcy.2014.10.033

Pepe, A., Caló, F., 2017. A Review of Interferometric Synthetic Aperture RADAR (InSAR) Multi-Track Approaches for the Retrieval of Earth's Surface Displacements. Appl. Sci. 7, 1264. https://doi.org/10.3390/app7121264

Wang, G., Xie, M., Chai, X., Wang, L., Dong, C., 2013. D-InSAR-based landslide location and monitoring at Wudongde Hydropower Reservoir in China. Environ. Earth Sci. 69, 2763–2777. https://doi.org/10.1007/s12665-012-2097-x

Wang, H., Chang, L., Markine, V., 2018. Structural Health Monitoring of Railway Transition Zones Using Satellite Radar Data. Sensors 18, 413. https://doi.org/10.3390/s18020413

Chapter 3

Monitoring of long-term land subsidence in coastal area by multi-temporal DInSAR analyses

3.1 Introduction

The land subsidence phenomenon is a crucial issue that the Indonesian government must address. Several cities have reported being impacted by this phenomenon (Chaussard et al., 2013). Semarang is one of those cities. The subsidence in Semarang has led to serious and costly damage to urban infrastructures, such as buildings, roads, and railway tracks. Moreover, the city has frequently been hit by floods which have severely affected the living conditions of the urban population there (Abidin et al., 2013; Andreas et al., 2017; Gumilar et al., 2013; Marfai et al., 2008).

Monitoring subsidence is a vital task related to predicting and mitigating the disasters that subsidence may cause. The subsidence in Semarang has been monitored by terrestrial methods, such as leveling, and by GPS surveys at several measurement points (Abidin et al., 2013; Gumilar et al., 2013; Marfai and King, 2007). Although these methods are useful and can provide precise measurement results, they require the installation of devices as well as personnel on the ground. Therefore, displacement monitoring can be costly especially when conducted over a vast area. Moreover, these methods provide data limited to the measurement points where the leveling marks and the GPS receivers are installed.

DInSAR, on the other hand, has the potential to be an effective tool for measuring land surface deformation over vast areas with centimeter-order accuracy and high spatial resolution after spatial averaging and geocoding (Massonnet and Feigl, 1998). Moreover, the accuracy of DInSAR has been improved by the development of advanced processing algorithms and methods. One of those methods is Permanent Scatterer Interferometry (PSI) (Ferretti et al., 2001) and another is the Small Baseline Subset (SBAS) method (Berardino et al., 2002). Furthermore, DInSAR does not require the installation of any devices on the ground. Recently, DInSAR has been widely used for measuring the displacements of the land surface (Jo et al., 2017; Liu et al., 2016; Moghaddam et al., 2013; Morishita et al., 2016; Raucoules et al., 2007; Singhroy and Molch, 2004).

Research on the land subsidence in Semarang, based on DInSAR, has been conducted by several researchers (Arimoto et al., 2013; Chaussard et al., 2013; Kuehn et al., 2010; Lubis et al., 2011). Kuehn et al. (2009) monitored the subsidence from 2002 to 2006 using Envisat-ASAR data. Lubis et al. (2010) monitored the subsidence from 2007 to 2009 using ALOS-PALSAR data. Both sets of results show that the subsidence rates vary from fractions of 1 mm/year to 10 cm/year and even beyond. However, their results have not been validated against other results using different methods, such as leveling or GPS. On the other hand, a time-series analysis using ALOS-PALSAR data was carried out by Arimoto et al. (2013) and Chaussard et al. (2013), and their results were roughly compared with GPS campaign results only for a 1-year period (2008-2009). A good correlation was shown, but a comparison should be conducted with longer GPS campaign results. In addition, the subsidence map for Semarang needs to be updated.

In this study, the long-term subsidence in Semarang, for up to 14 years, is obtained by using SBAS DInSAR with different SAR data sets, i.e., Envisat-ASAR, ALOS-PALSAR, and Sentinel-1A. A set of data observed by each SAR is independently analyzed and the results are placed in chronological order. Time-series subsidence maps, showing the evolution of spatiotemporal subsidence, are generated. The SBAS DInSAR results are validated by a comparison with the GPS results for dozens of observation points (Abidin et al., 2013). In order to discuss the time transition of the subsidence from 2003 to 2017, the hyperbolic method (Tan et al., 1991) is applied to connect the unlinked SBAS results. Finally, the discussion is extended to the subsidence phenomenon in Semarang by considering the geological conditions and the groundwater extraction activities.

3.2 Outline of Semarang

The study area is city of Semarang; it is located in the north of Java Island, Indonesia. Geographically, Semarang lies at 6°58′S 110°25′E. It is the capital and largest city of the Central Java Province. Semarang has an area of about 373.70 square kilometers (144.29 sq mi) and a population of about 1.5 million (BPS, 2016). Semarang is an industrial city, and most of its commercial and industrial areas are built on a flat coastal plain with elevations ranging from 0 to 10 m (Marfai and King, 2007).

Figure 3.1 shows the location and geological conditions of Semarang. Geologically, Semarang has three main lithologies, namely, the Kaligetas Formation (sedimentary and partially volcanic rock) in the south, the Damar Formation (sedimentary rock) in the middle, and Alluvium

in the north (Thaden et al., 1975). The Kaligetas Formation consists of volcanic breccias, basaltic lava, tuff, sandstone, and claystone. The Damar Formation is composed of tuffaceous claystone, volcanic breccias, sandstone, tuff, and conglomerates. The Alluvium consists of pebbles, sand, silt, and clay as river and swamp deposits, and it covers the surface with a thickness of up to 150 m.
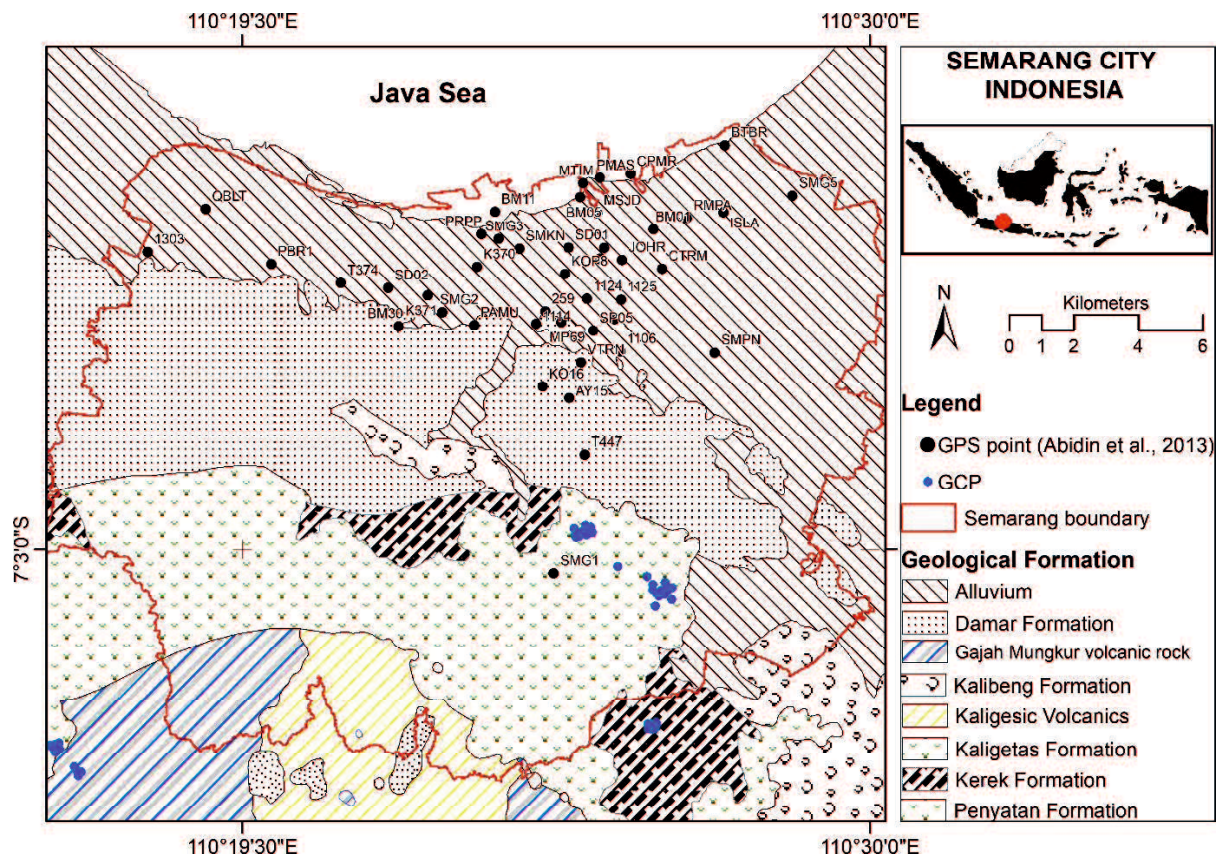
Figure 3.1 Geological conditions of Semarang and surrounding area (modified from geologic map published by Geological Survey of Indonesia) (Thaden et al., 1975).

The subsidence in Semarang occurs in areas of marine and alluvium sediments. It has been measured in several places since the 1980s using various measurement techniques, e.g., benchmark and field surveys, Dutch cone sounding, consolidation tests, standard penetration tests, and groundwater level studies (Marfai and King, 2007). Moreover, since 1983, government agencies have been monitoring the subsidence and have implemented several measures to mitigate the problem. However, continuous subsidence monitoring results have not been published recently.

3.3 Procedure of multi-temporal DInSAR

3.3.1 Data collection

Table 3.1 List of SAR data: Envisat-ASAR (path number 318), ALOS-PALSAR (path number 431), and Sentinel-1A (path number 76).

No.	ENVISAT-ASAR Date	ALOS-PALSAR Date	Sentinel-1A Date
0	2003-03-12	2007-01-21	2015-01-26
1	2003-04-16	2007-06-08	2015-03-27
2	2003-06-25	2007-09-08	2015-05-14
3	2003-07-30	2007-10-24	2015-06-07
4	2003-10-08	2007-12-09	2015-07-01
5	2004-05-05	2008-01-24	2015-07-25
6	2004-08-18	2008-03-10	2015-08-18
7	2004-09-22	2008-04-25	2015-09-11
8	2005-01-05	2008-06-10	2015-10-29
9	2005-06-29	2008-07-26	2015-11-22
10	2005-08-03	2008-09-10	2015-12-16
11	2005-09-07	2008-10-26	2016-01-09
12	2006-01-25	2008-12-11	2016-02-02
13	2006-04-05	2009-01-26	2016-02-26
14	2006-05-10	2009-06-13	2016-03-21
15	2006-06-14	2009-10-29	2016-04-14
16	2006-07-19	2009-12-14	2016-05-08
17	2006-08-23	2010-01-29	2016-06-01
18	2006-11-01	2010-03-16	2016-07-19
19	2007-01-10	2010-06-16	2016-08-12
20	2007-08-08	2010-09-16	2016-09-05
21	2007-10-17	2010-11-01	2016-09-29
22		2010-12-17	2016-10-23
23		2011-02-01	2016-11-16
24			2016-12-10
25			2017-01-03
26			2017-01-27
27			2017-02-08
28			2017-02-20
29			2017-03-04

Seventy-six sets of SAR data are used to conduct the time-series analysis of the subsidence. The data are classified into three groups since they were acquired by three different satellites carrying SAR sensors, namely, Envisat-ASAR, ALOS-PALSAR, and Sentinel-1A. The Envisat-ASAR and Sentinel-1A data were provided by the European Space Agency (ESA), and the ALOS-

PALSAR data were provided by the Japan Exploration Agency (JAXA). Envisat and Sentinel-1A are European satellites which carry a SAR sensor and operate in the C-band channel. ALOS is a Japanese satellite which carries a PALSAR sensor and operates in the L-band channel.

The Envisat-ASAR and Sentinel-1A data were acquired during the descending passage and in a right-looking observation direction. The ALOS-PALSAR data were acquired during the ascending passage and in a right-looking observation direction. As shown in Table 3.1, the first data gathered by Envisat-ASAR were available starting in March 2003, while the last were available starting in October 2007. On the other hand, the first data gathered by ALOS-PALSAR were available starting in January 2007 and the last were available starting in February 2011. Several months overlap between the Envisat-ASAR and the ALOS-PALSAR data. The Sentinel-1A data were available from the beginning of 2015; this means that no SAR data were available for almost four years from 2011 to 2015.

3.3.2 SBAS processing

The SBAS method is employed in this study along with the quadratic model (Berardino et al., 2002), which is implemented using the software ENVI SARscape 5.3 (Sarmap, 2013). Since every SAR sensor (i.e., Envisat-ASAR, ALOS PALSAR, and Sentinel-1) has unique characteristics, in terms of its electromagnetic properties, it is not able to make an interferogram using the data from a different sensor. Therefore, the SBAS method was applied separately to all the data sets for each SAR satellite. In addition, only co-polarization images were used, namely, VV polarization for Envisat-ASAR and Sentinel-1A and HH polarization for ALOS-PALSAR. The Digital Elevation Model (DEM) data, produced by Shuttle Radar Topography Mission3 (SRTM3), were used to remove the phase component of the topography from the interferogram.

Firstly, the criteria for the perpendicular and temporal baseline thresholds for the SBAS processing were determined based on the study area conditions and the SAR data. Perpendicular baselines that are a few tens to a few hundreds of meters are usually used (Liu and Mason, 2016). For the ALOS-PALSAR data, longer perpendicular baselines (up to 1 km) can be used since longer wavelengths are less sensitive to geometrical distortions (Sandwell et al., 2008). However, there is no definite value for the temporal baseline threshold. The setting of this parameter depends on the conditions of the research area. If the study area is an urban area, the temporal baseline can be set for a longer period of time, since many stable points can maintain their coherence for a long time. An interferogram can still be generated over an urban area even if the temporal baseline is

up to 4 years (Lanari et al., 2007). Based on these considerations, a baseline table and its connection graph can be produced for each group.

The connection graph for each set of data is presented in Figures 3.2 (a) –(c). The yellow and green dots in these figures represent the super master and the slave of the SAR data, respectively. The black lines represent the interferograms that pass the SBAS minimal requirements, and the red dot means the discarded SAR image which is not suitable for generating an interferogram. The maximum allowable perpendicular and temporal baselines of the interferogram for the SBAS processing of the Envisat-ASAR data are 475 m and 350 days, respectively. Thirty-seven pairs of interferograms passed the criteria, and their connection graph is shown in Figure 3.2 (a), where the mean absolute perpendicular baseline is 258 m and the mean temporal baseline is 190 days. The connection graph for the ALOS-PALSAR data is presented in Figure 3.2 (b). For the ALOS-PALSAR data, the perpendicular and temporal baseline criteria were set at 1300 m and 420 days, respectively, and 97 interferograms were suitable. The mean absolute perpendicular baseline and the mean absolute temporal baseline are 652 m and 220 days, respectively. The connection graph for the Sentinel-1A data is shown in Figure 3.2 (c). The maximum perpendicular and temporal baselines for the Sentinel-1A data were set at 160 meters and 180 days, respectively. Accordingly, 170 interferograms for Sentinel-1A were employed in the analysis for which the mean absolute perpendicular baseline and the mean absolute temporal baseline are 46 m and 93 days, respectively.

Interferogram processing is affected by the noises in the low-coherence area (Raucoules et al., 2007). In order to reduce the noises, the interferogram multi-looks operation is conducted. The number of looks for Envisat-ASAR, ALOS-PALSAR, and Sentinel data were set at 1x5, 3x8, and 5x1, respectively, in range and azimuth directions. Interferogram multi-looking is effective for reducing noises with the tradeoff of the spatial resolution (Hanssen, 2001). In addition, to improve the quality of the interferograms, the Goldstein filter (Goldstein and Werner, 1998) was applied. This process is important for making the unwrapping process easier. The unwrapping process was then conducted for each interferogram to reveal its absolute phase. The robust minimum cost flow (MCF) algorithm (Costantini, 1998) was utilized to accomplish this step. In the unwrapping step, the coherence threshold is set at 0.2, which means the pixels with coherence of less than 0.2 are not involved in the calculation and are removed.

Some of the interferograms experienced interference by orbital error fringes. These orbital error fringes were refined by applying a 2nd order polynomial estimation in the azimuth and range

directions (Hanssen, 2001). Some ground control points (GCPs) were used for the calibration; their locations are shown in Figure 3.1. The unwrapping process was then repeated for the refined interferograms. The dominant source of errors for InSAR is an atmospheric phase screen (APS) (Tang et al., 2016). To reduce the errors induced by the APS, spatio-temporal filtering was carried out. Finally, geocoding process image resampling was conducted. In this step, the coherence threshold was set at 0.4. As the final results, time-series LOS-displacement maps, obtained by each data set with a spatial resolution of about 25 m by 25 m, were generated.
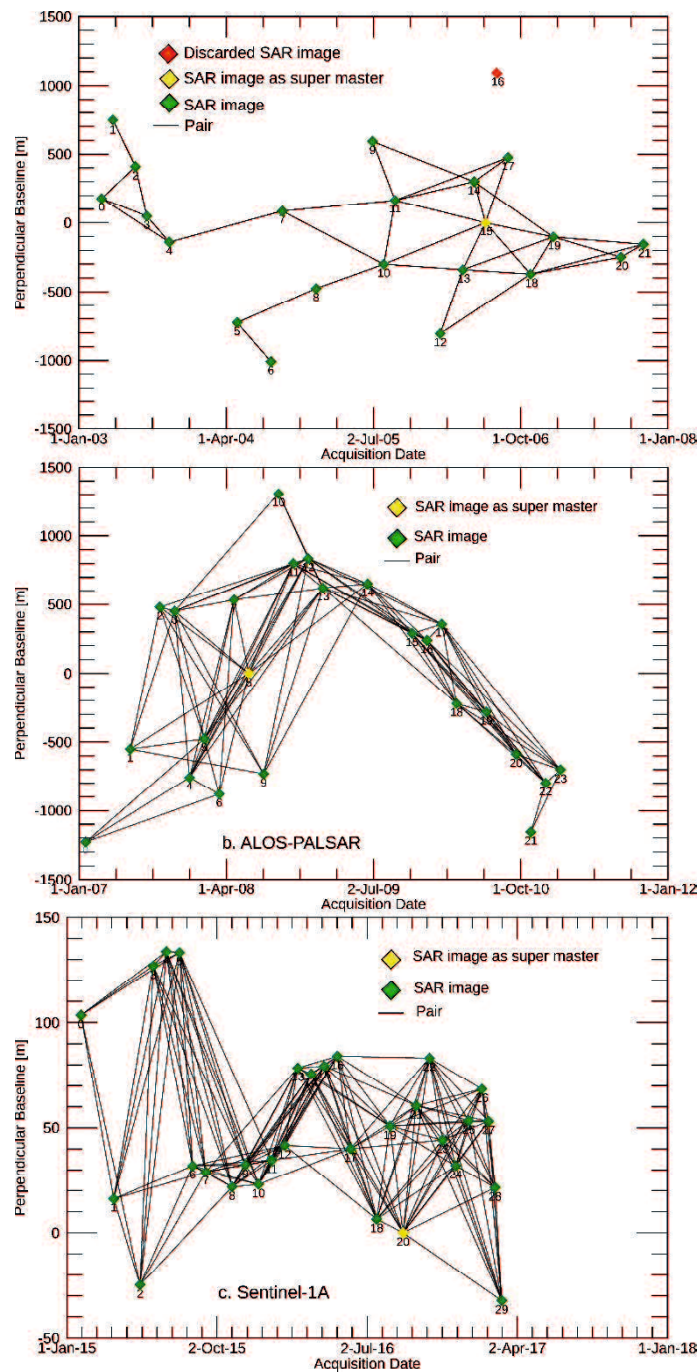
Figure 3.2 Baseline table sets of data: (a) Envisat-ASAR, (b) ALOS-PALSAR, and (c) Sentinel-1A.

3.3.3 Derivation of land subsidence from LOS displacement

The displacement observed by DInSAR is one dimensional along the line of sight (LOS). An additional operation is required to convert the LOS displacement to the subsidence. This operation assumes that the displacement is mainly caused by the subsidence (vertical displacement) and that the horizontal displacement is very small compared to the subsidence; and thus, it can be ignored. The relationship between the LOS displacement and the subsidence is shown in Figure 3.3. In this figure, θ_i and R are the incidence angle and the slant range, respectively. H is the altitude of the satellite. Following the above assumption, the vertical displacement or subsidence can then be calculated from Eq. (3.1). Subsidence S is assigned a negative sign.

$$S = -\frac{d}{\cos\theta_i} \tag{3.1}$$

where d is the LOS displacement (where the extension of LOS is given a positive sign).
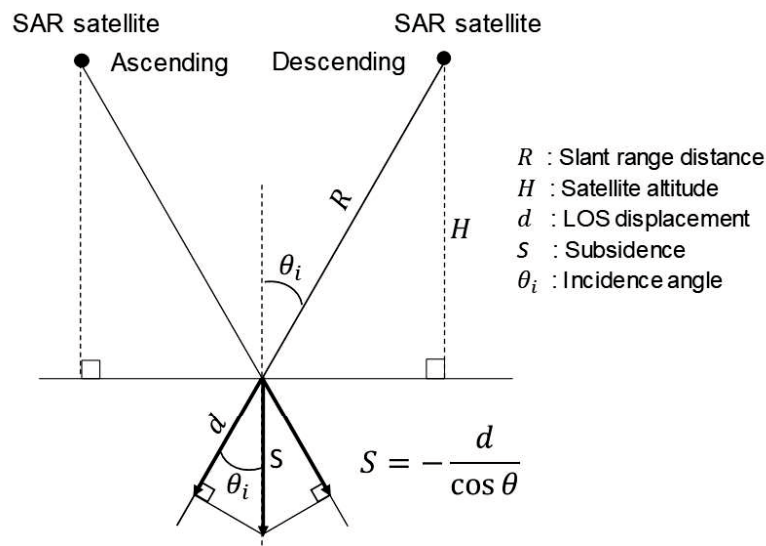
Figure 3.3 Illustration of relationship between LOS displacement and subsidence under assumption of no horizontal displacement.

3.4 Spatial distribution of subsidence

3.4.1 Time-series subsidence map

The spatial distribution of the subsidence over a period of 14 years is presented. It seems to be the longest period of subsidence analysis ever conducted for Semarang. Using the SBAS method, a subsidence map was generated for each data acquisition date. Time-series subsidence maps are presented in Figures. 3.4, 3.5, and 3.6 to show the clear evolution of subsidence over time. It should be noted that since each data set was analyzed independently, the color legend for

each time-series map is reset to have a value of zero on the date of the first data for each SAR data set.
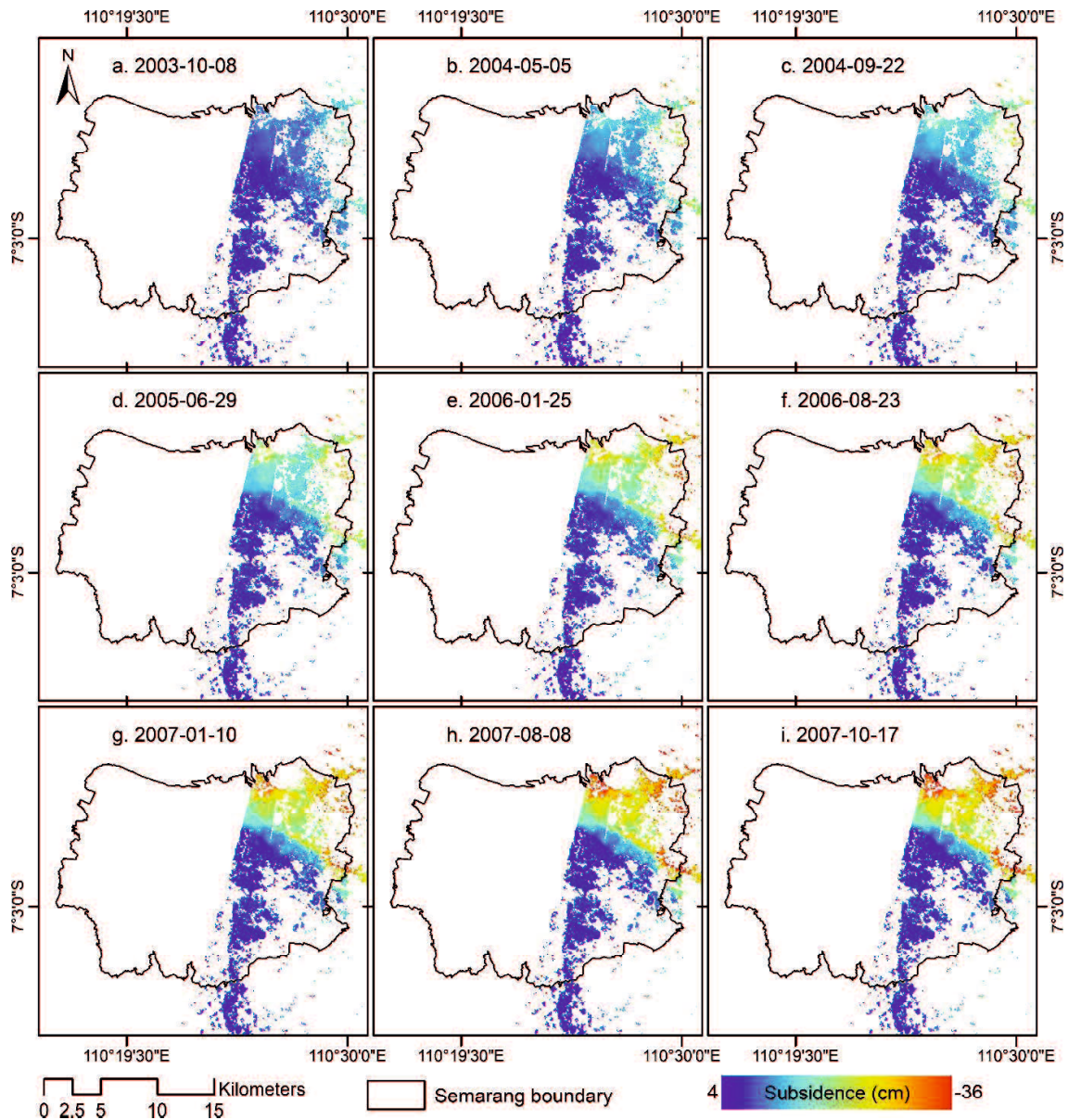
Figure 3.4 Subsidence distribution maps of Semarang: evolution of subsidence from 2003-03-12 until 2007-10-17 using Envisat-ASAR data.

Figure 3.4 shows the evolution of subsidence from 2003-2007 using the Envisat-ASAR data set. Unfortunately, the images do not cover the entire Semarang area; they only cover the eastern half of the area. The subsidence is presented by the range in colors from blue to red for small to large displacements. The area without any color in the eastern half means that no results were obtained for the subsidence due to the low coherence of the interferogram. Low-coherence areas in InSAR can usually be found in heavily vegetated areas, on the water, or on flat surfaces

(Hanssen, 2001). Figure 3.4 shows that the northeast part of the coastal area experienced the highest subsidence rate compared to the other areas in the south. The subsidence in that area rose to 36 cm in four years. These results correspond to the prior results by Kuehn et al. (2010) for which the subsidence was derived in the same periods with a method based on the Stable Point Network (SPN) technique.
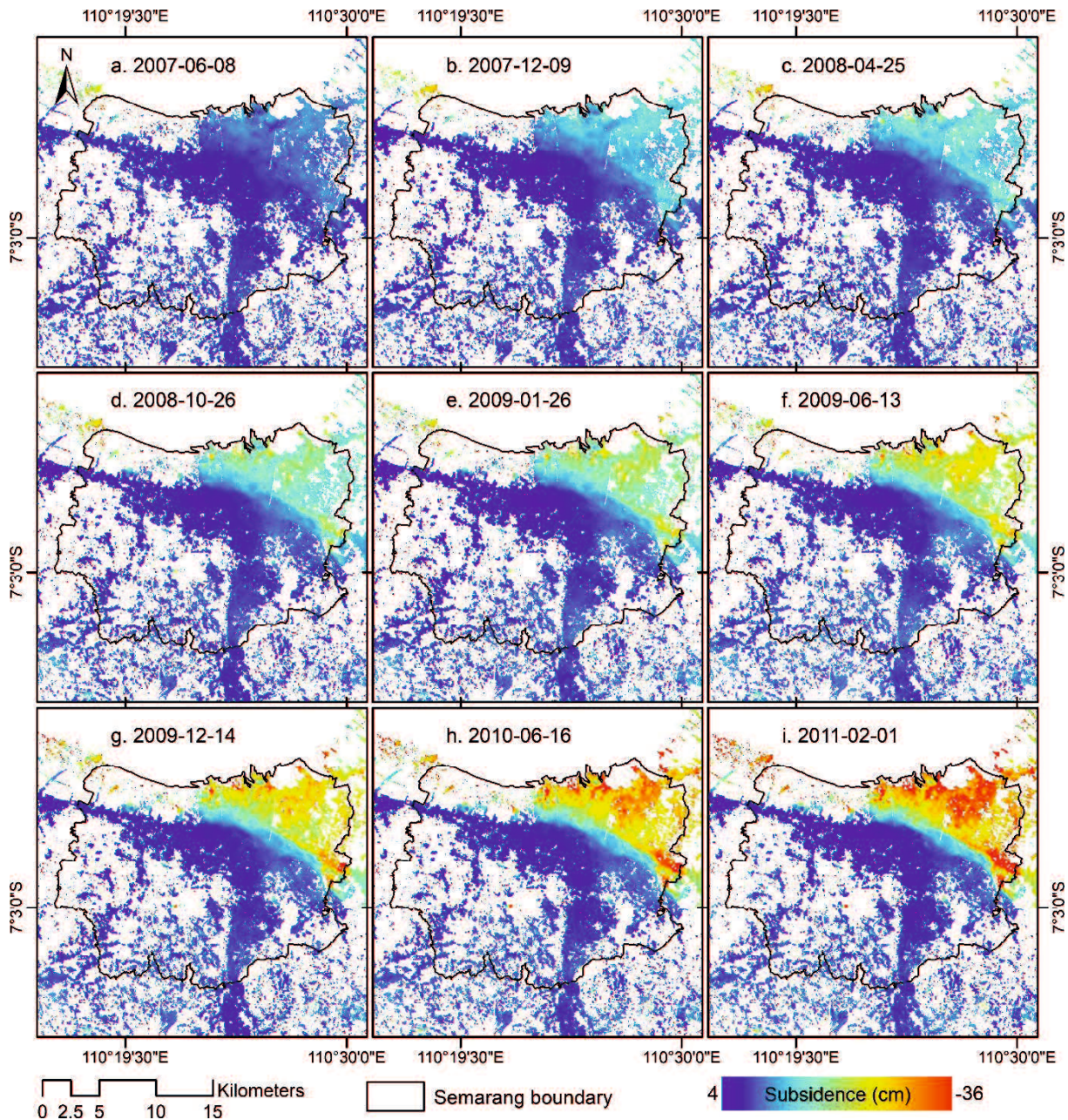
Figure 3.5 Subsidence distribution maps of Semarang: evolution of subsidence from 2007-01-21 to 2011-02-01 using ALOS-PALSAR data.

Figure 3.5 shows the evolution of subsidence from 2007-2011 using the ALOS-PALSAR data set. The spatial distribution of the subsidence does not show as many changes as the previous

results by Envisat-ASAR. The largest subsidence occurred in the northeast part of the Semarang coastal area. Since the ALOS-PALSAR data cover the whole city, it is found that the northwest part of the coastal area also experienced large subsidence.

Figure 3.6 shows the subsidence maps that were derived by Sentinel-1A. These maps show the subsidence from 2015-2017. The spatial distribution pattern of subsidence is similar to the previous observation results by ALOS-PALSAR shown in Figure 3.6. A large area of subsidence is still concentrated in the northeast part.
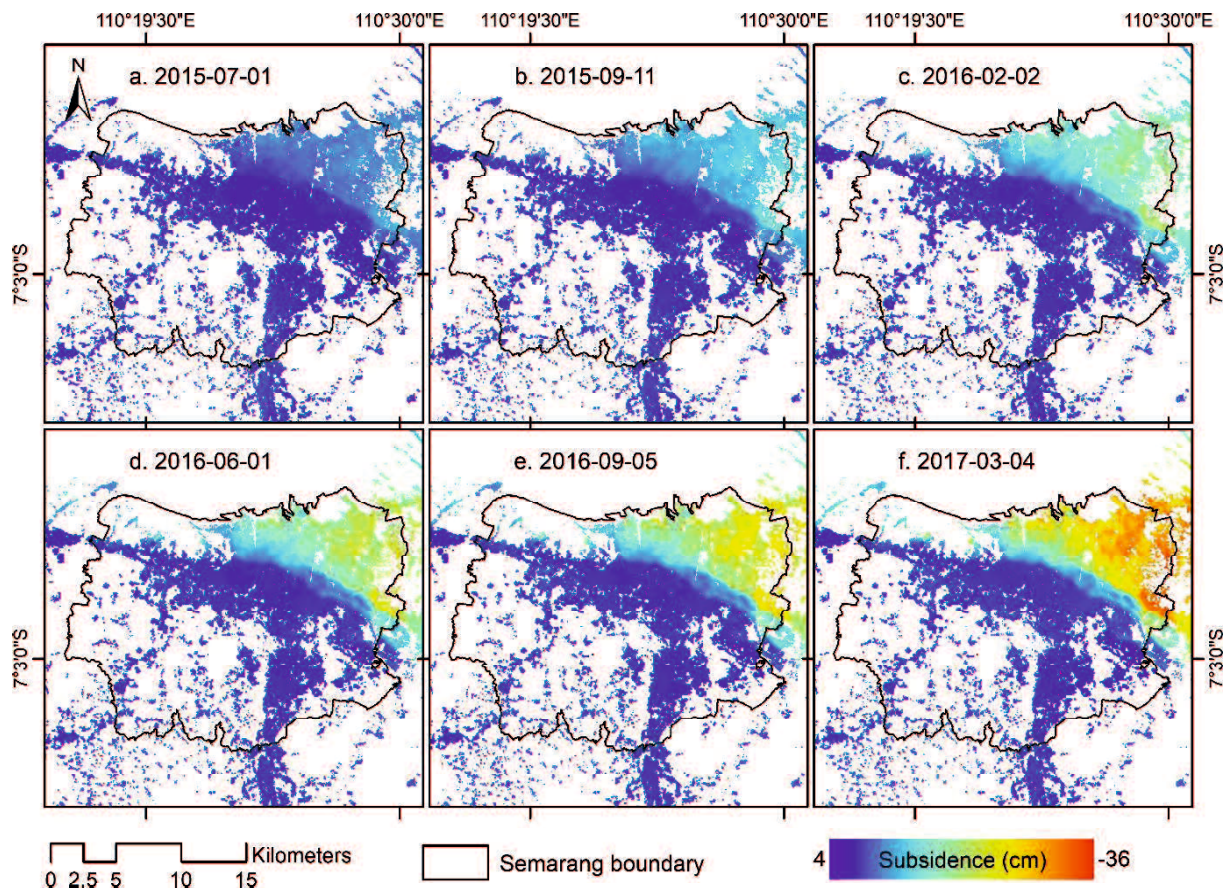
Figure 3.6 Subsidence distribution maps of Semarang: evolution of subsidence from 2015-01-07 to 2017-03-04 using Sentinel-1A data.

3.4.2 Subsidence related to geological conditions

Figure 3.7 presents a geological map and total subsidence maps generated by each satellite that were superimposed onto the geological map. Generally, the spatial distribution pattern of the subsidence in Semarang does not change much. These maps reveal that large subsidence has occurred in the Alluvium area. The area where the subsidence transits from large to small clearly matches the boundary between the Damar Formation (sedimentary rock) and the Alluvium. The Alluvium has the potential to subside due to consolidation. On the other hand, the Damar

Formation is firm. This means that the geological conditions influence the different effects on the subsidence process in Semarang.
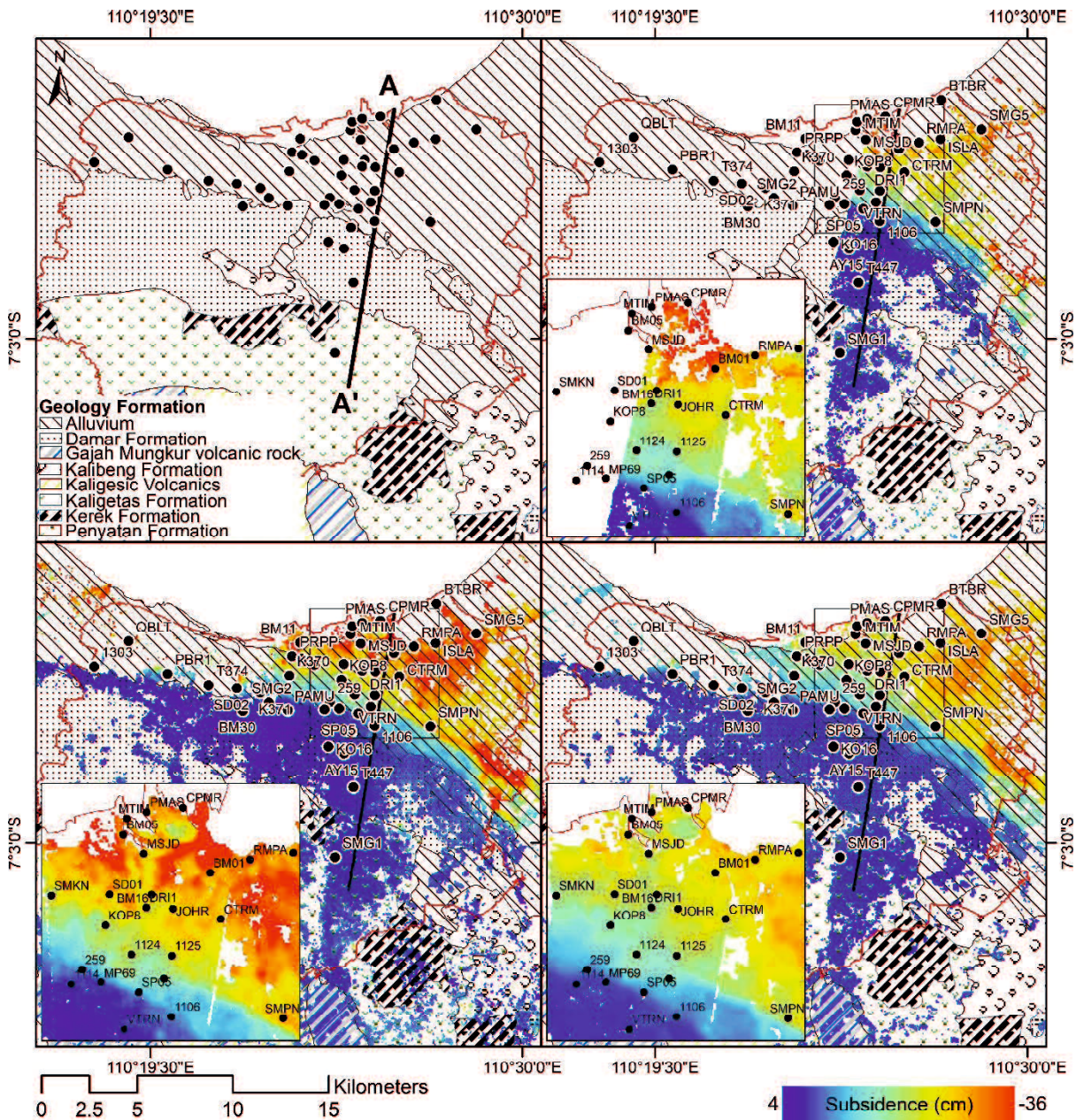
Figure 3.7 Subsidence distribution maps superimposed on map of geological conditions: (a) geological conditions of Semarang, (b) subsidence map by Envisat-ASAR (2003-2007), (c) subsidence map by ALOS-PALSAR (2007-2011), and (d) subsidence map by Sentinel-1A (2015-2017).

The subsidence distribution along cross-section line A-A' in Figure 3.7 is shown in Figure 3.8 for the three periods. The elevation of the ground surface is also illustrated. Its relationship is shown in Figure 3.8. The area in the north, composed of the Alluvium, exhibits large subsidence. The subsidence around the boundary between the Alluvium and the Damar Formation becomes

smaller than the subsidence in the north area. Almost no subsidence is seen in the area of the Damar and Kaligetas Formations. The subsidence in the area of Alluvium becomes larger year by year.
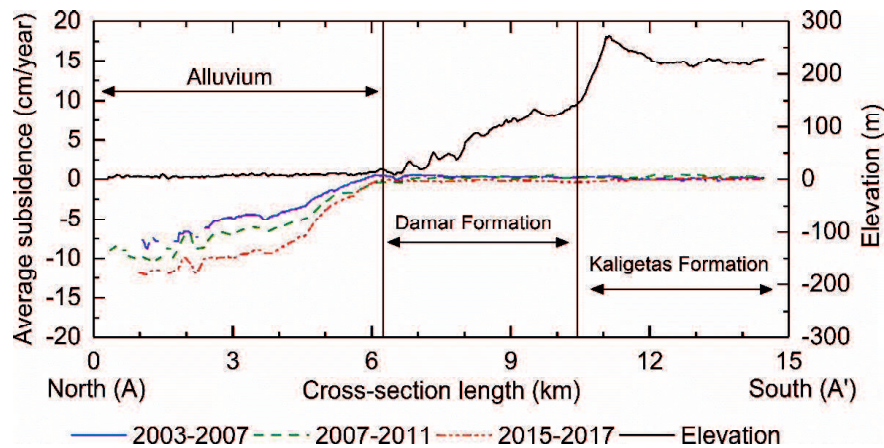
Figure 3.8 Cross-section line (A-A') to show relationship among elevation, geological conditions, and subsidence.

3.4.3 Comparison of results by GPS and SBAS

In order to verify the validity of the SBAS method, the results of SBAS were compared with those of GPS. This kind of validation in Semarang has been conducted by Arimoto et al. (2013) using the 1-year GPS campaign results. In this study, a detailed comparison with the 2-year GPS campaign results is conducted.

The subsidence measurements by GPS were conducted four times between 2008 and 2011 (Abidin et al., 2013). Thirty-three GPS measurement points were set up in 2008, and eleven additional points were set up in 2009. The locations of all the GPS measurement points are shown in Figure 3.1. The subsidence by the SBAS is calculated using Eq. (3.1) and the LOS displacement, which was extracted from the pixels including the location of a GPS measurement point.

A comparison of the two sets of results is shown in Figures 3.9 and 3.10 for the subsidence from 2008-2009 and from 2009-2010 with the correlation between the SBAS results and the GPS results at all the GPS measurement points, respectively. Point SMG1 was taken as the reference point, which was installed in the firm ground located in the south area of the Kaligetas Formation far from the coastal area. The subsidence at all the measurement points is relative to the reference point. Figure 3.9 shows a comparison of the subsidence from 2008-2009. It can be seen that the largest difference is 9.1 cm at point SP05 and the smallest is 0.2 cm at point BM05 with the root square mean error (RMSE) of 3.3 cm. The correlation value for both results during this period is

0.67. Figure 3.10 shows a comparison of the subsidence from 2009-2010. It can be seen that the largest and smallest differences are 4.4 cm and 0.1 cm, respectively, which correspond to points SP05 and BM01, respectively. The RMSE for this period is 2.5 cm with a correlation value of 0.88. It is found that the results of SBAS agree well with those of GPS within a few centimeters as the RMSE, and the validity of the SBAS method was confirmed.

The big difference between the GPS and the SBAS results, like at point SP05, could have been caused by several factors, such as the local site conditions that influence the GPS measurements, the ground surface conditions that effect the SBAS results, etc. The GPS measurements at this point have a larger standard deviation than the other points due to a signal obstruction (Abidin et al., 2013). The difference between the results of DInSAR and GPS is known to be within a few centimeters, as the RMSE (Liu et al., 2015; López-Quiroz et al., 2009; Luo et al., 2014). Therefore, it is found that the SBAS results in this study are acceptable.
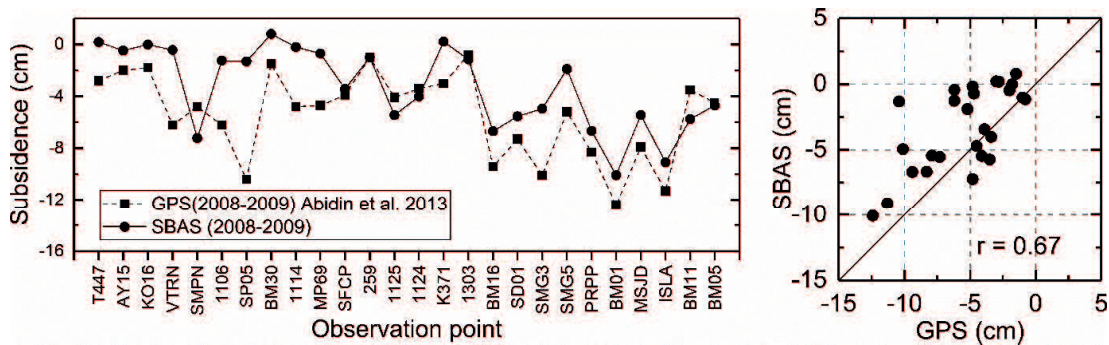
Figure 3.9 Comparison of SBAS and GPS results at GPS observation points from 2008-2009.
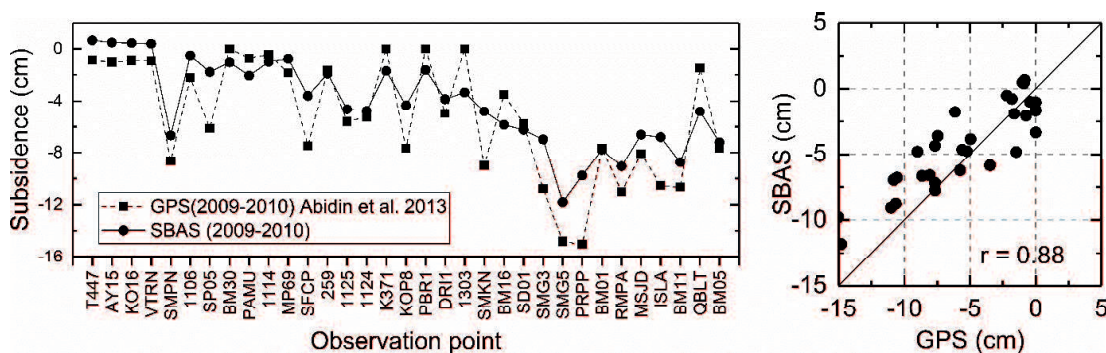
Figure 3.10 Comparison of SBAS and GPS results at GPS observation points from 2009-2010.

3.5 Time transition of subsidence

As seen in the above section, the subsidence for the three different periods, i.e., 2003-2007, 2007-2011, and 2015-2017, were obtained independently by different SAR satellites. In order to obtain the time transition of the subsidence for the whole period, 2003-2017, the three sets of

results should be continuously connected. A research was conducted in Tucson, Arizona (Kim et al., 2015) in which the results were linearly connected under the assumption that the annual rate of subsidence was constant. However, the annual rate of subsidence is not always constant; it often changes with time and varies spatially.

The behavior of the subsidence in Semarang is mainly caused by water extraction activities (Marfai and King, 2007; Putranto and Rüde, 2016), and it is based on the consolidation phenomenon. In this study, the hyperbolic method (Tan et al., 1991), which was proposed to analyze the consolidation subsidence, is employed as a simple method to connect the subsidence for the three different periods and to smooth the results of SBAS in the area of Alluvium.

3.5.1 Hyperbolic method for subsidence analysis

The hyperbolic method (HM) was proposed to analyze the subsidence by consolidation (Tan et al., 1991). It is well known that analyzing and predicting the consolidation subsidence is often difficult in practice because of the complexity of the actual ground conditions. The method was proposed for simply analyzing the settlement data in the field so as to evaluate the behavior and to estimate the subsequent subsidence. It is capable of being applied to infinitesimal and finite strain consolidation and is able to yield reasonable estimates for the settlement of various types of consolidation.

The hyperbolic equation used in the HM is represented as follows:

$$S_t = S_{t_i} - \left(\frac{t - t_i}{\alpha + \beta(t - t_i)} \right) \tag{3.2}$$

where S_t and S_{t_i} are the subsidence at time t and initial time t_i (starting time to be applied), respectively, and α and β are constants to be determined by fitting the measured subsidence. The initial tangent gradient of the subsidence represented by Eq. (3.2) is $\frac{1}{\alpha} \left(= \left(\frac{dS}{dt} \right)_{t=t_i} \right)$, and S_t becomes the final value of subsidence, $S_f = S_{t_i} - 1/\beta$, when time t goes to infinity in Eq. (3.2). Parameters α and β are related to the rate and the convergence value of the subsidence, respectively (see Figure 3.11).

In order to apply the HM to the results of SBAS, Eq. (3.2) is modified as follows:

$$-\left(\frac{t - t_i}{S_t - S_{t_i}} \right) = \alpha + \beta(t - t_i) \tag{3.3}$$

where t_i and t are the acquisition dates of the first SAR data and the subsequent SAR data, respectively. S_{t_i} and S_t represent the subsidence at times t_i and t, respectively. By taking Eq. (3.3) as an observation equation and applying the least squares method to the measured subsidence, α and β can be determined. Figure 3.11 shows a schematic illustration of the HM.
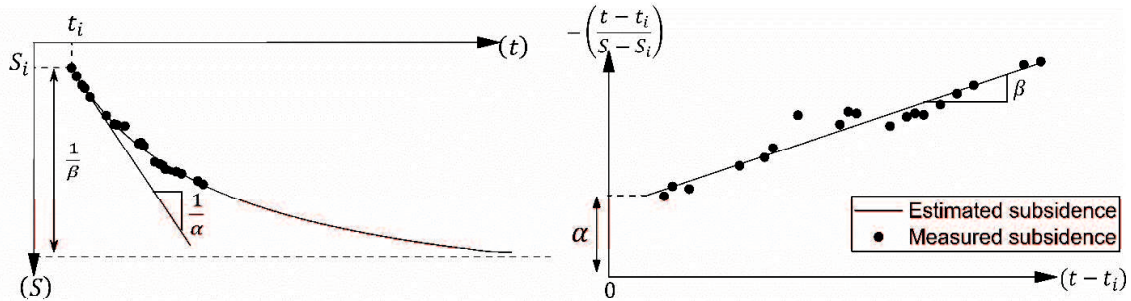
Figure 3.11 Schematic representation of hyperbolic method.

3.5.2 Continuous measurement results of Envisat-ASAR, ALOS-PALSAR, and Sentinel-1A

The HM described in section 3.5.1 is applied to the SBAS results in the area of Alluvium for the three periods, (I) 2003-2007, (II) 2007-2011, and (III) 2015-2017, respectively. The subsidence is extracted from the pixels that include the GPS measurement points.

Table 3.2 presents the results of α and β for each period. The upper suffix $\cdot^{(*)}$ represents data periods (I), (II), and (III). For example, $S_t^{(I)}$, $t_i^{(II)}$, and $\alpha^{(III)}$ mean the subsidence represented by the hyperbolic equation in Period (I), the initial date in Period (II), and parameter α in Period (III), respectively. The locations of the pixels are almost at the same positions as the GPS measurement points, as shown in Figure 3.1.

Figure 3.12 shows the transition of the subsidence at several pixels as examples drawn by the hyperbolic curves using parameters α and β, as shown in Table 3.2. The subsidence by SBAS is also plotted there. The results are denoted in blue, green, and red for the three periods, (I), (II), and (III), respectively. From Figure 3.12, it is found that the subsidence at SMPN, BM16, DRI1, 1124, 1125 SMG5, and RMPA increased with time and the rate of the subsidence also increased. Actually, parameter α decreased with Periods (I), (II), and (III) ($\alpha^{(I)} > \alpha^{(II)} > \alpha^{(III)}$ in Table 3.2). This means that the initial tangent gradient of the subsidence increased ($1/\alpha^{(I)} < 1/\alpha^{(II)} < 1/\alpha^{(III)}$) and then the subsidence accelerated. Only the subsidence at 1106 seems to have remained stable.

Table 3.2 Results of hyperbolic method (HM) applied to SBAS results.

		(I)2003-2007 $t_i^{(I)}$ = $12Mar2003$ $S_{t_i}^{(I)} = 0$		(II)2007-2011 $t_i^{(II)}$ = $21Jan2007$ $S_{t_i}^{(II)} = S_{t=t_i^{(II)}}^{(I)}$		(III)2015-2017 $t_i^{(III)}$ = $26Jan2015$ $S_{t_i}^{(III)} = S_{t=t_i^{(III)}}^{(II)}$		Type of subsidence behavior (A or B, see 3.5.2)
Initial date **Initial subsidence** **Pixel name**		$\alpha^{(I)}$	$\beta^{(I)}$	$\alpha^{(II)}$	$\beta^{(II)}$	$\alpha^{(III)}$	$\beta^{(III)}$	
Group (1)	CTRM	72.698	0.0057	44.748	0.0074	33.746	0.0003	A
	BM16	69.914	0.0007	47.097	0.0082	38.722	0.0078	A
	RMPA	43.39	0.0122	39.397	0.001	22.632	0.0068	A
	BM01	53.923	0.0025	43.302	0.0027	27.496	0.0082	A
	JOHR	67.114	0.0097	55.511	0.001	32.551	0.0054	A
	SFCP	143.36	0.0074	96.756	0.0017	61.013	0.0008	A
	SMG5	40.593	0.0173	30.386	0.0084	20.978	0.0056	A
	SMPN	37.668	0.0214	43.221	0.0073	34.694	0.004	A
	SP05	52.823	0.3835	192.88	0.0099	97.057	0.0979	B
	DRI1	93.756	0.0073	55.476	0.0119	48.445	0.001	A
	1106	289.41	0.1749	132.62	0.2046	150.74	0.0977	B
	1124	121.07	0.0055	70.571	0.0072	41.344	0.0116	A
	1125	105.24	0.0065	75.651	0.0016	43.507	0.0055	A

		(I)2003-2007 $t_i^{(I)}$ = $12Mar2003$ $S_{t_i}^{(I)} = 0$		(II)2007-2011 $t_i^{(II)}$ = $21Jan2007$ $S_{t_i}^{(II)} = 0$		(III)2015-2017 $t_i^{(III)}$ = $26Jan2015$ $S_{t_i}^{(III)} = S_{t=t_i^{(III)}}^{(II)}$		Type of subsidence behavior (A or B see 3.5.2)
Initial date **Initial subsidence** **Pixel name**		$\alpha^{(I)}$	$\beta^{(I)}$	$\alpha^{(II)}$	$\beta^{(II)}$	$\alpha^{(III)}$	$\beta^{(III)}$	
Group (2)	BM11			39.208	0.0076	35.925	0.0085	A
	ISLA			42.702	0.0059	24.843	0.0093	A
	MSJD			56.7	0.0036	28.334	0.0134	A
	PRPP			45.811	0.0005	35.38	0.0131	B
	SD01	N/A		35.324	0.0178	34.202	0.0091	A
	SD02	(No SAR data in		374.26	0.1167	73.723	0.1108	B
	SMG3	this area. See Fig.		56.228	0.0041	36.391	0.0089	A
	SMKN	5)		77.056	0.0045	36.028	0.0156	A
	K370			89.765	0.0014	43.187	0.0259	B
	KOP8			56.444	0.0244	38.857	0.0231	A
	PBRI1			111.52	0.0189	55.129	0.177	B
	QBLT			141.01	0.0352	61.5	0.0424	A

The HM is not applied to the SBAS results in the area of the Damar and Kaligetas Formations, because subsidence caused by consolidation does not occur in such rock formations. A linear regression is used to connect the SBAS results. The subsidence transitions at K016 and PAMU are shown in Figure 3.13. They are very small at less than 2 cm over a period of four years. The behavior is stable.
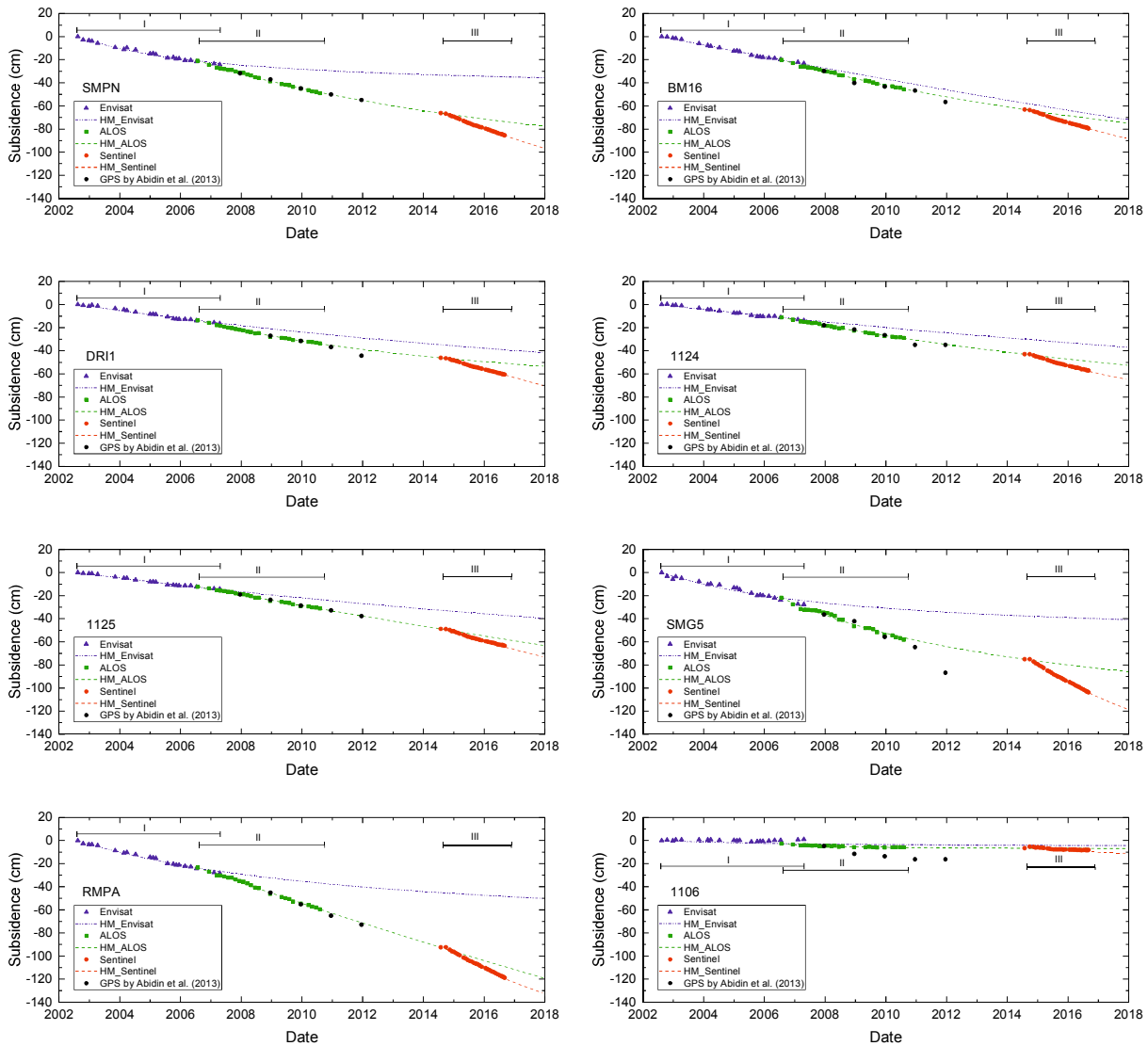
Figure 3.12 Long-term subsidence using hyperbolic method in area of Alluvium.

To confirm the validity of the connection using the HM, the estimated subsidence by the HM and GPS measurement results are compared during the unlinked period from February 2011 to January 2015. The results of the GPS campaign by the third author and his colleagues are also plotted in Figure 3.12. The results of the HM (dotted green line in Figure 3.12) and GPS (bullets in Figure 3.12) show a good agreement, except at SMG5 and 1106. The HM can provide good

estimates of the subsidence in the un-linked period between (II) and (III). Results for the other points are plotted in Figure 3.13.

Figure 3.13 Long-term subsidence using hyperbolic method at GPS points.
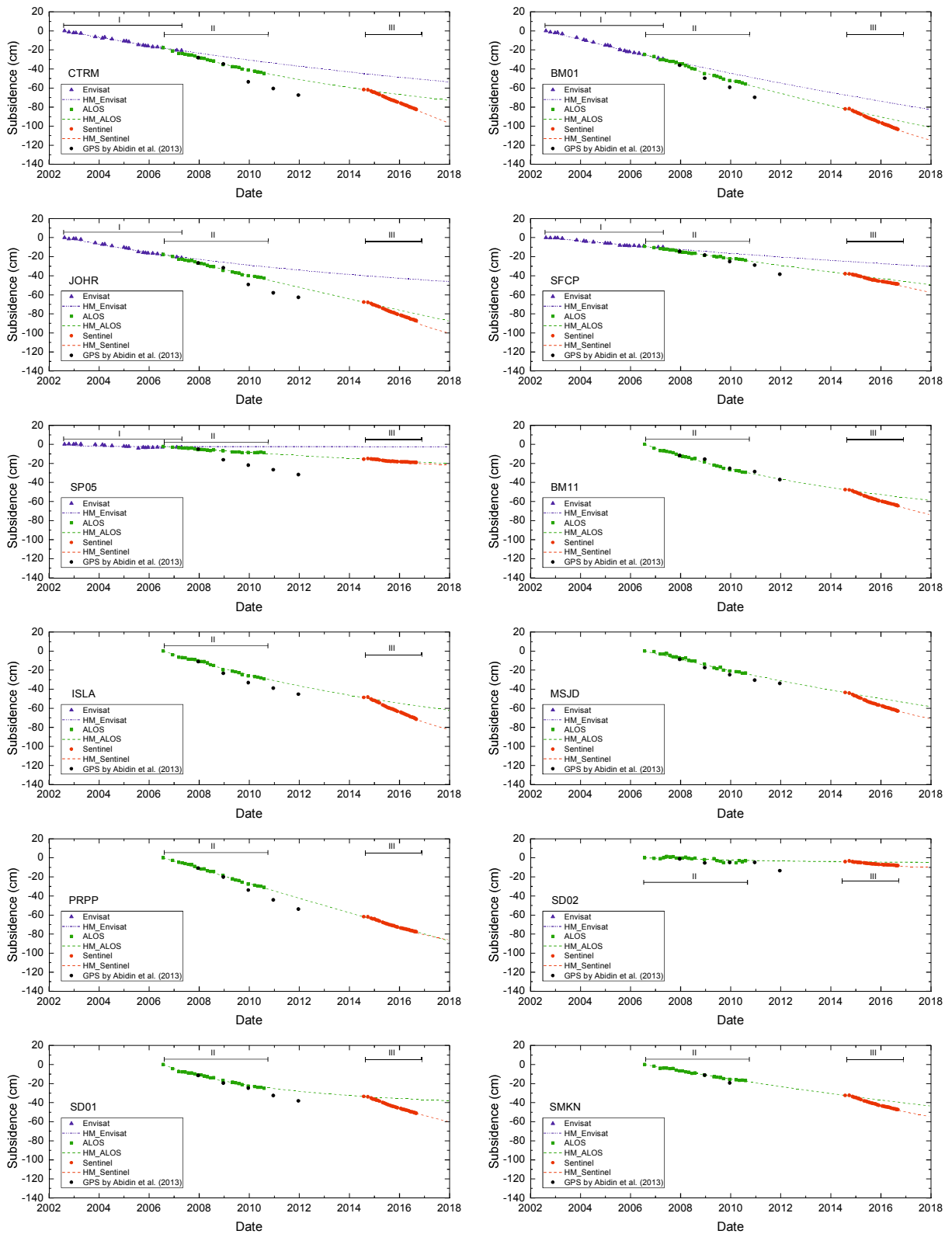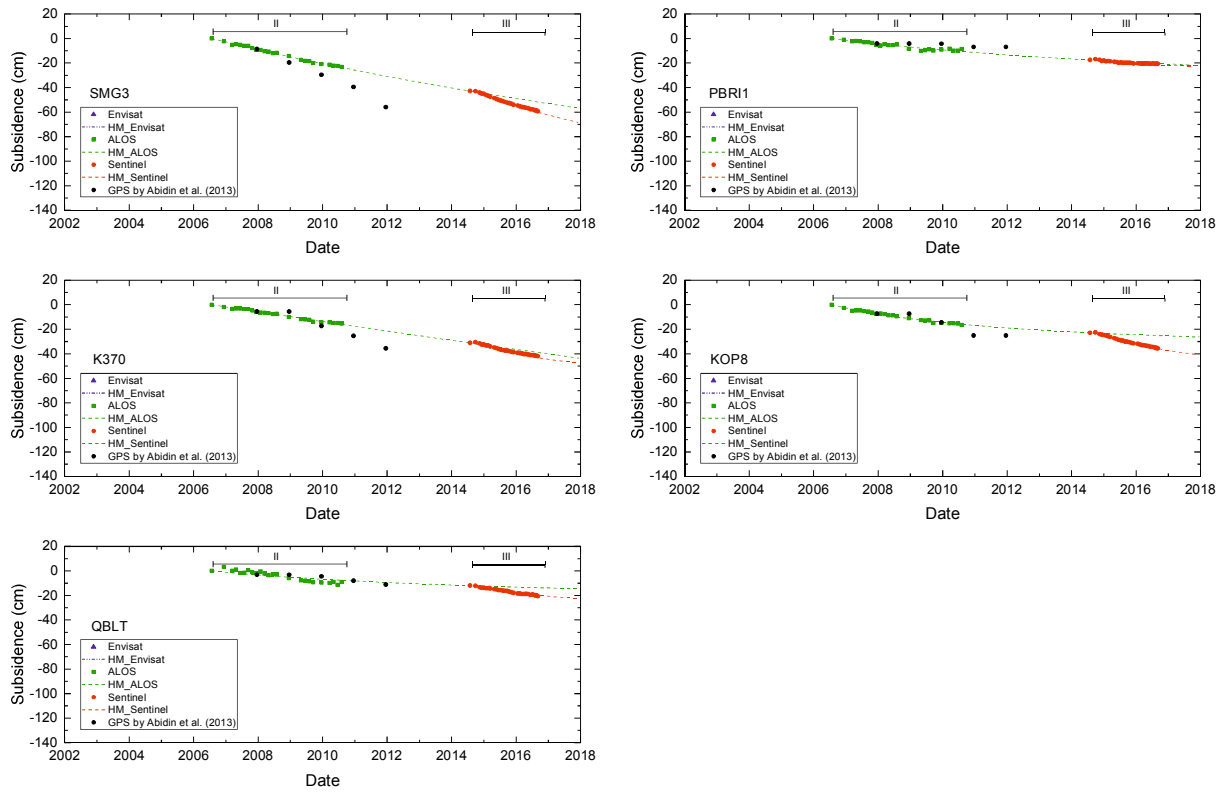
It is found that the HM could be useful for concatenating the results by different SAR satellites in different periods, and the subsidence could be evaluated as long-term continuous monitoring results. The GPS results in the area of the Damar Formation are also plotted in Figure 3.14 produced by a linear regression. The results also show a good agreement.
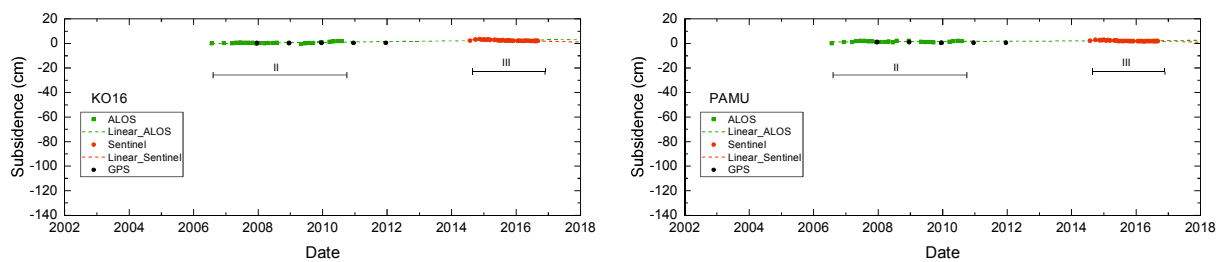
Figure 3.14 Transition of subsidence at very small subsidence points.

3.6 Discussions

From the results in 3.5.2, the subsidence behavior from 2003-2017 is classified into three types: (1) Type A: subsidence with an increasing rate (accelerated subsidence), e.g., SMPN, BM16, DRI1, 1124, 1125 SMG5, and RMPA in Figure 3.12, (2) Type B: subsidence with a constant rate, e.g., 1106 in Figure 3.12, and (3) Type C: very small subsidence, e.g., KO16 and PAMU in Figure 3.14. The three types are written in Table 3.2 and plotted in Figure 3.15. Type

A" is located mainly in the northeast Alluvium area. "Type B" is seen along the border between the Alluvium and the Damar Formation. "Type C" mainly lies in the Damar Formation. The distribution of the types of subsidence corresponds to the geological features. The subsidence of "Type A" exhibits acceleration behavior.
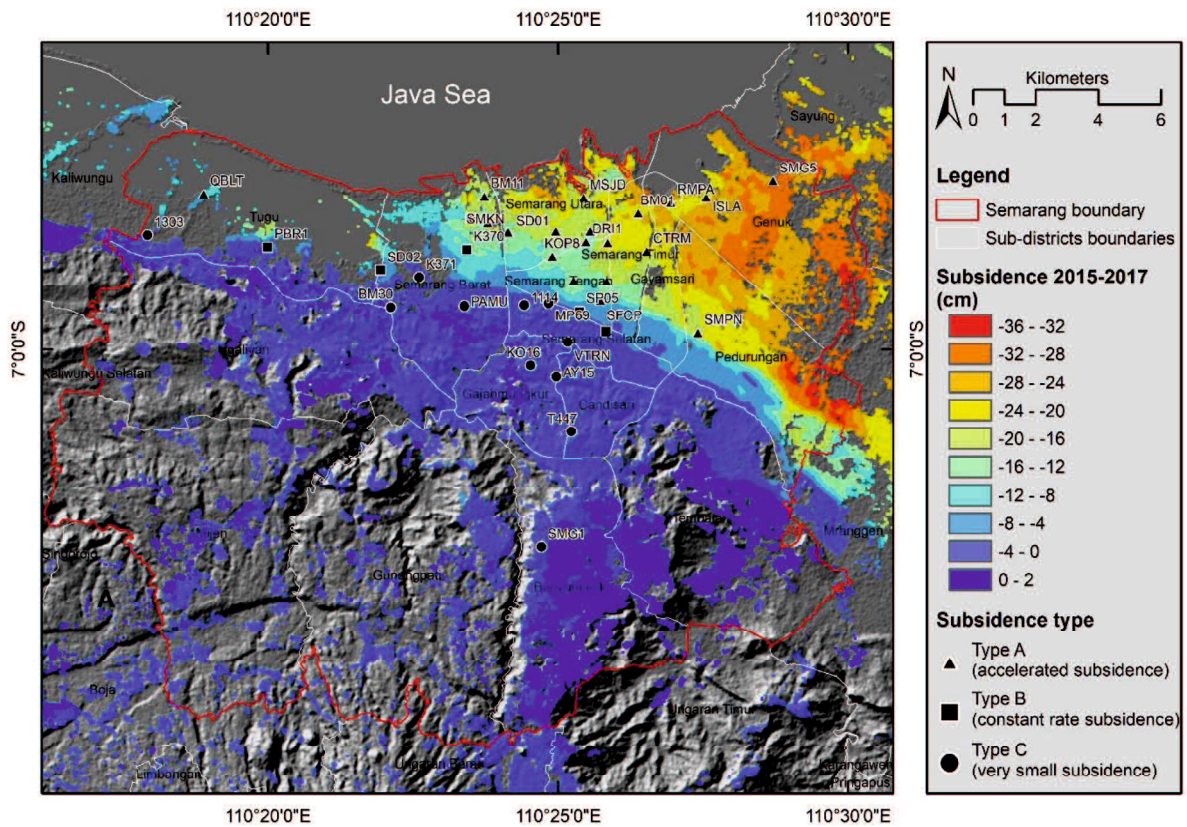
Figure 3.15 Classification of subsidence types using hyperbolic method.

A numerical analysis of the subsidence in Semarang was conducted in 2011 by Sarah et al. (2011). They predicted that the subsidence would stop by 2016 under the assumption that the groundwater extraction activities would be halted in 2010. However, according to the SBAS results and the transition of subsidence "Type A" shown in this study, subsidence is still ongoing even today and has increased significantly. Accelerated subsidence (Type "A"), as seen in Figures 3.12 and 3.13, can be caused by continuous groundwater extraction.

As stated in Volentino (2013), industries in Semarang mainly use groundwater for their activities. The groundwater has been exploited as a natural resource since 1841 (Putranto and Rüde, 2016) and its consumption has been increasing rapidly over the last decade (Marfai and King, 2007). Figure 3.16 shows the number of registered deepwater wells and the total extraction in the Semarang-Demak groundwater basin (Putranto and Rüde, 2016) and (Semarang

Municipality Government, 2015). Since 1999, the yearly extraction of groundwater has been constant, except for in 2004, and it increased a little in 2010. During 2011-2013 the amount of groundwater extraction increased rapidly. The results are shown in Figure 3.12; the recent acceleration behavior seems to be particularly related to the trend in groundwater extraction activities.
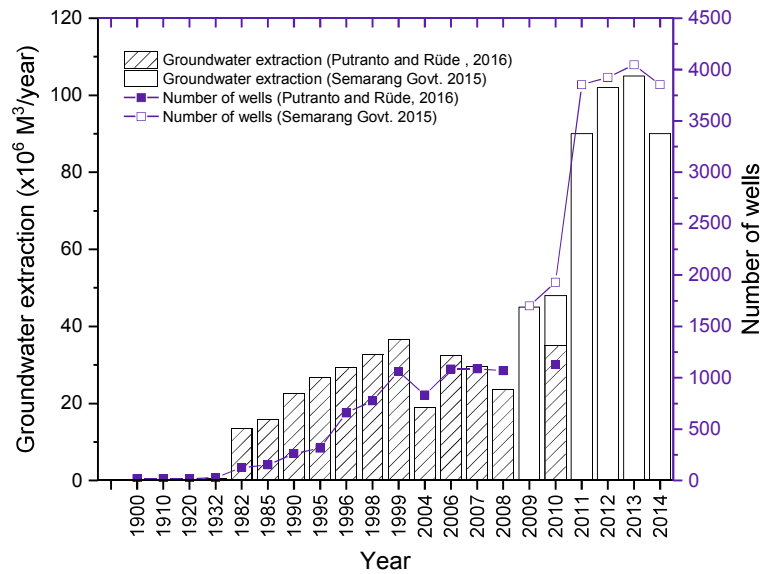
Figure 3.16 Number of registered deep wells and total extraction in Semarang-Demak groundwater basin (Putranto and Rüde, 2016) and (Semarang Municipality Government, 2015).

These results agree well with those of previous researches which found a strong correlation between groundwater subsidence extraction and the subsidence phenomenon in this region (Chaussard et al., 2013; Marfai and King, 2007; Yuwono et al., 2013). Large subsidence of up to 24-36 cm during the period of 2015 to 2017 is found at some locations in the sub-districts of Pedurungan, Genuk, and Sayung. The effect of groundwater extraction activities can lead to the severe subsidence that has also been reported by other researchers who conducted subsidence observations in many other megapolitan cities in countries such as Mexico, Italy, USA, China, and Turkey (Caló et al., 2017; Gao et al., 2016; Kim et al., 2015; Liu et al., 2015; López-Quiroz et al., 2009; Raucoules et al., 2007).

Based on the experience of large cities in Japan, that were facing a subsidence problem, it is seen that halting the groundwater extraction activities plays a key role in stopping the subsidence. Figure 3.17 shows the temporal behavior of the subsidence in some cases in Japan (Ministry of the Environment, 2016). The longest observation was conducted in the Kanto Plain; it was started in 1892. During the observation periods, there were some major events, namely, (a)

the start of the excavation of deep wells, (b) the Kanto earthquake, (c) the beginning of World War II (WWII), (d) the establishment of the industrial water law, (e) the establishment of the building water law, (f) the establishment of the basic law for environmental pollution control, (g) the establishment of guidelines on measures for the prevention of ground subsidence in Chikugo, Saga Plain, and Nobi Plain, and (h) the establishment of guidelines on measures for the prevention of ground subsidence in the North Kanto Plain. Stopping or restricting groundwater extraction can lead to stable subsidence behavior.
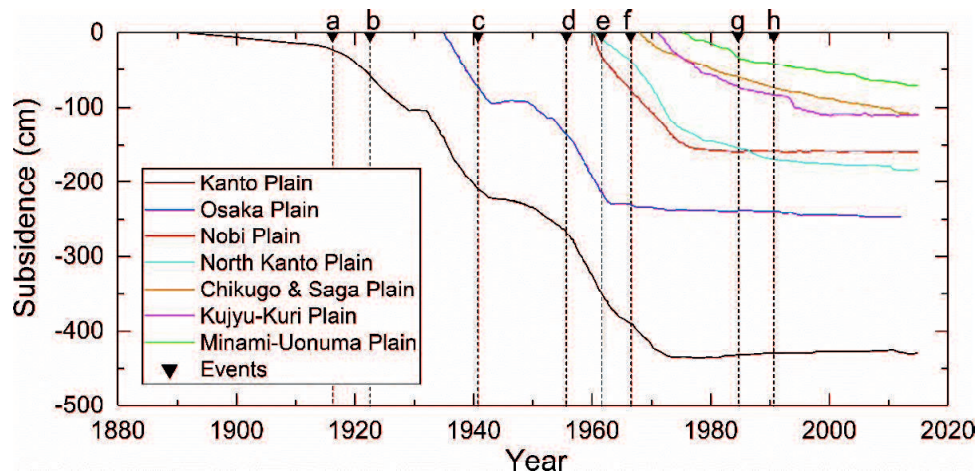
Figure 3.17 Changes in long-term subsidence in representative areas of Japan (Ministry of the Environment, 2016).

A field observation of Semarang was conducted as part of this study in March and August 2017 to discover the impact of the ground subsidence. Figure 3.18 shows several photos taken in the north part of the coastal area (additional photos are presented in appendix 1). The ground level is below the high tide level particularly on the north shore, which makes those areas prone to flooding. In addition, many buildings and infrastructures have been damaged. This subsidence phenomenon has led to tremendous economic losses, and it is the citizens with a low economic level who have suffered the most (Andreas et al., 2017; Gumilar et al., 2013; Marfai et al., 2008). In order to establish a mitigation plan, subsidence monitoring should be continued. It is found from this study that employing DInSAR, along with the SBAS method, is useful for realizing such a mitigation plan. In addition, the subsidence information by DInSAR has been found to be useful for the assessment of a coastal vulnerability index (CVI) in Semarang (Husnayaen et al., 2018); therefore, subsidence monitoring needs to be continued.

Figure 3.18 Some impacts of subsidence in Semarang investigated by the author in March and August 2017.

3.7 Summary of chapter 3

In this study, long-term subsidence monitoring in Semarang, Indonesia has been conducted by means of the multi-temporal DInSAR analysis with the SBAS method using multi-sensor SAR data sets (i.e., Envisat-ASAR, ALOS-PALSAR, and Sentinel-1A).

The conclusions are as follows:

- The time series for the subsidence distribution map of Semarang for a period of 14 years (2003-2017) has been obtained. It provided the distribution of subsidence in space and the transition of the time series.

- It was found that the north part of the city is severely affected by the subsidence. Some places in the sub-districts of Pedurungan, Genuk, and Sayung have experienced the largest subsidence, namely, in the order of up to 24-36 cm during the period of two years from 2015-2017.

- The distribution of subsidence is closely related to the geological conditions. The northeast area is composed of the Alluvium exposed to large subsidence. The subsidence also increased around the boundary between the Alluvium and the Damar Formation. There was almost no subsidence in the area of the Damar Formation. The subsidence gradually became larger from Period (I) (2003-2007) to Period (III) (2015-2017) through Period (II) (2007-2011).

- The validity of the SBAS results was confirmed through the use of two years of GPS campaign results, from 2008-2010. The root mean squares of the difference between the DInSAR with SBAS and the GPS results were found to be a few centimeters, and the two

sets correlate well. However, the monitoring period of SAR is limited by both the lifespan of the satellites and the lack of SAR data during a certain period.

- In order to overcome the above problems, the hyperbolic method was used to connect the different SBAS DInSAR results in different periods. The connected long-term subsidence behavior could be classified into three categories: (1) accelerated subsidence, (2) subsidence with constant velocity, and (3) no subsidence.

- According to the other former research, the accelerated subsidence may be related to groundwater extraction activities. In order to clarify the relationship and to form an appropriate mitigation plan, monitoring should be continued.

- It was proven that SBAS DInSAR can be a useful tool for long-term continuous subsidence monitoring.

References

Abidin, H.Z., Andreas, H., Gumilar, I., Sidiq, T.P., Fukuda, Y., 2013. Land subsidence in coastal city of Semarang (Indonesia): Characteristics, impacts and causes. Geomatics, Nat. Hazards Risk 4, 226–240. https://doi.org/10.1080/19475705.2012.692336

Andreas, H., Abidin, H.Z., Gumilar, I., Sidiq, T.P., Yuwono, B., 2017. Adaptation and mitigation of land subsidence in Semarang. AIP Conf. Proc. 1857. https://doi.org/10.1063/1.4987088

Arimoto, M., Yo, F., Manabu, H., Youichiro, T., 2013. Land Subsidence in Semarang, Indonesia, Observed by InSAR Time-Series Analysis Using ALOS/PALSAR Data. J. Geod. Soc. Japan 59, 45–56.

Berardino, P., Fornaro, G., Lanari, R., Sansosti, E., 2002. A new algorithm for surface deformation monitoring based on small baseline differential SAR interferograms. IEEE Trans. Geosci. Remote Sens. 40, 2375–2383. https://doi.org/10.1109/TGRS.2002.803792

BPS, 2016. Semarang Munipacility in Figures. BPS-Statistic of Semarang Municipality, Semarang.

Caló, F., Notti, D., Galve, J.P., Abdikan, S., Görüm, T., Pepe, A., Şanli, F.B., 2017. DInSAR-based detection of land subsidence and correlation with groundwater depletion in konya plain, Turkey. Remote Sens. 9. https://doi.org/10.3390/rs9010083

Chaussard, E., Amelung, F., Abidin, H., Hong, S.H., 2013. Sinking cities in Indonesia: ALOS PALSAR detects rapid subsidence due to groundwater and gas extraction. Remote Sens. Environ. 128, 150–161. https://doi.org/10.1016/j.rse.2012.10.015

Costantini, M., 1998. A novel phase unwrapping method based on network programming. Geosci. Remote Sensing, IEEE Trans. 36, 813–821. https://doi.org/10.1109/36.673674

Ferretti, A., Prati, C., Rocca, F., 2001. Permanent scatterers in SAR interferometry. IEEE Trans. Geosci. Remote Sens. 39, 8–20. https://doi.org/10.1109/36.898661

Gao, M., Gong, H., Chen, B., Zhou, C., Chen, W., Liang, Y., Shi, M., Si, Y., 2016. InSAR time-series investigation of long-term ground displacement at Beijing Capital International Airport, China. Tectonophysics 691, 271–281. https://doi.org/10.1016/j.tecto.2016.10.016

Goldstein, R.M., Werner, C.L., 1998. Radar interferogram filtering for geophysical applications. Geophys. Res. Lett. 25, 4035–4038. https://doi.org/10.1029/1998GL900033

Gumilar, I., Abidin, H.Z., Sidiq, T.P., Andreas, H., Maiyudi, R., Gamal, M., 2013. Mapping And Evaluating The Impact Of Land Subsidence In Semarang (Indonesia). Indones. J. Geospasial 2, 26–41.

Hanssen, R.F., 2001. Radar Interferometry: Data Interpretation and Error Analysis. Kluwer Academic Publishers, Dordrecht.

Husnayaen, Rimba, A.B., Osawa, T., Parwata, I.N.S., As-syakur, A.R., Kasim, F., Astarini, I.A., 2018. Physical assessment of coastal vulnerability under enhanced land subsidence in Semarang, Indonesia, using multi-sensor satellite data. Adv. Sp. Res. 61, 2159–2179. https://doi.org/10.1016/j.asr.2018.01.026

Jo, M.J., Jung, H.S., Won, J.S., 2017. Measurement of precise three-dimensional volcanic deformations via TerraSAR-X synthetic aperture radar interferometry. Remote Sens. Environ. 192, 228–237. https://doi.org/10.1016/j.rse.2017.02.022

Kim, J.W., Lu, Z., Jia, Y., Shum, C.K., 2015. Ground subsidence in Tucson, Arizona, monitored by time-series analysis using multi-sensor InSAR datasets from 1993 to 2011. ISPRS J. Photogramm. Remote Sens. 107, 126–141. https://doi.org/10.1016/j.isprsjprs.2015.03.013

Kuehn, F., Albiol, D., Cooksley, G., Duro, J., Granda, J., Haas, S., Hoffmann-Rothe, A., Murdohardono, D., 2010. Detection of land subsidence in Semarang, Indonesia, using stable points network (SPN) technique. Environ. Earth Sci. 60, 909–921. https://doi.org/10.1007/s12665-009-0227-x

Lanari, R., Casu, F., Manzo, M., Zeni, G., Berardino, P., Manunta, M., Pepe, A., 2007. An overview of the Small BAseline Subset algorithm: A DInSAR technique for surface deformation analysis. Pure Appl. Geophys. https://doi.org/10.1007/s00024-007-0192-9

Liu, G., Guo, H., Perski, Z., Fan, J., Bai, S., Yan, S., Song, R., 2016. Monitoring the slope movement of the Shuping landslide in the Three Gorges Reservoir of China, using X-band time series SAR interferometry. Adv. Sp. Res. 57, 2487–2495. https://doi.org/10.1016/j.asr.2016.03.043

Liu, J.G., Mason, P.J., 2016. Image Processing and GIS for Remote Sensing, Second. ed. John Wiley & Sons, Singapore.

Liu, Y., Huang, H., Dong, J., 2015. Large-area land subsidence monitoring and mechanism research using the small baseline subset interferometric synthetic aperture radar technique over the Yellow River Delta, China. J. Appl. Remote Sens. 9, 096019. https://doi.org/10.1117/1.JRS.9.096019

López-Quiroz, P., Doin, M.P., Tupin, F., Briole, P., Nicolas, J.M., 2009. Time series analysis of Mexico City subsidence constrained by radar interferometry. J. Appl. Geophys. 69, 1–15. https://doi.org/10.1016/j.jappgeo.2009.02.006

Lubis, A.M., Sato, T., Tomiyama, N., Isezaki, N., Yamanokuchi, T., 2011. Ground subsidence in Semarang-Indonesia investigated by ALOS-PALSAR satellite SAR interferometry. J. Asian Earth Sci. 40, 1079–1088. https://doi.org/10.1016/j.jseaes.2010.12.001

Luo, Q., Perissin, D., Zhang, Y., Jia, Y., 2014. L- and X-band multi-temporal InSAR analysis of tianjin subsidence. Remote Sens. 6, 7933–7951. https://doi.org/10.3390/rs6097933

Marfai, M.A., King, L., 2007. Monitoring land subsidence in Semarang, Indonesia. Environ. Geol. 53, 651–659. https://doi.org/10.1007/s00254-007-0680-3

Marfai, M.A., King, L., Sartohadi, J., Sudrajat, S., Budiani, S.R., Yulianto, F., 2008. The impact of tidal flooding on a coastal community in Semarang, Indonesia. Environmentalist 28, 237–248. https://doi.org/10.1007/s10669-007-9134-4

Massonnet, D., Feigl, K.L., 1998. Radar interferometry and its application to changes in the earth's surface. Rev. Geophys. 36, 441–500. https://doi.org/10.1029/97RG03139

Ministry of the Environment, 2016. Overview of ground subsidence areas throughout the country. Japan.

Moghaddam, N.F., Sahebi, M.R., Matkan, A.A., Roostaei, M., 2013. Subsidence rate monitoring of Aghajari oil field based on Differential SAR Interferometry. Adv. Sp. Res. 51, 2285–2296. https://doi.org/10.1016/j.asr.2013.01.023

Morishita, Y., Kobayashi, T., Yarai, H., 2016. Three-dimensional deformation mapping of a dike intrusion event in Sakurajima in 2015 by exploiting the right- and left-looking ALOS-2 InSAR. Geophys. Res. Lett. 43, 4197–4204. https://doi.org/10.1002/2016GL068293

Putranto, T., Rüde, T., 2016. Hydrogeological Model of an Urban City in a Coastal Area, Case study: Semarang, Indonesia. Indones. J. Geosci. 3. https://doi.org/10.17014/ijog.3.1.17-27

Raucoules, D., Colesanti, C., Carnec, C., 2007. Use of SAR interferometry for detecting and assessing ground subsidence. Comptes Rendus - Geosci. 339, 289–302. https://doi.org/10.1016/j.crte.2007.02.002

Sandwell, D.T., Myer, D., Mellors, R., Shimada, M., Brooks, B., Foster, J., 2008. Accuracy and resolution of ALOS interferometry: Vector deformation maps of the father's day intrusion at Kilauea. IEEE Trans. Geosci. Remote Sens. 46, 3524–3534. https://doi.org/10.1109/TGRS.2008.2000634

Sarah, D., Syahbana, A.J., Lubis, R.F., Mulyono, A., 2011. Modelling of Land Subsidence Along Tanah Mas -Pelabuhan Section Semarang City Using Finite Element Method. J. Ris. Geol. dan Pertamb. 21, 105. https://doi.org/10.14203/risetgeotam2011.v21.50

Sarmap, 2013. SBAS Tutorial, http://www.sarmap.ch/tutorials/sbas_tutorial_V_2_0.pdf.

Semarang Munipalcity Government, 2015. Laporan Keterangan Pertanggungjawaban (LKPJ) Walikota Semarang Akhir Tahun Anggaran 2014. Indonesia

Singhroy, V., Molch, K., 2004. Characterizing and monitoring rockslides from SAR techniques. Adv. Sp. Res. 33, 290–295. https://doi.org/10.1016/S0273-1177(03)00470-8

Tan, T.S., Inoue, T., Lee, S.L., 1991. Hyperbolic method for consolidation analysis. J. Geotech. Eng. 117, 1723–1737. https://doi.org/10.1061/(ASCE)0733-9410(1991)117:11(1723)

Tang, W., Liao, M., Yuan, P., 2016. Atmospheric correction in time-series SAR interferometry for land surface deformation mapping - A case study of Taiyuan, China. Adv. Sp. Res. 58, 310–325. https://doi.org/10.1016/j.asr.2016.05.003

Thaden, R.E., Sumadirja, H., Richards, P.W., 1975. Geologic Map of the Magelang and Semarang Quadrangles, Java (Semarang (sheet 11/XIII-E, 1:100000)). Geological Survey of Indonesia, Bandung.

Volentino, D., 2013. Kajian Pengawasan Pemanfaatan Sumberdaya Air Tanah di Kawasan Industri Kota Semarang. J. Wil. dan Lingkung. 1, 265–274. https://doi.org/https://doi.org/10.14710/jwl.1.3.265-274

Yuwono, B.D., Abidin, H.Z., Hilmi, M., 2013. Geospatial analyze on cause of Subsidence in Semarang (In Indonesian). Proc. SNST-4.

Chapter 4

Monitoring the ground deformation of a volcano with a large height difference in topography

4.1 Introduction

As a country that is located in the "ring of fire", Japan has dozens of active volcanoes. A volcano can be disastrous when it erupts, especially one that lies near a city. Therefore, the monitoring of the volcano's behavior is very important for safety and risk management. The activities of a volcano usually lead to ground surface deformation. Thus, a volcano's behavior can be monitored through the observation of its surface deformation.

Monitoring of the ground surface deformation can be conducted using a traditional measurement method, i.e., leveling, or modern technologies such as GPS. Using the proper GPS method (i.e., the method developed by Shimizu et al., 2014) for surface displacement monitoring enables the yielding of continuous and highly accurate results. However, the method necessitates the installation of GPS sensors at the monitoring site. The installation and maintenance of the devices on the ground involve high costs and a great labor force. In addition, the installation and maintenance of the devices under tough and harsh conditions, like active volcanoes, can be dangerous.

SAR (Synthetic Aperture Radar) is a radar device that is mounted on an aircraft or an artificial satellite (Hanssen, 2001). It transmits pulse waves to the Earth's surface and receives the reflections. DInSAR (Differential Interferometric SAR) has been recognized as an effective tool for measuring ground surface deformation over vast areas. It can provide 2D deformation maps with moderate accuracy (Massonet and Feigl, 1998). In addition, it does not require the installation of any devices on the ground. This means that the monitoring can be conducted anywhere as long as the SAR data are available. Measurements using DInSAR can be conducted frequently based on the SAR satellite revisit time in the target area. Moreover, its accuracy can be improved by conducting a time-series analysis.

Besides DInSAR's superiority for ground deformation monitoring, it also has demerits. For example, DInSAR can be prone to atmospheric disturbances. If the atmospheric effects are random in time, they can be reduced with a time-series analysis (e.g., using SBAS) by stacking or averaging the results. However, seasonal effects and stratified tropospheric delays cannot be

51

successfully removed. Various methods have been developed for mitigating the atmospheric effects on InSAR measurements based on external data such as ground meteorological observations, GPS data, satellite water vapor products, like those from Medium Resolution Imaging Spectrometer (MERIS) and Moderate Resolution Imaging Spectroradiometer (MODIS), and results from numerical meteorological modeling (Shimada, 1999; Ding et al., 2008). In general, these methods are divided into two groups: empirical and predictive (Jolivet et al., 2011). All the methods have merits and demerits, but generally they seem to be too complicated for most users, except for specialists of DInSAR. This study proposes two simple methods for correcting tropospheric delays that are easy to apply. One active volcano in Japan, "Sakurajima", is taken as the study area to prove the applicability of the proposed methods.

4.2 Study area and data collection

4.2.1 Study area
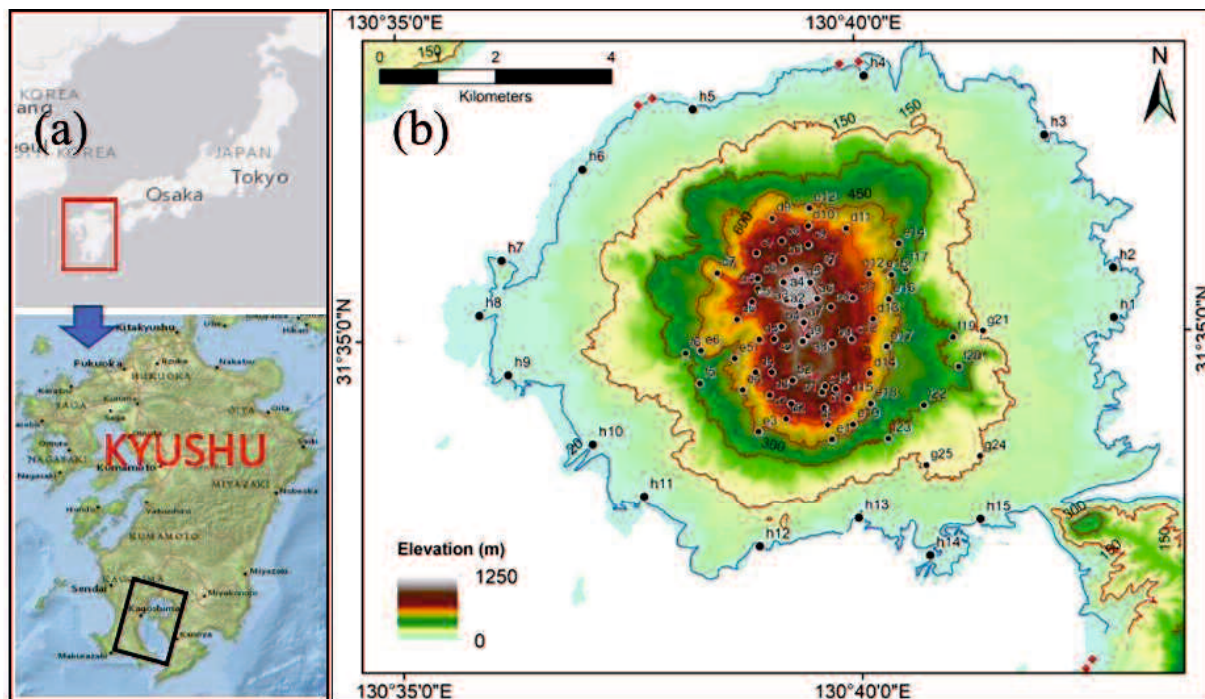
Figure 4.1 (a) Location of Sakurajima Volcano and **(b)** elevation map of Sakurajima Volcano in planar projection JGD2011_UTM Zone 52N (Modified from Geospatial Information Authority of Japan (GSI), 2018).

The study area is Sakurajima Volcano. Sakurajima Volcano is one of the most active volcanoes in Japan; it lies in the southern part of Kyushu Island (see Figure 4.1). It has been monitored by GNSS (GPS) continuous observation, seismometer measurements, and many other instruments. From the monitoring results, it was reported that the body of Sakurajima rapidly

expanded in August 2015 (Japan Meteorological Agency, 2015). Figure 4.1 shows the location of Sakurajima Volcano and an elevation map provided by the Geospatial Information Authority of Japan (GSI). The blue line on the elevation map represents the altitude of 20 m. The red lines are the contour lines for the interval of 150 m. The black points are the sample points at which the displacements are later taken by a DInSAR analysis. The red points are the ground control points (GCPs) that are employed in the time-series DInSAR processing. The average elevation of the GCPs is around 20 m from the mean sea level.

4.2.2 Data collection

This study uses the Sentinel-1A SAR data for the DInSAR time-series analysis. Fifty-four SAR images, acquired from Nov 2014 to August 2017, are used. The SAR images were gathered for path number 163 along a descending passage and right-looking observations. The Digital Elevation Model (DEM), with a mesh of 10 m, is used to remove the topography component in DInSAR. In addition, hourly meteorological data (i.e., air pressure, temperature, and humidity) taken at Kagoshima Station are used to estimate the tropospheric delays. All the Sentinel-1A data were provided by the European Space Agency (ESA). The DEM and meteorological data were provided by the GSI and the Japan Meteorological Agency (JMA), respectively.

4.3 Proposed correction methods for reducing errors caused by tropospheric delays

Based on the long experiences on research of GPS displacement monitoring, it is found that GPS measurement results are severely affected by tropospheric delays and that such errors can be reduced by using an appropriate tropospheric delay model together with meteorological conditions (Shimizu et al., 2014). Tropospheric delays are related to temperature, humidity, and atmospheric pressure. They also have seasonal behavior. In addition, tropospheric delays have a correlative relationship with the difference in height between each measurement point and the reference point (Nakashima et al., 2014).

Since SAR operates in the microwave band (i.e., similar to GPS), this phenomenon is likely to occur in the same way as DInSAR. The stacking independent SAR data approaches (e.g., SBAS method) can successfully reduce the errors caused by temporally random tropospheric delays. However, these approaches neglect biases due to data sampling and to temporally correlated stratified tropospheric delays (Doin et al., 2009).

Therefore, this study employs an idea which the authors developed for reducing the errors caused by tropospheric delays, and proposes the following two methods for DInSAR analysis:

a. Correction by directly using the measured values (method 1)

The procedure for method 1 is as follows:

1. Extract LOS displacements at several points at the same elevation from the SBAS results during a period in which no displacement occurs. For example, extract measured displacements at 10 points at the elevation of 900 m.

2. Collect similar displacement behavior and assume that those displacements are caused only by tropospheric delays. Take the average of the measured displacements at those points and use it as the correction value (*CVM1*) for that elevation.

3. Subtract this correction value from the measured displacements at any point at the same elevation.

4. Repeat Steps 1-3 for other elevations.

b. Correction by using the physical model (method 2)

In method 2, the Hopfield model (Hoffmann-Wellenhoft et al., 1992), representing tropospheric delays, is used to estimate the Zenith Tropospheric Delay (ZTD). The Hopfield model requires meteorological data (i.e., temperature, humidity, and atmospheric pressure) in order to estimate the delay of the microwave. The Zenith Tropospheric Delay can be expressed by Eq. (4.1):

$$\text{ZTD}(h) = 10^{-6} N_{d0}^{\text{trop}} \int_h^{hd} \left(1 - \frac{h}{h_d}\right)^4 dh + 10^{-6} N_{w0}^{\text{trop}} \int_h^{hw} \left(1 - \frac{h}{h_w}\right)^4 dh$$

$$= \frac{10^{-6}}{5} \left\{ N_{d0}^{\text{trop}} h_d \left(1 - \frac{h}{h_d}\right)^5 + N_{w0}^{\text{trop}} h_w \left(1 - \frac{h}{h_w}\right)^5 \right\} \tag{4.1}$$

where $h_d = 40136 + 148.72(T - 273.16)\,(m)$ is the dry part of the atmosphere and $h_d = 11000\,(m)$ is the wet part of the atmosphere. The corresponding dry component is

$$N_{do}^{\text{trop}} = c_1 \frac{p}{T} \qquad\qquad c_1 = 77.64 \left(\frac{K}{\text{hpa}}\right) \tag{4.2}$$

where p is the atmospheric pressure in hector pascal (hpa) and T is the temperature in Kelvin (K). The wet component was found to be

$$N_{wo}^{\text{trop}} = c_2 \frac{e}{T} + c_3 \frac{e}{T^2} \qquad\qquad c_2 = -12.96 \left(\frac{K}{\text{hpa}}\right) \qquad c_3 = 3.718 \cdot 10^5 \left(\frac{K^2}{\text{hpa}}\right)$$

$$e = 6.112 \left(\frac{RH}{100}\right) \exp\left(\frac{(17.62T-4813)}{(T-30.03)}\right) \qquad (4.3)$$

The ZTD difference (ZTDdiff) between each measurement point and the reference point (GCPs) is calculated using Eq. (4.4):

$$\text{ZTDdiff} = \text{ZTD}(h + \Delta h) - \text{ZTD}\ (h) \qquad (4.4)$$

By inserting Eq. (4.1) into Eq (4.4), and considering the first order approximation by disregarding the higher orders of (h/h$_w$) and (h/h$_d$), ZTDdiff can be approximated by Eq (4.5):

$$\text{ZTD}_{\text{diff}} = 10^{-6}(N_{d0}^{\text{trop}} + N_{W0}^{\text{trop}})\Delta h \qquad (4.5)$$

where h is the GCP elevation and Δh is the difference in elevation between the measurement point and GCP. The procedure for method 2 is as follows:

1. Extract LOS displacements at several points at the same elevation from the SBAS results during a period in which no displacement occurs.
2. Collect similar displacement behavior and take the average of the measured displacements at those points. The average value is denoted by $CVM1_H$.
3. Repeat Steps 1 and 2 for several elevations (e.g., every 150 m).
4. Calculate ZTDdiff for each elevation using the meteorological data observed at a reference point. Take the correlation between the average measured value $CVM1_H$ and ZTDdiff.
5. Obtain the following correlation equation for each elevation:

$$CVM1_H = a_H \cdot ZTDdiff_H + b_H \qquad (4.6)$$

   Subscript H in Eq. (4.6) represents the elevation of each measurement point.
6. Calculate the average of "a_H" as $\bar{a}$ for each elevation. It is found that "b_H" has a linear relationship with elevation H, i.e., $b_H = c \cdot H$, where c is a constant. Finally, obtain the following equation for correction of the tropospheric delay. $CVM2_H$ is the error correction value.

$$CVM2_H = \bar{a} \cdot ZTDdiff_H + (c \cdot H) \qquad (4.7)$$

7. Subtract $CVM2_H$ from the LOS displacement to provide the final results.

Method 1, using $CVM1$, is a completely empirical method employing measured displacements. On the other hand, method 2, using Eq. (4.7), is a semi-empirical method associated with the tropospheric delay model and meteorological data.

4.4 Results and discussions

4.4.1 Displacement monitoring using SBAS

Fifty-three LOS displacement maps were generated from 21 November 2014 to 25 August 2017. Figures 4.2 (a)-(d) show four examples of the LOS displacement maps. The LOS displacement values lie in the range of -150 mm to 150 mm; they are presented by colors ranging from red to blue. The white color means no data due to low coherence or a sea area. Positive values mean that the LOS component of the ground surface movement shrunk toward the satellite and vice versa. Figure 4.2 (a) shows the cumulative LOS displacement from 21 November 2014 to 3 December 2014. The color in Figure 4.2 (a) is mainly green; this means that the LOS displacement is very small. Figures 4.2 (b), (c), and (d) have the same color and meaning as Figure 4.2 (a); they represent the cumulative LOS displacements from 21 November 2014 to 24 August 2015, to 18 August 2016, and to 25 August 2017, respectively.

In Figure 4.2 (b), a large LOS displacement is detected in the dark blue area surrounded by a black circle. This behavior is supposed to have been caused by the accumulation of volcanic deposits due to the Sakurajima eruption that occurred in August 2015. The light blue color, found in the area with the elevation of 600 m and beyond, means that the ground surface in that area seems to have heaved up slightly. In Figures 4.2 (c) and (d), the blue color for the elevation beyond 300 m becomes darker. This means that the ground surface continuously moved toward the satellites during that period. However, the blue color in the black circle area becomes lighter. This means that the ground surface in that area is moving away from the satellite. Although the mechanism driving this phenomenon is unclear, it is possible that it was caused by the compaction of the volcanic deposits which flew into this area after the eruption. Another possible mechanism is that the changes in the terrain surface elevation of Sakurajima Volcano were induced by the changes in pressure of a magma reservoir and/or by erosion brought about by rain (Tomiyama et al., 2011).

For a more detailed investigation of the time transition of the LOS displacements, some points are taken as sample points. The sample points are divided into eight groups based on their elevation. Group "a" is for the points located at an elevation of 1050 m. Groups "b-g" are for the points located at elevations of 900 m to 150 m with an elevation interval of 150 m between the groups. Group "h" is for the points located at an elevation of 20 m. The locations of the sample points are shown in Figure 4.1.
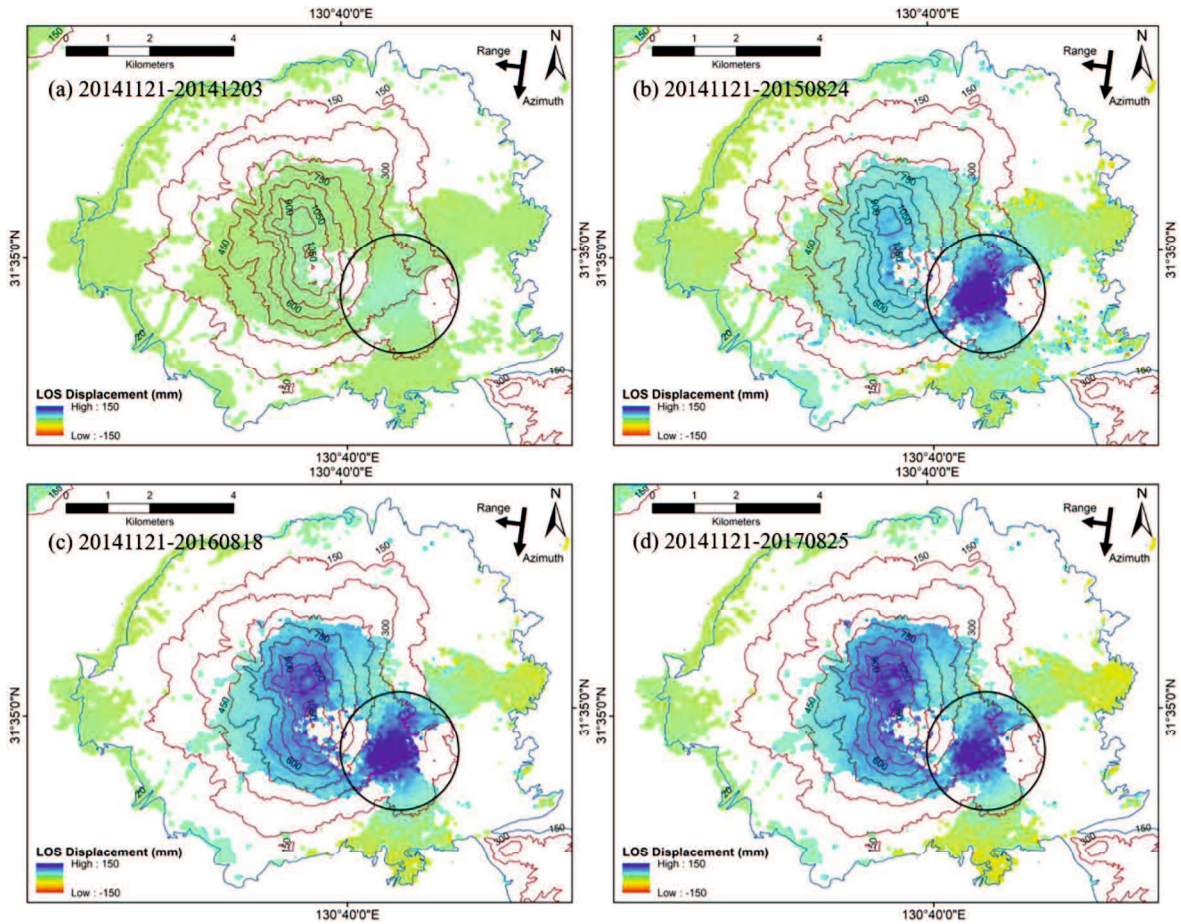
Figure 4.2 (a)-(d). Line of sight (LOS) displacement maps.

Figures 4.3 (a)-(h) shows the transition of the LOS displacements at all the sample points. The seasonal periodic behavior is clearly shown in groups "a-e". The behavior seems to have been caused by the tropospheric delay effects. Such a tendency at high elevations is larger than that at low elevations. This phenomenon is similar to the tropospheric delay effects found in GPS monitoring results (Shimizu et al., 2014; Nakashima et al., 2014).

On the other hand, it is also found that the LOS displacements tend to increase at certain elevations. The periodic behavior was also observed at an elevation of 300 m (group f), but some points show large changes in LOS displacements during the period from July to early September 2015. Those points are f19, f20, f22, and f23. At points g21, g22, and g 24, similar behavior to point f19 is seen, namely, that almost no displacement was observed from Dec 2014 to July 2015. However, the LOS displacements rapidly increased from July 2015 to September 2015 and gradually decreased until the last observation date. At the elevation of 20 m (group h), no periodic behavior is seen at any of the points of the LOS displacements. This is because the elevation of

the reference points, i.e., GCPs, is almost the same as 20 m. Thus, there are no tropospheric delay effects between the points in group h and the reference points of GCPs.
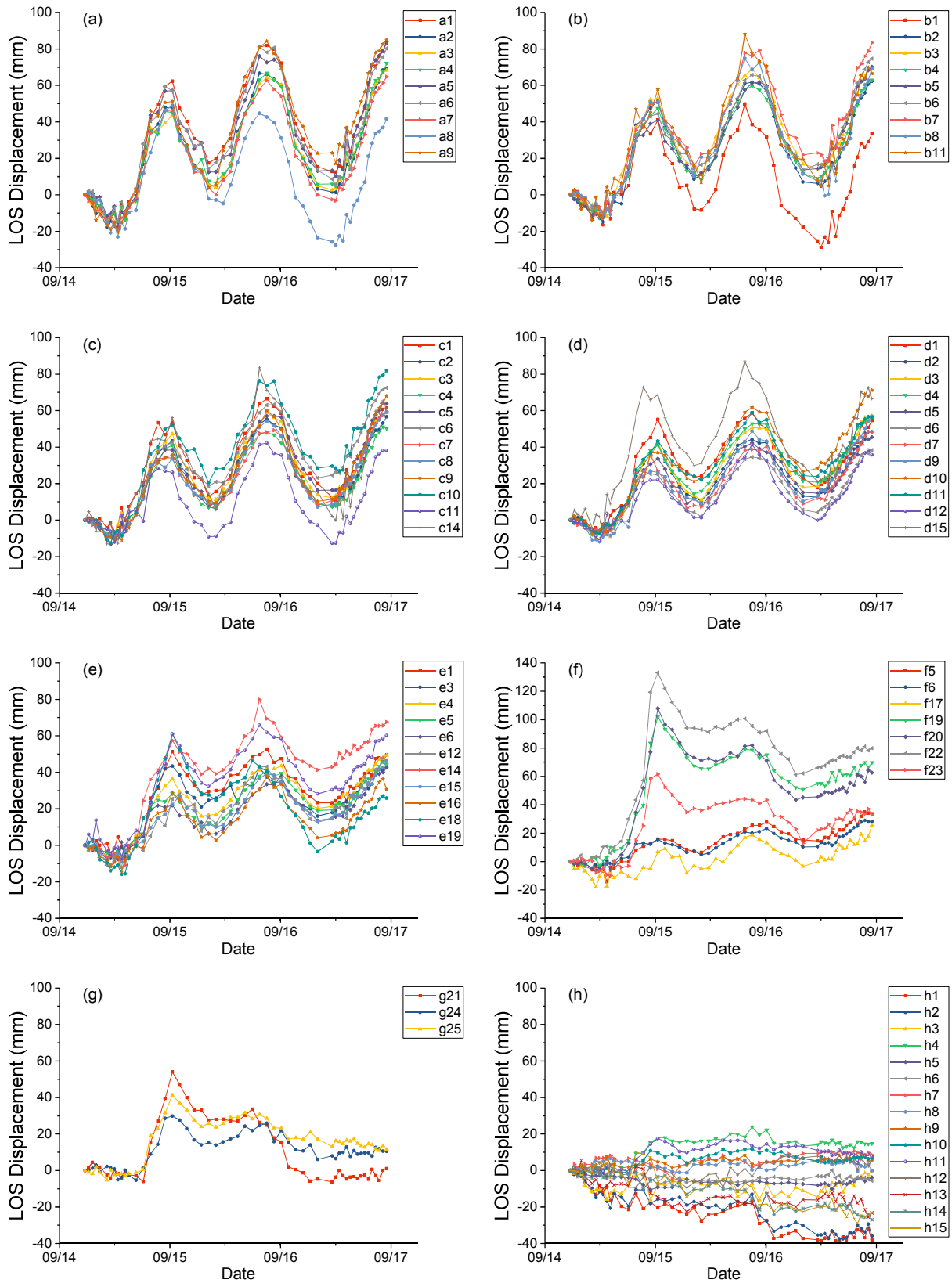
Figure 4.3 (a)-(h) Transition of LOS displacement at sample points.

4.4.2 Application of proposed methods to SBAS results

As shown in Figure 4.3 and mentioned in section 4.4.1, the SBAS results seem to be affected by tropospheric delays. In order to reduce the errors due to the tropospheric delays, the proposed method 1 and method 2 are applied to those results.

Step 1 of method 1, described in 4.3 *a.*, is now conducted. For the elevation of 1050 m, points a1-a6 have similar behavior. Therefore, the average is taken as *CVM1*. For the elevations of 900 m, 750 m, 600 m, 450 m, 300 m, and 20 m, the *CVM1* are calculated by taking the displacement average of (b5 and b6), (c7, c8, and c9), (d5, d6, and d7), (e4, e5, and e6), (f5 and f6), and (h5, h6, h8, h9, h11, and h13), respectively. For the elevation of 150 m, correction method 1 cannot be applied because the number of points is limited.

Step 4 of method 2, described in 4.3 *b.*, is applied. The ZTDdiff of each elevation is calculated. The hourly ZTDdiff is generated. Figure 4.4 (a) shows the ZTDdiff and CVM1 at the elevation of 1050 m. The ZTDdiff values at the SAR data acquisition time are selected. Figure 4.4 (b) shows the normalized ZTDdiff and the normalized CVM1. It seems that ZTDdiff and CVM1 have a good correlation.

(a)   (b)
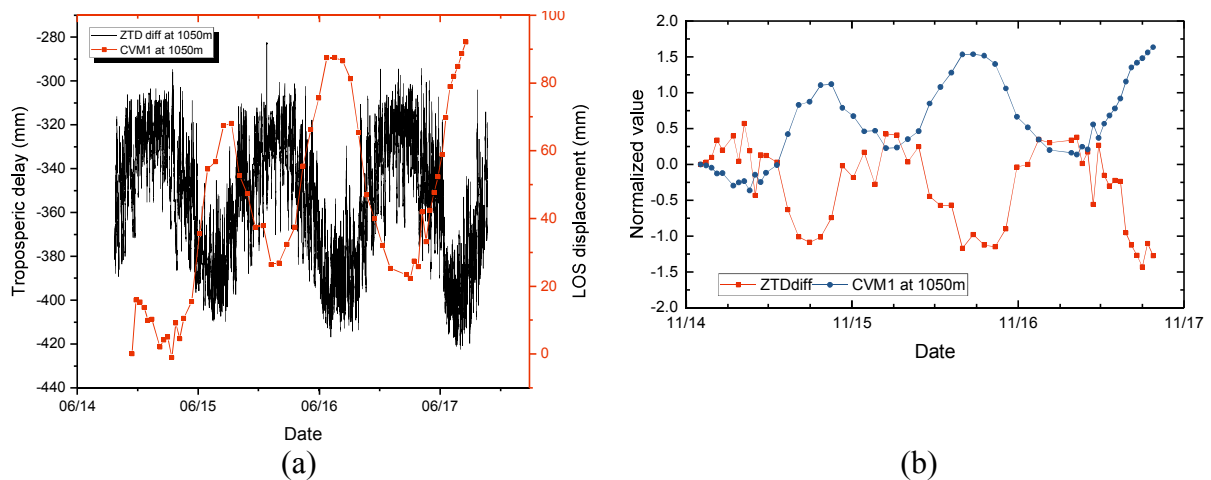
Figure 4.4 (a) Zenith tropospheric delay difference (ZTDdiff) and correction value of method 1 (CVM1) at elevation of 1050 m, and **(b)** normalized ZTDdiff and CVM1 at elevation of 1050 m.

Figure 4.5 (a) shows the ZTDdiff for each elevation. It is found that the ZTDdiff changes as a function of the elevation. Applying Step 5 of the procedure for method 2, Figure 4.5 (b) shows the linear regression of ZTDdiff and CVM1 at the points at the elevation of 1050 m. The results obtained by doing the same procedure for each elevation, from 450 m to 900 m, are summarized in Table 4.1.

Table 4.1 Linear regression equations and correlation values between ZTDdiff and CVM1 for each.

Elevation (m)	Linear regression equation	Correlation value (r)
1050	$CVM1_a = -0.8292 \cdot ZTDdiff_a - 252.76$	0.8644
900	$CVM1_b = -0.814 \cdot ZTDdiff_b - 209.08$	0.8289
750	$CVM1_c = -0.8521 \cdot ZTDdiff_c - 183.32$	0.8358
600	$CVM1_d = -0.7686 \cdot ZTDdiff_d - 128.87$	0.8093
450	$CVM1_e = -0.9421 \cdot ZTDdiff_e - 111.74$	0.7215

The average value for "a_H", as ($\bar{a}$), is calculated, and then $\bar{a} = -0.856$ is obtained. The linear regression of "b" with the elevation is derived, and then $b = -0.000243 \cdot H$ is obtained. Finally, the correction value by method 2 (*CVM2*) can be expressed by Eq. (4.8) as

$$CVM2_H = -0.856 \cdot ZTDdiff_H - 0.000243 \cdot H \tag{4.8}$$

where *H* is the elevation that represents the millimeter unit.
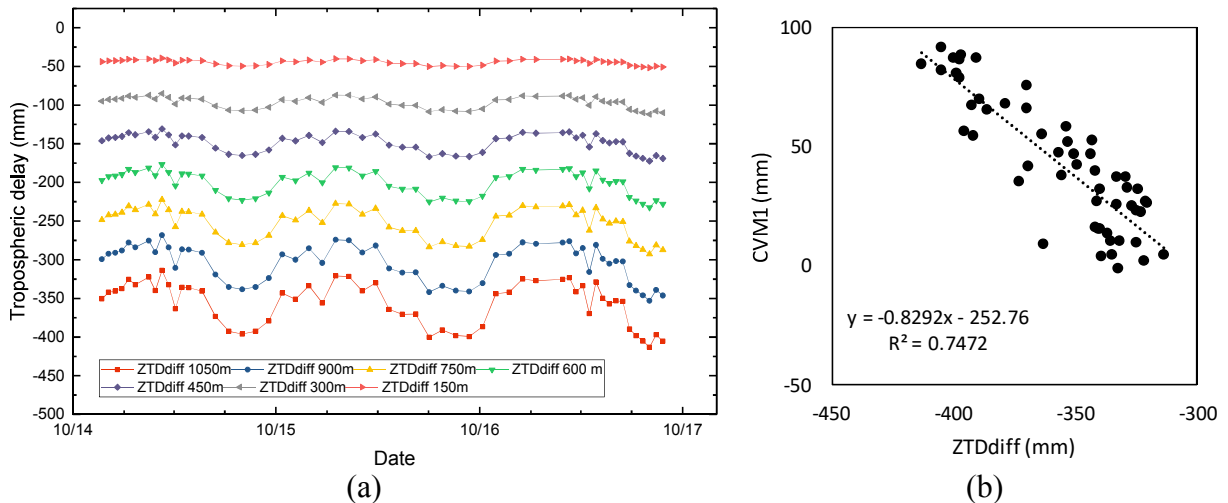
Figure 4.5 (a) ZTDdiff for each elevation and **(b)** correlation graph of ZTDdiff and CVM1 at elevation of 1050 m.

By applying both proposed methods, methods 1 and 2, the periodic behavior was removed, as shown in Figure 4.6. The LOS displacement transitions before and after the correction are shown in Figures 4.6 (a)-(d) for points a9, c1, f22, and h15, respectively. However, method 1 and method 2 yield different results, especially at high elevations. Method 1 seems to lead to smoother results than method 2. However, the results depend highly on the SBAS results. It is difficult to apply the method to the entire area when the results cannot be obtained due to low coherence. On the other hand, method 2 can overcome the demerit of method 1. It can be applied to the entire area once the correction value equation has been determined. Although further applications are

required to confirm the validity of the proposed methods, the first application introduced in this study can provide better results than those of the original SBAS.
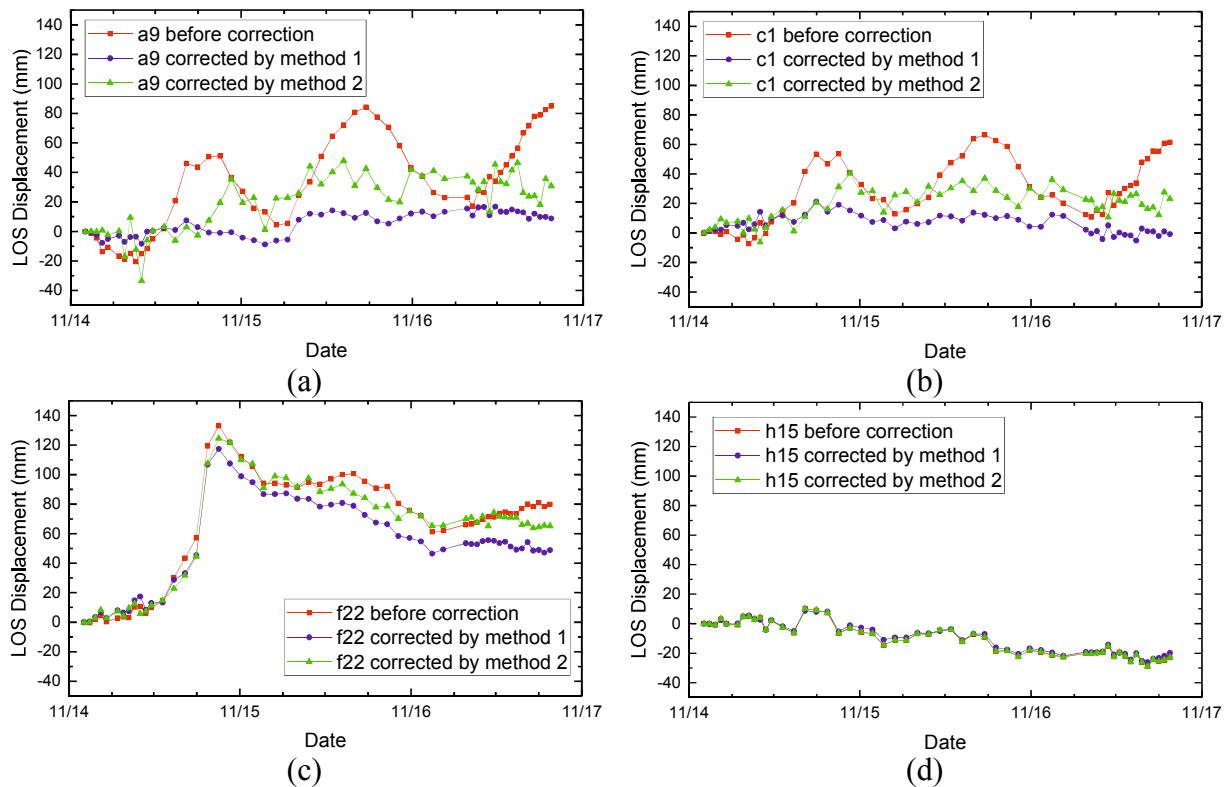
Figure 4.6 (a)-(d). Transition of LOS displacements at selected points before and after correction by two proposed methods.

4.5 Summary of chapter 4

Monitoring the behavior of volcanoes is very important. This task can be done by employing the DInSAR method and conducting a time-series analysis using SBAS. It can provide the spatial distribution of the LOS displacements with cm-order accuracy. However, the periodic behavior caused by tropospheric delays severely affects the SBAS results. Tropospheric delays occur due to the high variation of the elevation found in areas with volcanoes. Two methods have been proposed in this study to reduce these effects. Method 1 is an empirical method, while method 2 is a semi-empirical method using a physical model called the Hopfield model. By taking the study case of Sakurajima Volcano, Japan, both methods were able to successfully reduce the periodic behavior. Further study is needed to investigate the validity of the proposed methods.

References

Berardino, P., Fornaro, G., Lanari, R. and Sansosti, E., 2002, A new algorithm for surface deformation monitoring based on small baseline differential SAR interferograms, *IEEE Trans. Geosci. Remote Sens*., 40, 2375–2383.

Ding, X.L., Li, Z.W., Zhu, J.J., Feng, G.C. and Long, J.P., 2008, Atmospheric effects on InSAR measurements and their mitigation, *Sensors.,* 8, 5426–5448.

Doin, M.P., Lasserre, C., Peltzer, G., Cavalié, O. and Doubre, C., 2009, Corrections of stratified tropospheric delays in SAR interferometry: Validation with global atmospheric models, *J. Appl. Geophys*., 69, 35–50.

Hanssen, R.F., 2001, Radar Interferometry: Data Interpretation and Error Analysis. Kluwer Academic Publishers, Dordrecht.

Hoffman-Wellenhof, B., Lichtenegger, H. and Collins, J., 1992, GPS: Theory and practice, Second Edition. Springer, New York.

Japan Meteorological Agency, 2015, Sakurajima volcanic activity in 2015. (In Japanese)

Jolivet, R., Grandin, R., Lasserre, C., Doin, M.P. and Peltzer, G., 2011, Systematic InSAR tropospheric phase delay corrections from global meteorological reanalysis data, *Geophys. Res. Lett.*, 38, 1–6.

Massonnet, D. and Feigl, K.L., 1998, Radar interferometry and its application to changes in the earth's surface. Rev, *Geophys*, 36, 441–500.

Nakashima, S., Namba, T., Itagaki, S., Soda, H., Iwasaki, T., Shimizu, N. and Ono, M., 2014, Tropospheric delay correction of GPS displacement measurement in the presence of large height differences using fixed-point observation, *Journal of MMIJ.,* 130, 479-487. (In Japanese)

Shimada, M., 1999, Correction of the satellite's state vector and the atmospheric excess path delay in the SAR interferometry - An application to surface deformation detection, *J. Geod. Soc. Japan*, 45, 327–346.

Shimizu, N., Nakashima, S. and Masunari, T., 2014, ISRM suggested method for monitoring rock displacements using the Global Positioning System (GPS), *Rock Mech Rock Eng.,* 47, 313-328.

Tomiyama, N., Koike, K., Iguchi, M. and Omura M., 2011, Analysis of topographic change at Mount Sakurajima, South Kyushu, Japan, using JERS-1 SAR Interferometry, *Geoinformatics,* 22, 17-24

Chapter 5

Application of DInSAR to geotechnical issues: case studies

In chapter 3, the success of the application of SBAS DInSAR for long-term subsidence monitoring in Semarang was shown. In chapter 4, it was seen that SBAS DInSAR with correction by means of the proposed method could yield reasonable results for ground surface displacement over the rugged topography of Sakurajima Volcano. In those chapters, it was proven that SBAS DInSAR can be a useful tool for ground surface displacement monitoring in such vast areas. It is important to apply the same technique to other areas which have potential geotechnical issues.

In this chapter, six different areas have been taken as case studies, namely, Seoul and its surrounding area in South Korea, Denpasar and its surrounding area in Indonesia, Mitake and its surrounding area in Japan, Sidoarjo mud flow area in Indonesia, Black Sea coast in Bulgaria, and Yabakei slope in Japan. The geotechnical issues of these areas can be categorized into two different types, land subsidence and land mass movement.

5.1 Subsidence monitoring in various cities

5.1.1 Subsidence in Seoul megapolitan city, South Korea

a. Study area

The study area is the city of Seoul and its surrounding area in South Korea. With a population of about 10 million people, Seoul is the largest city in South Korea (World Population, 2018). With the surrounding Incheon metropolis and Gyeonggi Province, the Seoul megapolitan area forms the heart of the Seoul Capital Area, home to roughly half of the country's population. Rapid growth of the South Korean economy has led to the development of a massive infrastructure across the country, including Seoul.

The rapid development of a city is usually followed by environmental issues along with social issues. The environmental issues related to geotechnical challenges include, for example, the subsidence that has occurred in some big cities of the world, such as Tokyo, Mexico City, Jakarta, and many others. Therefore, it would be interesting to know whether Seoul will also face these same types of environmental issues. Thus, this study applies the SBAS DInSAR in order to answer this question. Figure 5.1 shows the location of the study area.
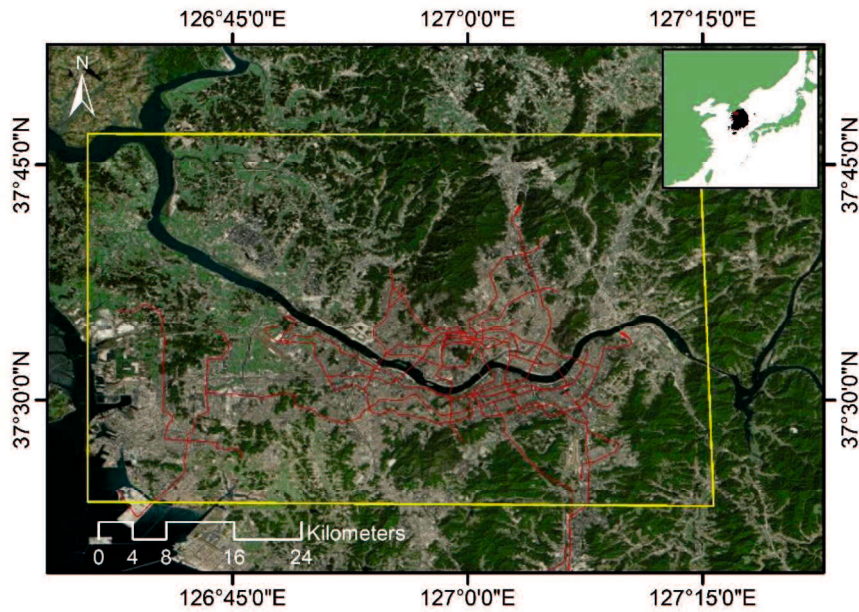
Figure 5.1 Google Earth images of part of Korean Peninsula. The yellow box shows the study area (Seoul and its surrounding area).

b. Data collection and processing

Twenty-nine images of Sentinel-1 SAR were used to conduct a time-series analysis by SBAS DInSAR. The first SAR image was recorded on 26 October 2014 and the last image was recorded on 19 May 2017. All the SAR data were provided by ESA at no cost. The ALOS Global Digital Elevation Model (ALOS-GDEM), which was provided by JAXA, was used to remove the topographic component. The setting and the conditions of the parameters for the SBAS DInSAR analyses are presented in appendix 3. Ninety-one interferograms were used. The baseline table of this SBAS is shown in Figure 5.2.
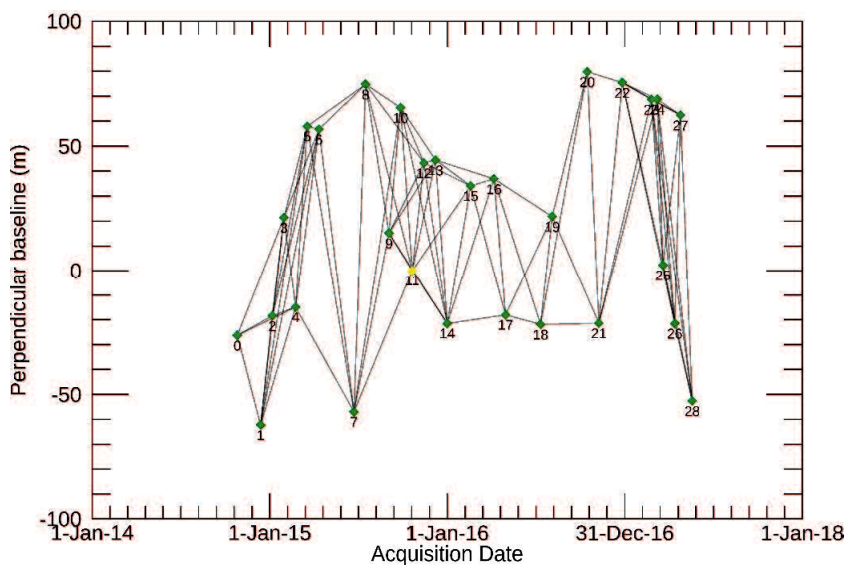
Figure 5.2 Baseline table of SBAS DInSAR processing for Seoul.

c. Results and discussion

Figure 5.3 shows the subsidence map of Seoul and its surrounding area as a result of SBAS DInSAR. The total subsidence occurring during the period of October 2014 to May 2017 can be seen in the figure. It can also be seen that the subsidence varies from place to place. The blue color means no subsidence, while the red color means the largest subsidence of up to 200 mm. There are eight interesting regions that present the occurrence of remarkable subsidence. Those regions are marked by boxes in Figure 5.3 and named Areas of Interest (AOI) from A to H.
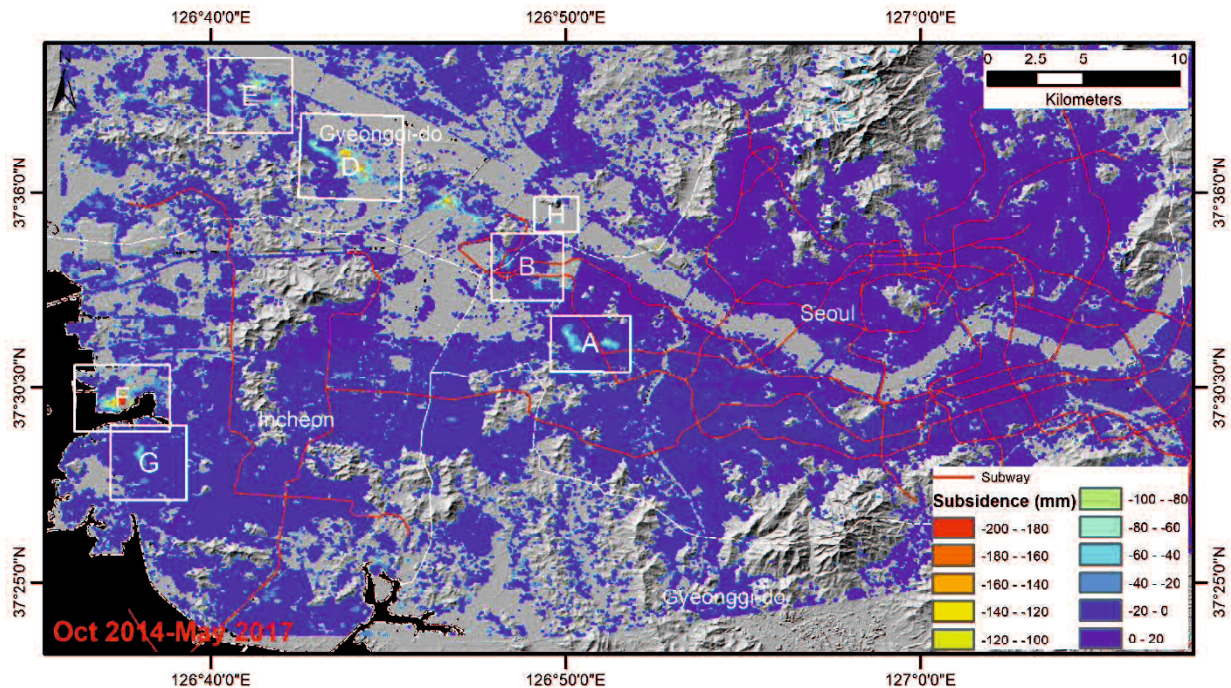
Figure 5.3 Subsidence map of Seoul and its surrounding area derived from Sentinel-1 SAR data from October 2014 to May 2017.

Figures 5.4 to 5.7 show the subsidence distribution, the optical image, and the subsidence transition at particular points in AOI A-H consecutively. Areas A, B, C, D, E, and H are a mix of residential and business/commercial areas. A typical subsidence pattern like a bowl is found. This subsidence could have been caused by excessive groundwater withdrawal. However, this hypothesis should be proven by further investigation, as there is presently no solid proof of it. AOI-F seems to be a reclaimed area since it is used as a port. In this area, the land settlement could have been caused by natural consolidation. In AOI-H, the displacement of a bridge was found.

Through these results, it is shown that the merit of SBAS DInSAR is its ability to provide displacement information over a vast area. The results can then be used as base data for

considering areas that might need more attention or further investigation. Additionally, it is also found that SBAS DInSAR has the potential to monitor bridge displacement behavior. This means that SBAS DInSAR also has the potential to monitor other man-made objects.
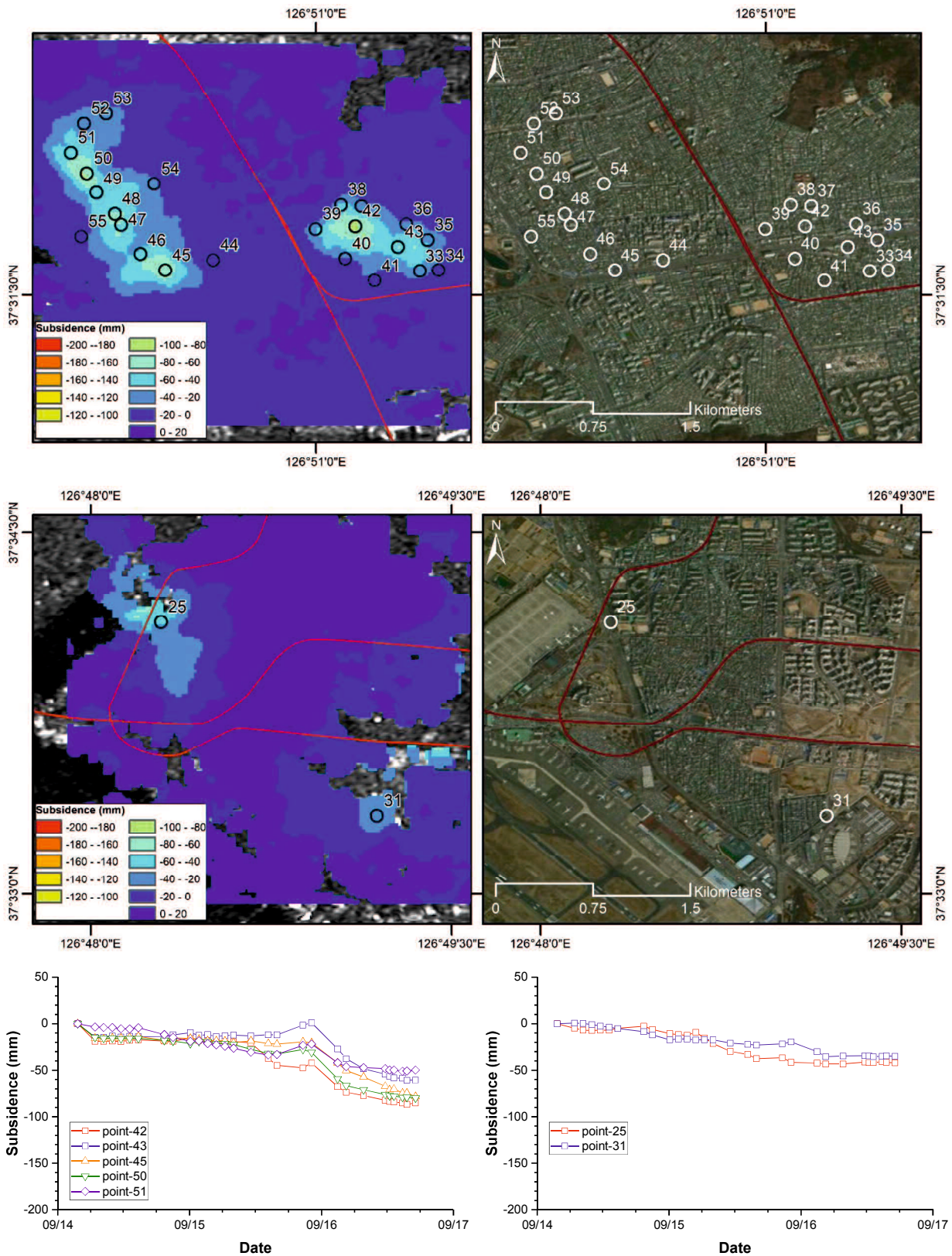
Figure 5.4 Subsidence map and subsidence transition at AOI-A and AOI-B.
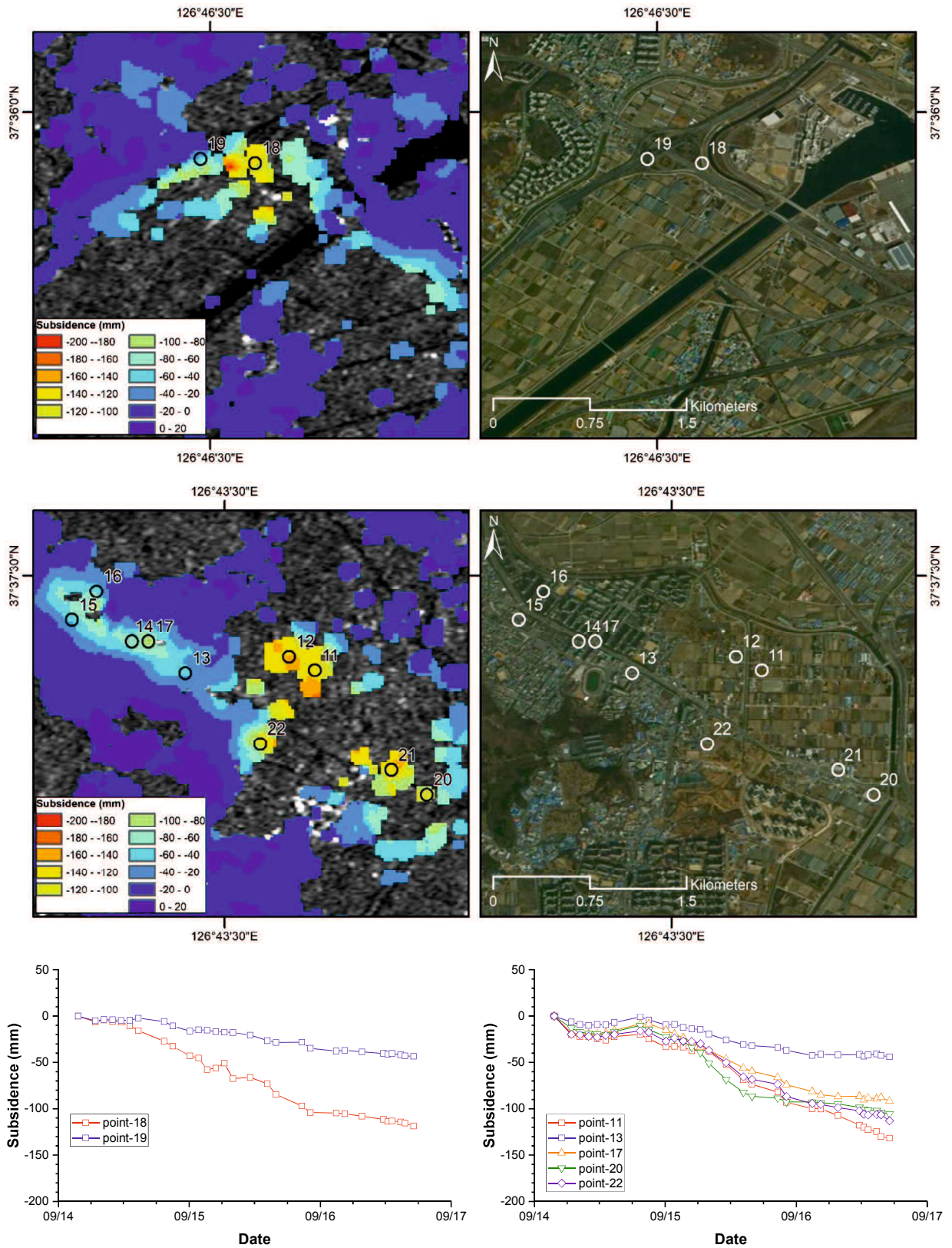
Figure 5.5 Subsidence map and subsidence transition at AOI-C and AOI-D.
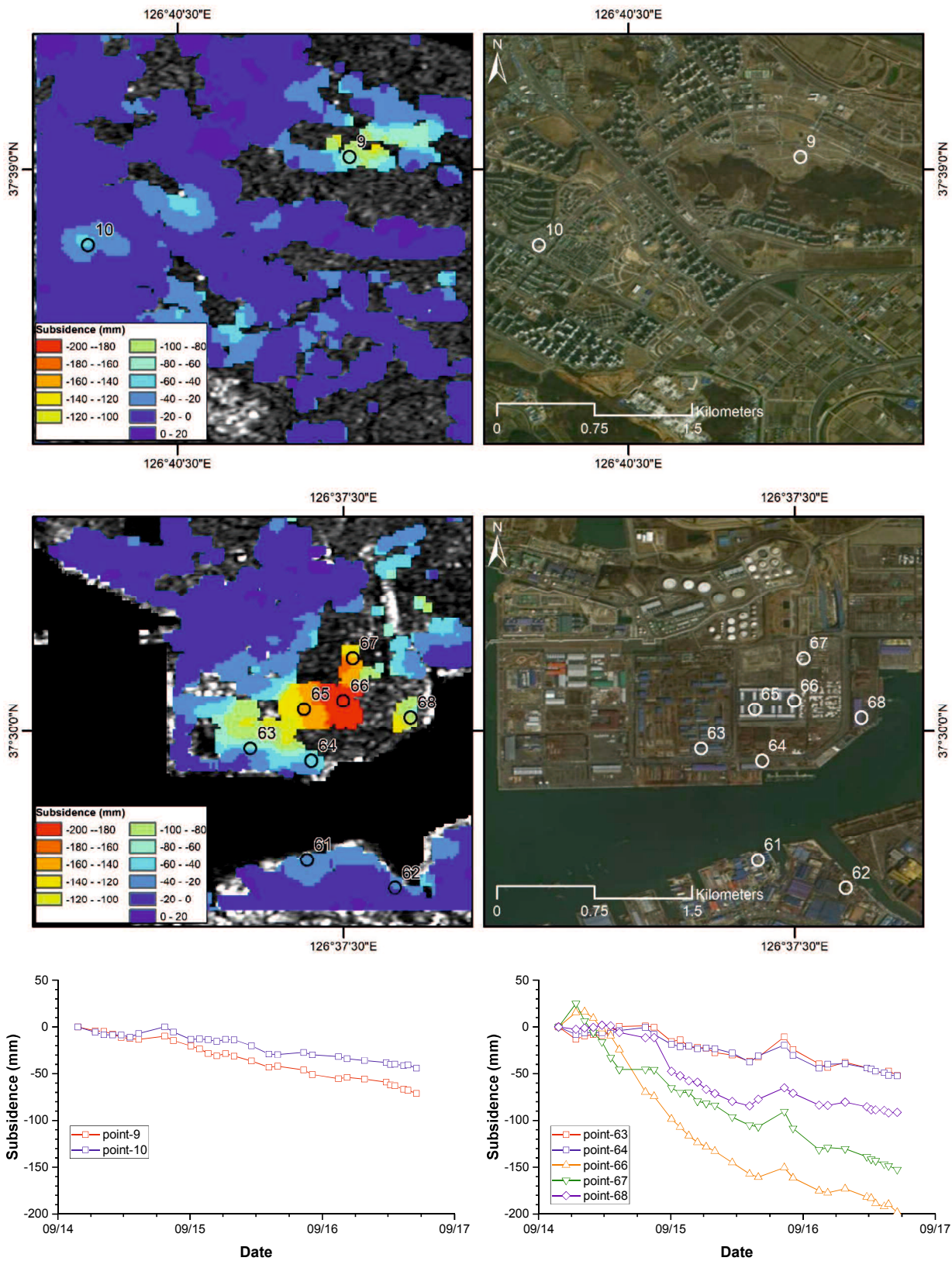
Figure 5.6 Subsidence map and subsidence transition at AOI-E and AOI-F.
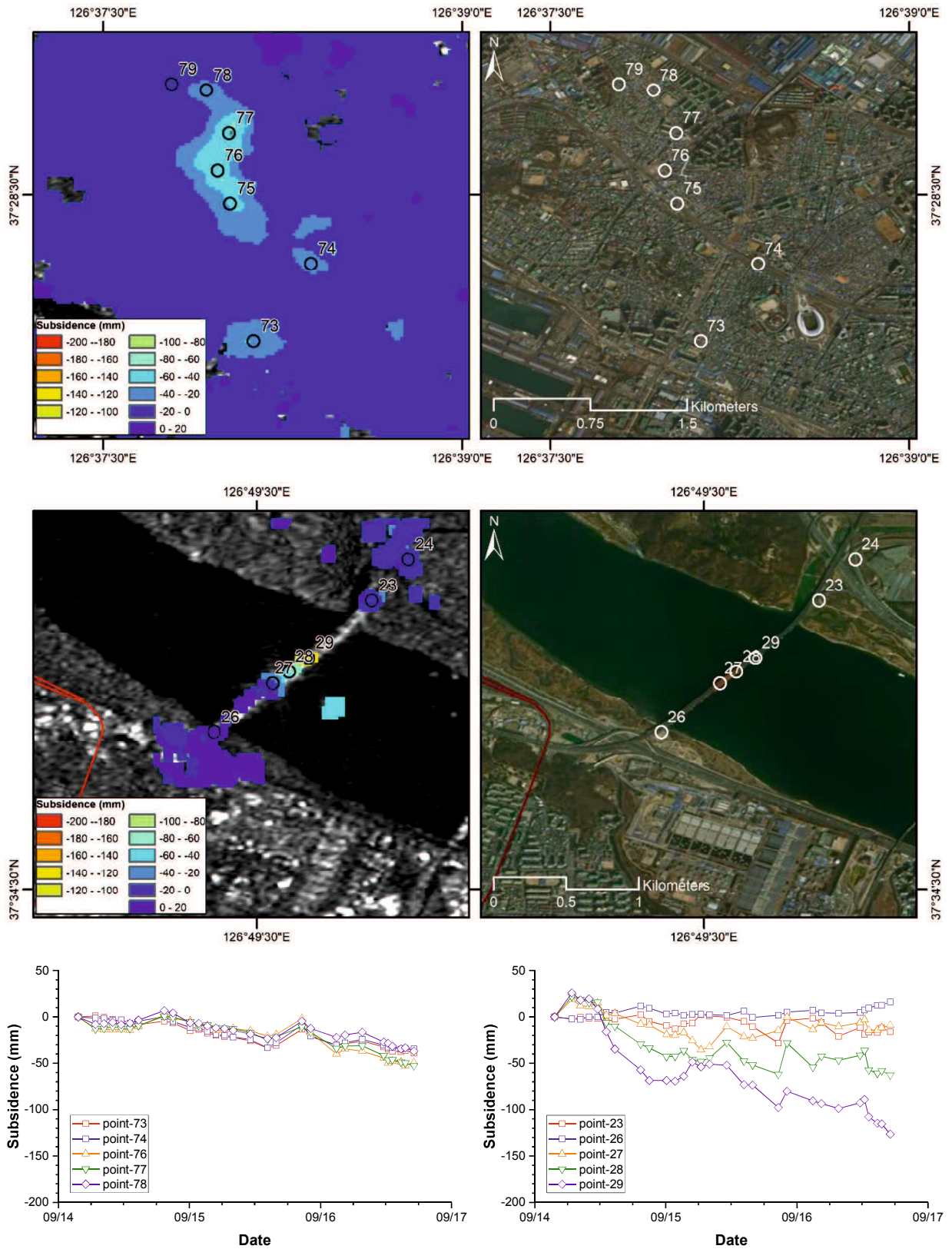
Figure 5.7 Subsidence map and subsidence transition at AOI-G and AOI-H.

5.1.2 Subsidence in Denpasar and its surrounding area, Bali, Indonesia

a. Study area

Bali is an island and a province in Indonesia. Bali is famous around the world for its beauty and tourist attractions. It has been the main tourist destination in Indonesia for many years. These tourist activities benefit the Balinese economy. However, the development is concentrated mostly in South Bali, including the city of Denpasar. The population is also concentrated in that area. In 2016, it was inhabited by 1 million people (BPS, 2016).

Although there have been no reports of subsidence or land surface movements in the area, it is important to conduct a SBAS DInSAR analysis to know the actual land behavior there. Figure 5.8 shows the location of the study area.
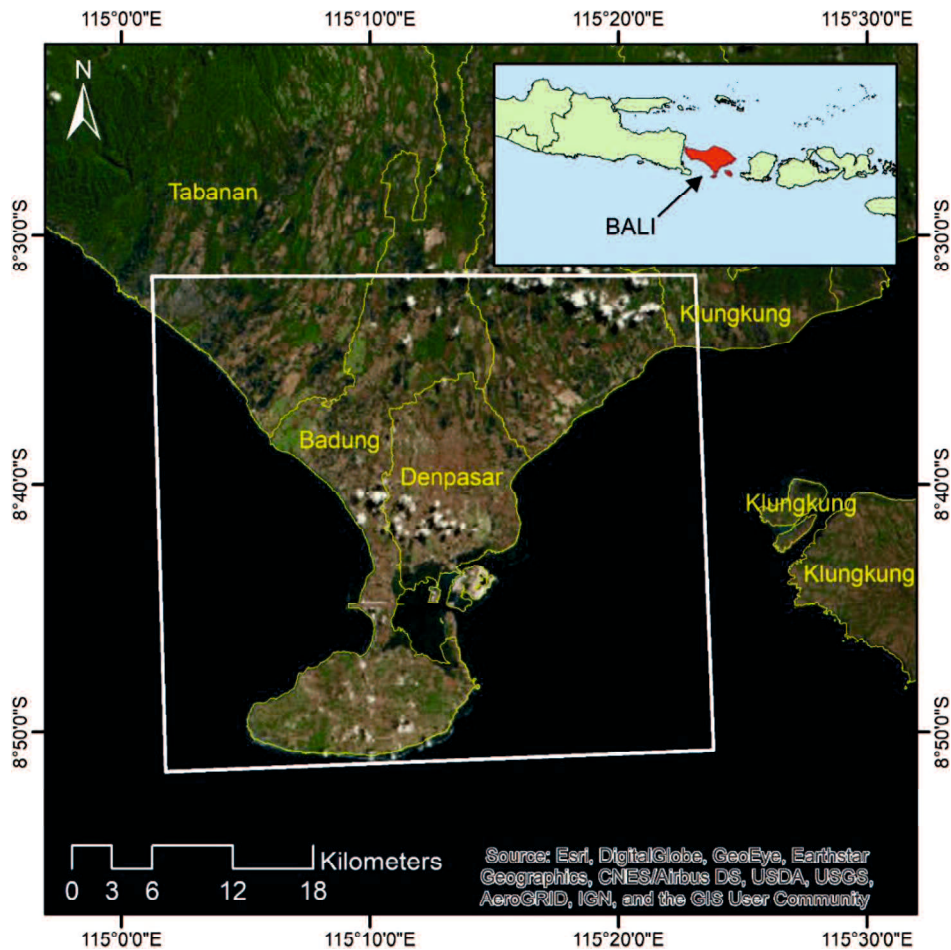
Figure 5.8 South Bali area including Badung Regency and city of Denpasar. The analyzed area is in the white box on the map.

b. Data collection and processing

To detect surface movement, SAR data by Sentinel-1 in the ascending direction were used. Thirty-five images of SAR data from October 2014 to August 2017 were collected. The SBAS

70

DInSAR setting for this study can be found in appendix 3. Figure 5.9 shows the baseline table of the SBAS DInSAR of this study. To remove the topographic component, the ALOS-GDEM by JAXA was used.
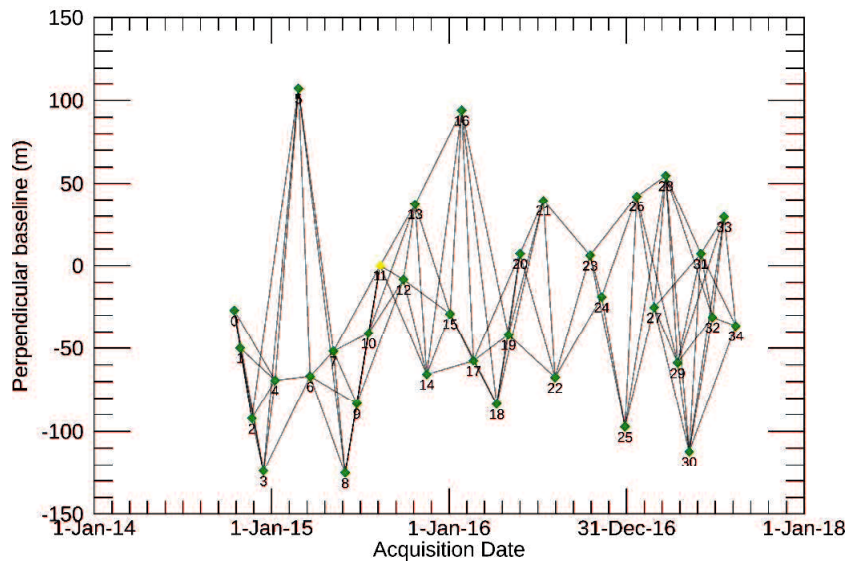
Figure 5.9 Baseline table of SBAS DInSAR for Denpasar and its surrounding area.

c. Results and discussion

Figure 5.10 shows the time-series LOS displacement map of Denpasar and its surrounding area from October 2014 to August 2017. The satellite observation was conducted in the descending right-looking direction, which means negative LOS displacement, indicating the ground surface moving away from the satellite and vice versa. The ground surface was seen to move away up to 80 mm in the south-west areas of Denpasar (yellow-red color on the map) during the observation period. It is clearly seen that the LOS displacement became larger over time in those areas. The blue colored area is the area without remarkable displacement. There are no results in the white colored area due to low SAR data coherence.

To grasp the transition behavior of the LOS displacement, six points of interest have been set, namely, B1, B8, B9, B11, B13, and B15. All point locations and their corresponding displacement transitions can be found in Figure 5.11. The largest displacements are found at points B1 and B9. The LOS displacement at those two points is seen to reach up to 60 mm. However, the behavior is different among them. At B1, the displacement increases monotonically. At point B9, on the other hand, the displacement seems to be smaller. At the other remaining points, the total displacement does not exceed 40 mm during the 3-year observation period. Based on the

71

experience of subsidence monitoring in Semarang, displacement that is less than 1 cm/year can be considered as not remarkable.

From these results, it is found that the LOS displacement in Denpasar is still not remarkable. These results coincide with the fact that no reports have ever been published regarding subsidence in this area. However, some areas do need more attention since their displacement behavior seems to be increasing. These SBAS DInSAR results can be a kind of warning or forecast to stakeholders in Bali to prevent serious subsidence from occurring. The continuation of this monitoring and further study of this phenomenon are highly recommended. This can be an issue for future research.
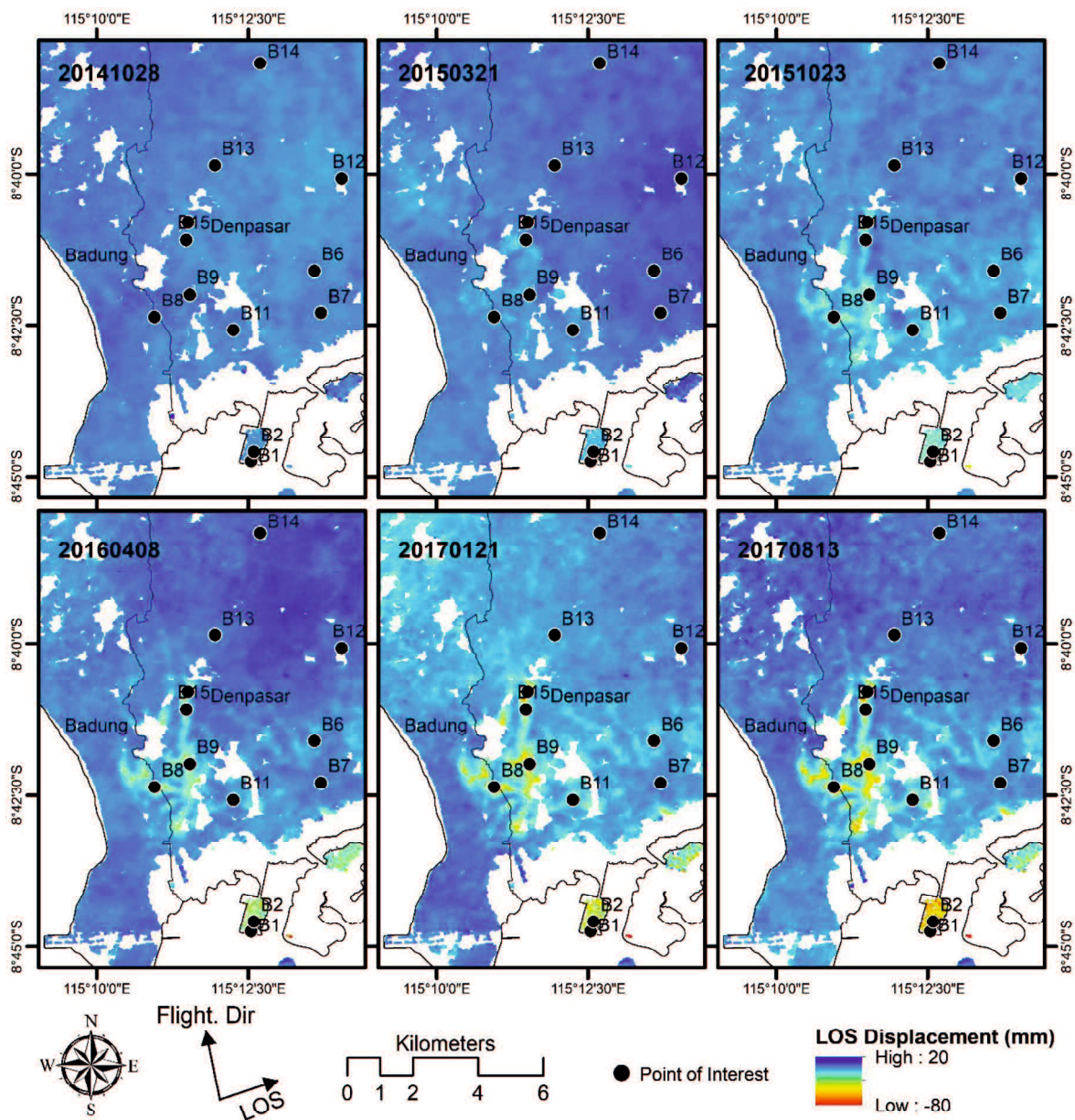
Figure 5.10 Time-series LOS displacement map in Denpasar and its surrounding area from October 2014 to August 2017.
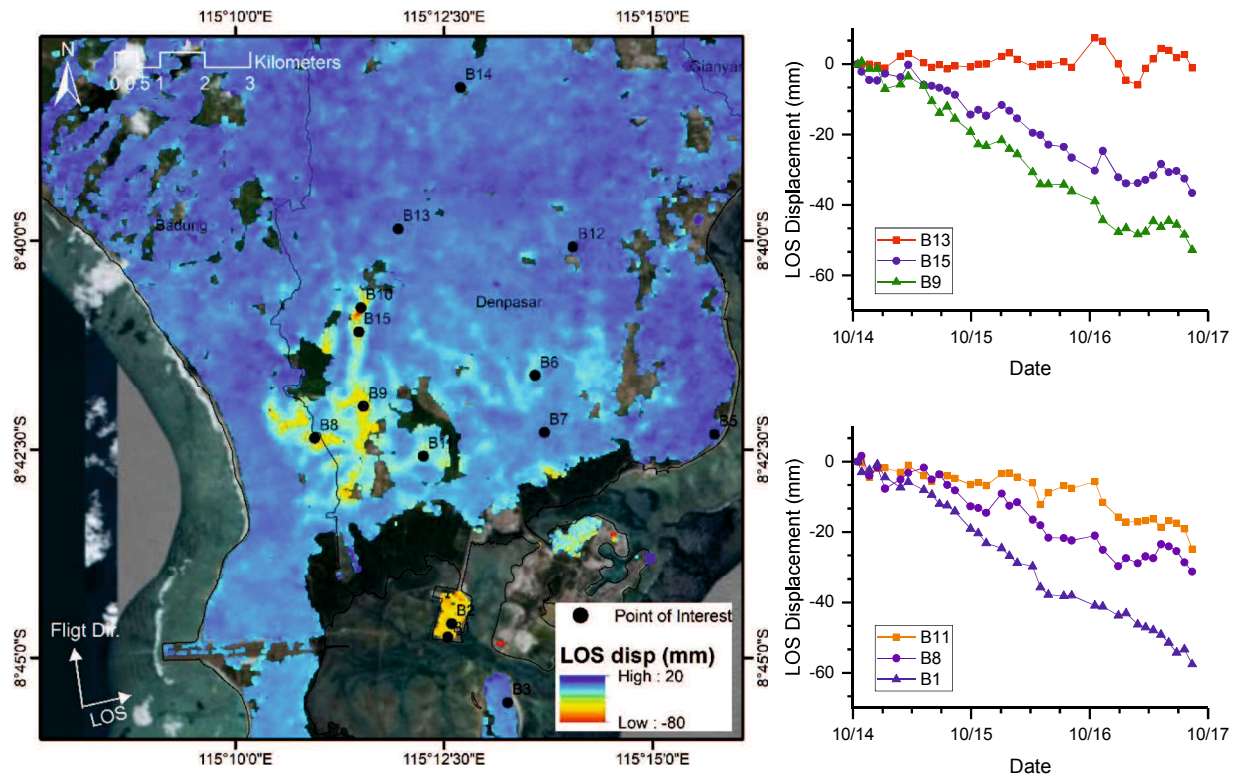
Figure 5.11 Transition of LOS displacement at six points of interest.

5.1.3 Subsidence induced by underground mining activity, Mitake, Japan

a. Study area

Figure 5.12 Location of the Mitake on an open street map. The study area is located in the black box.

Mitake is located in Gifu Prefecture, Japan. Its location is shown in Figure 5.12. Mitake was famous for its underground mining activities until the mid-1900s when the activities were stopped and the mines were abandoned. Many sinkholes and subsidence areas have been reported in this area (Aydan and Ito, 2015). The sinkholes and subsidence were probably triggered by the collapse of pillars which once served as supports at the abandoned underground mine sites.

Although these sinkholes and subsidence are spread over a large area, the size of the sinkholes and subsidence are not large in terms of monitoring by remote sensing. This is a new challenge for SBAS DInSAR, namely, to confirm whether it is capable of detecting small displacement behavior in such local areas. It will be an important finding if SBAS DInSAR can be utilized to predict collapse areas before they actually collapse. Therefore, Mitake is a good place to conduct such a study.

b. Data collection and processing

There are 70 images of Sentinel-1A/B SAR data available in our inventory. The acquisition dates of the data span from 5 May 2015 to 12 June 2018. The observations were acquired during the ascending passage and in a right-looking direction (ARL). Based on the setting of the SBAS parameters, 512 interferograms were generated, but 1 SAR data was discarded, and accordingly, 10 corresponding interferograms were not used for any further analysis. The details for the setting of the SBAS parameters can be found in appendix 3. Figure 5.13 shows the baseline table of the SBAS DInSAR for Mitake.
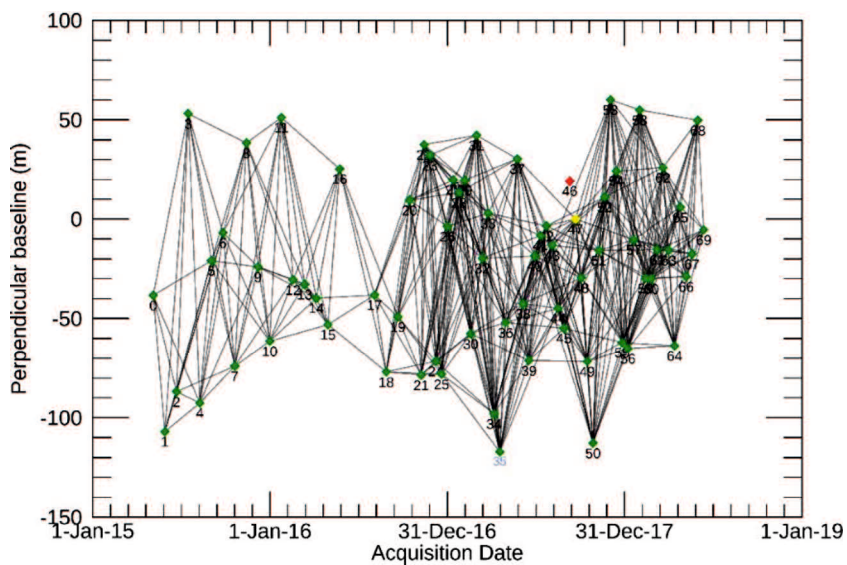
Figure 5.13 Baseline table of SBAS DInSAR for Mitake.

c. Results and discussion
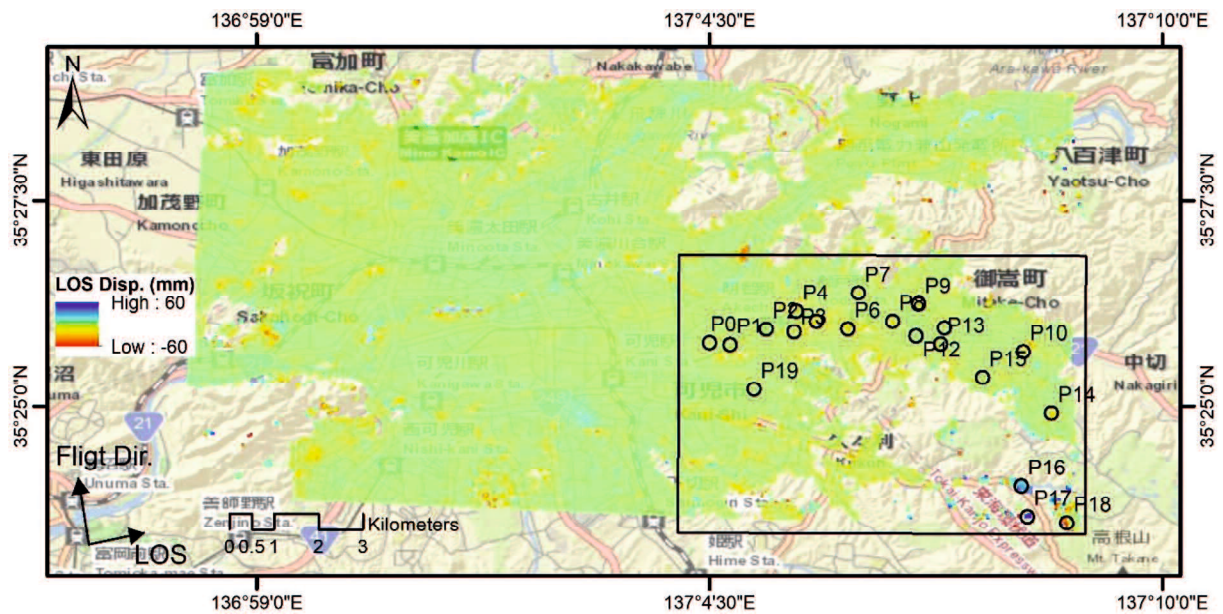
Figure 5.14 Total LOS displacement from May 2015 to June 2018. The analysis is focused on the black box area, namely, 19 points of interest have been set.

Figure 5.14 shows the total LOS displacement during the observation period. The LOS displacement varies from around +30 mm to -60 mm. The positive LOS displacement means the ground surface moves toward the satellite and vice versa. The processed SAR data cover the nearby area; however, further analysis will be focused on the area inside the black rectangle. The time-series LOS displacement in the area of interest is presented in Figure 5.15.

Figure 5.15 shows the spatial distribution of the LOS displacement over time. It can be seen that, in some areas, the amount of LOS displacement has been increasing since the beginning of the observation period. Due to a lack of information on the exact positions of the sinkholes and subsidence areas, the points of interest were selected arbitrarily. Nineteen points have been set and their LOS displacement was extracted from the map.

The transition of LOS displacement at the points of interest are shown in Figure 5.16. The measurements results for all points, except P16, P17, and P18, are scattered from +5 mm to -20 mm. The LOS displacements are too small to measure. Further study is needed in order to know the validity of the SBAS results by comparing them with other measurement results on the ground. In particular, the behavior at point P14 has a different pattern from the others. A deeper investigation should be conducted for this point.
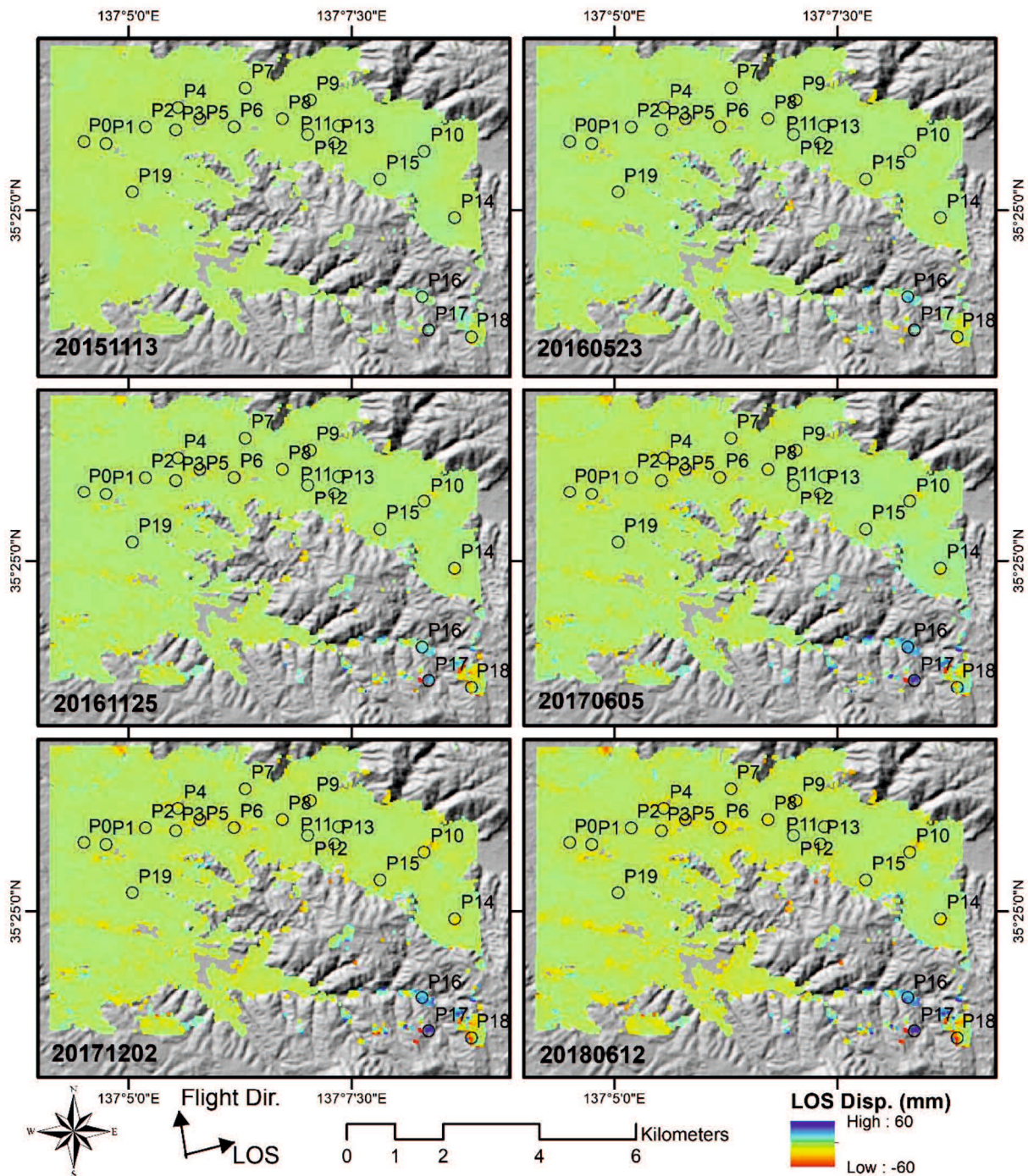
Figure 5.15 Time-series LOS displacement map of Mitake during the period May 2015 to June 2018.

From these results, it is found that it is still difficult to detect sinkholes and local subsidence by means of SBAS-DInSAR and using Sentinel-1 SAR data since the target areas are too small. However, SBAS DInSAR provides maps of the areas with no remarkable displacement (light green color). It is necessary to compare those maps with the actual locations of sinkholes and the local subsidence map. This will be another issue for a future research.
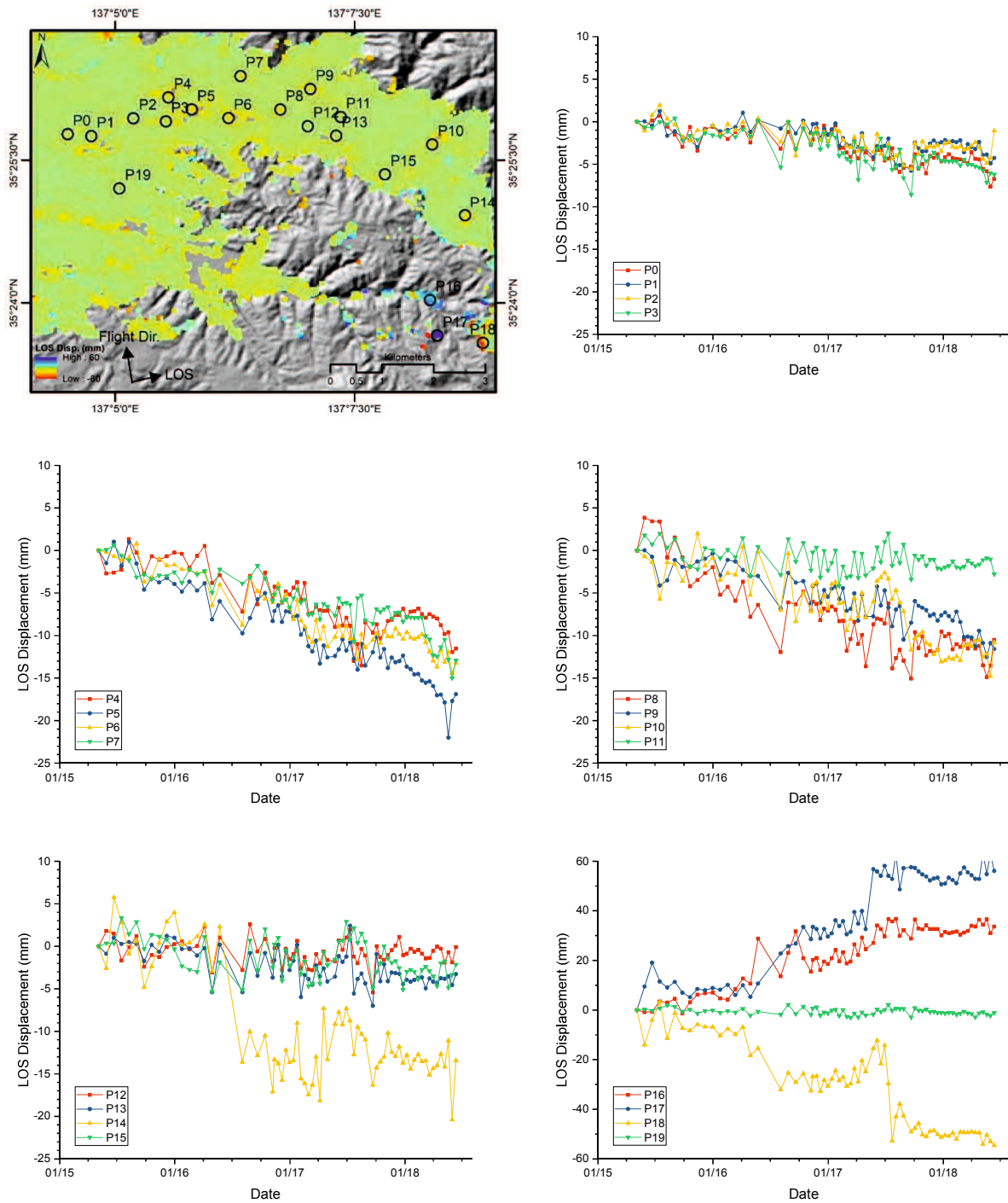
Figure 5.16 LOS displacement transition at several points of interest.

5.2 Monitoring of ground displacement induced by mass movements and landslides

5.2.1 Ground deformation induced by Sidoarjo mudflow (Lusi), Indonesia

a. Study area

The Sidoarjo mud flow or, in the Indonesian language, *Lumpur Sidoarjo (Lusi)*, is the result of an erupting mud volcano. It began near Sidoarjo, East Java, on 29 May 2006. It has

discharged ~104–105 m³/day of mud ever since, and it is predicted that this discharge will last for more than 80 years (Rudolph et al., 2011). This is a huge disaster for the Indonesian people. At least 60,000 people should be displaced (Richards, 2011), but the cause of Lusi is still under debate. There are two different arguments among scientists about the factors that are triggering Lusi. One group says that the cause of this mud volcano is the drilling activity of one oil company, while other groups says that the cause is the occurrence of a distant earthquake (Manga et al., 2009; Sawolo et al., 2009). One researcher has published a discussion on the controversy surrounding the factors related to the triggering of Lusi (Davies, 2017). Figure 5.17 shows the location of Lusi. The study area is marked with a red box.
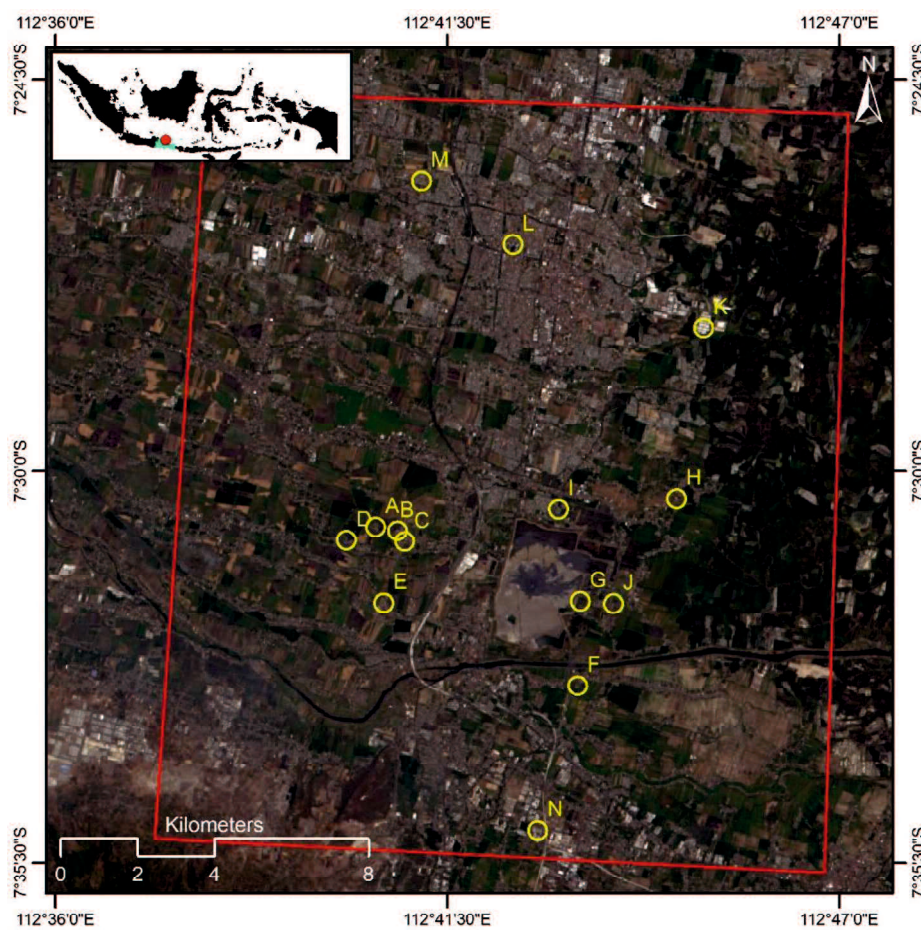
Figure 5.17 Location of Sidoarjo mudflow.

The Lusi mud flow is believed to be driving the land subsidence in the surrounding area (city of Sidoarjo). Research has been conducted to monitor the land subsidence in Lusi's surrounding area by Aoki and Sidiq (2014). They investigated the ground deformation using a total of 93 images of ALOS-PALSAR data that were taken from 2007-2011. They employed the PSI method using StaMPS software. It was found that the ground deformation was not limited to

the mud volcano, but that it was also occurring in nearby areas. They also found that the LOS displacement in certain areas was up to 300 mm during the observation period and that this rate was decreasing. In conclusion, they predicted that the Lusi mud flow would not last long. In this study, information on the LOS displacement in Lusi's surrounding area will be updated.

b. Data collection and processing

To conduct the time-series deformation monitoring, 42 images of Sentinel-1 SAR data are used. The SAR data were taken during the period of 10 Nov 2014 to 14 August 2017. The observation of the SAR data was taken in path number 3 during the descending passage and in a right-looking direction. The baseline table of the SBAS processing is shown in Figure 5.18. Details on the SBAS parameter setting are presented in appendix 3.
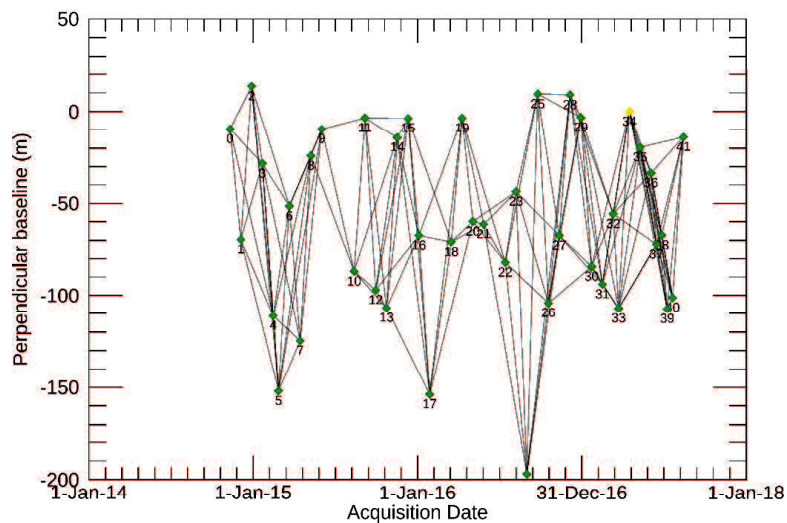
Figure 5.18 Baseline table of SBAS DInSAR for Lusi analyses.

c. Results and discussion

Figure 5.19 shows the time-series LOS displacement obtained from November 2014 to August 2017. No results were obtained at the mud deposit due to SAR's low coherence (<0.4). In some areas, LOS displacement up to -150 mm has been detected; it is marked by yellow to red colors. A clear deformation can be seen according to the time, as presented in Figure 5.19; however, the magnitude is smaller compared to period 2008-2011.

In order to understand the transition of the LOS displacement behavior, the values of some of the interest points were extracted. Their results are shown in Figure 5.20. The deformation at some points, such as points A, B, and C, tend to stabilize. However, linear behavior is found at some other points, such as points D, E, F, and G, although their magnitude is smaller. Using these

results, the subsidence map for the surrounding Sidoarjo mud flow is being updated. The recent displacement behavior has been shown. It is found that SBAS DInSAR is useful for providing recent ground displacement information over large areas.
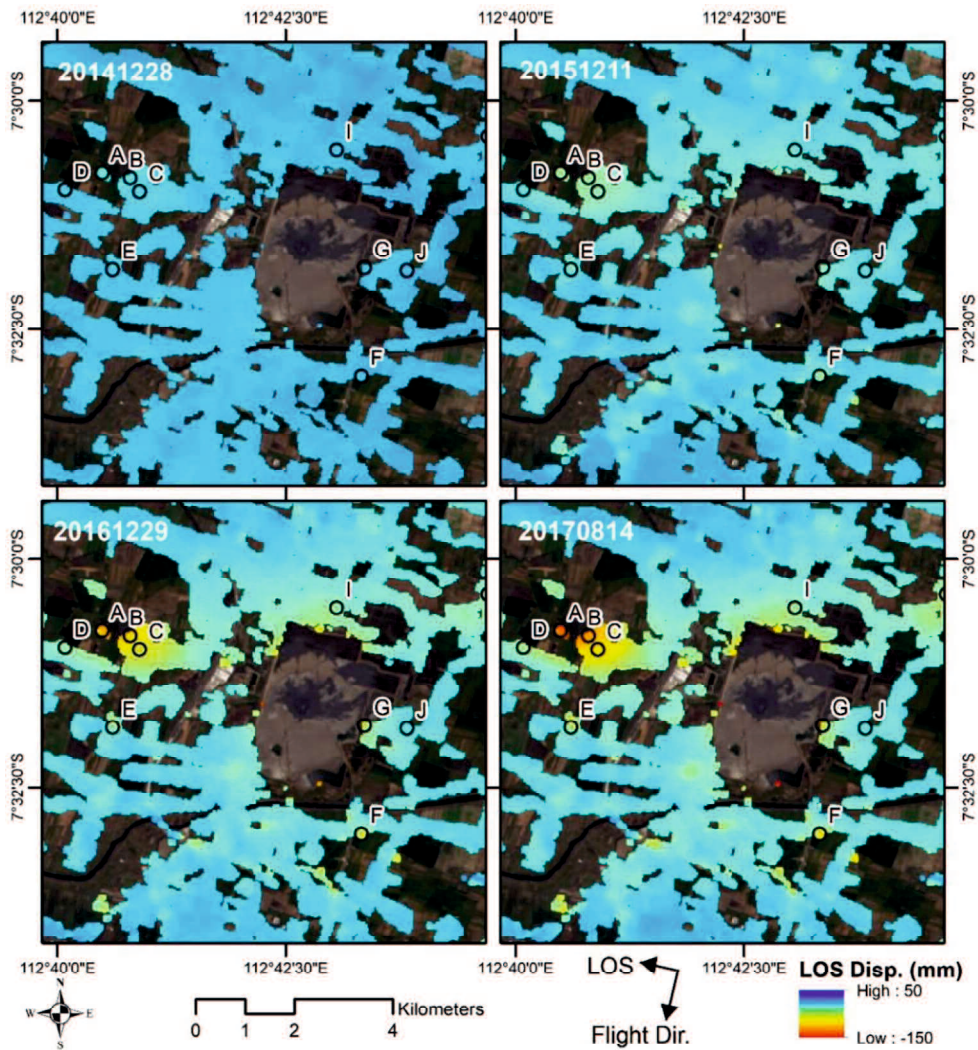
Figure 5.19 Time-series LOS displacement map in area surrounding Lusi during observation period.
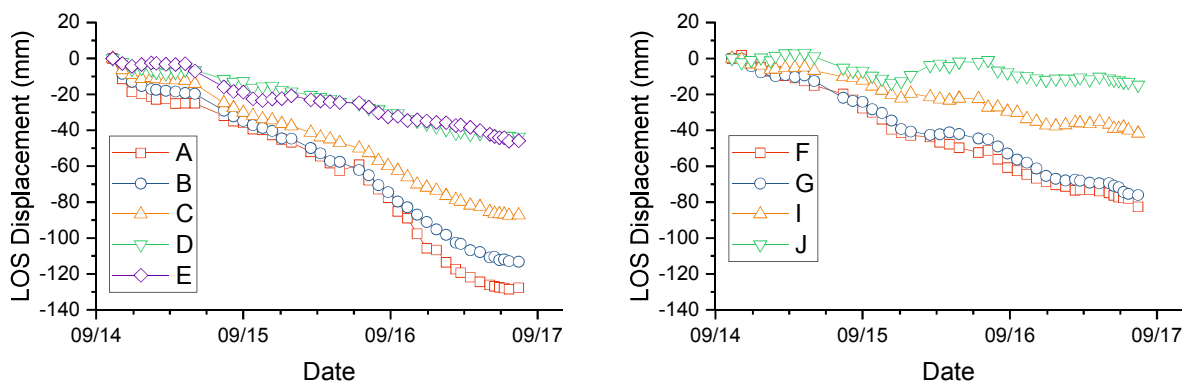
Figure 5.20 Temporal behavior of LOS displacement at interest points.

5.2.2 Landslide monitoring along Black Sea coast in Varna, Bulgaria

a. Study area
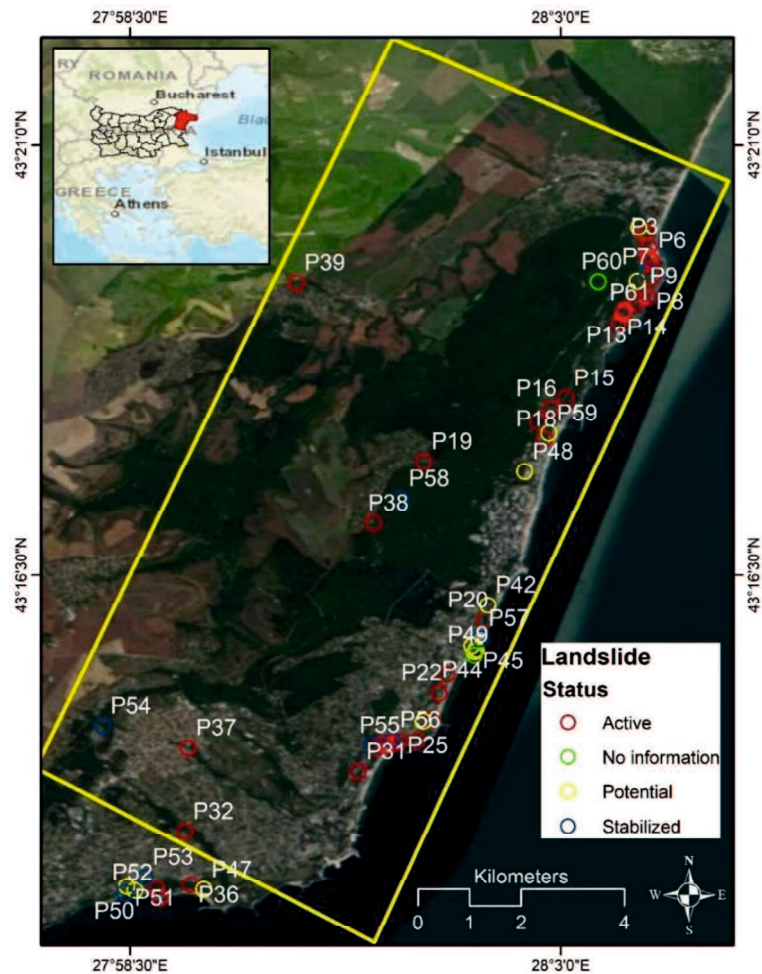
Figure 5.21 Location of landslide along Black Sea coast in Bulgaria.

The Black Sea coastal area in Bulgaria is known as a landslide area. Figure 5.21 shows the research locations of the landslide areas along the Black Sea coast between Varna and Kranevo. The active, potential, and stabilized landslide areas are marked by red, yellow, and blue circles, respectively. And the areas without any information on landslides are marked by green circles. The landslide data in this study were obtained from http://varna.geozashtita.bg/ (accessed 18 August 2018).

Since there is limited information about landslide monitoring using DInSAR for this site, it is necessary to conduct long-term monitoring using SBAS. In addition, interpreting the LOS displacement obtained over the landslide area is still challenging as there is no standard method for it. The Kranevo landslide site could be ideal for conducting research on the interpretation of LOS displacement measurements over a slope area.

b. Data collection and processing

In this study, 169 images of Sentinel-1A/B SAR data are used. They were acquired from October 2014 to August 2018 during the descending passage and in a right-looking direction (path number 36). Information on the elevation was extracted from the ALOS GDEM data. A time-series analysis is conducted by employing SBAS DInSAR. The SBAS processing is conducted twice, namely, for data collected from 2014-2016 and for that collected from 2016-2018. SBAS processing was divided into two periods because the temporal resolution during 2016-2018 was much higher than in the previous period. Therefore, it is necessary to select a different temporal baseline threshold for that period, otherwise the number of interferograms will become too large and require a great deal of computation time. The baseline tables for the two SBAS periods are presented in Figure 5.22. Details on the SBAS parameter setting can be found in appendix 3.
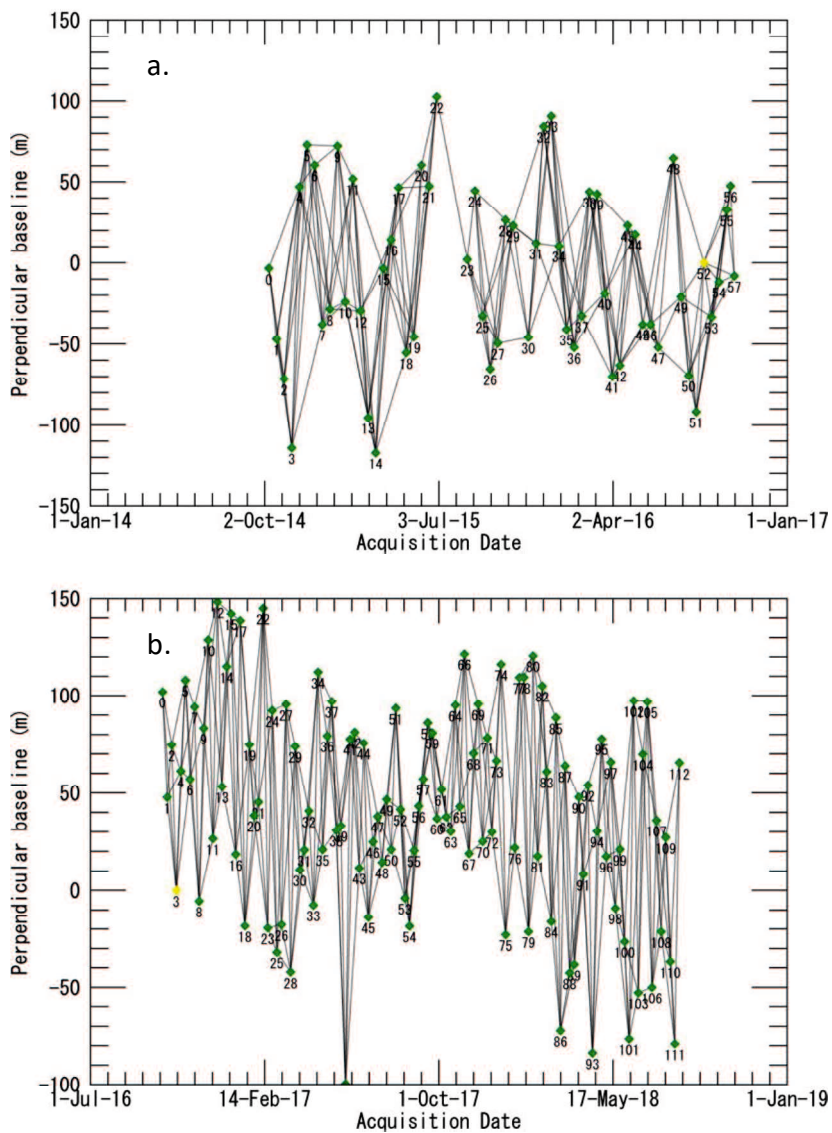
Figure 5.22 Baseline tables of SBAS DInSAR for Kranevo landslide analyses: (a) from 2014-2016 and (b) from 2016-2018.

c. Results and discussion

Figure 5.23 shows the LOS displacement evolution from the beginning to the end of the observations. Large LOS displacement was detected on the coast near Kranevo. That area is suspected of being a landslide-prone area. Positive LOS displacement means the ground surface is moving toward the satellite. In this case, the ground surface is moving toward the Black Sea since the SAR data were taken during the descending passage and in the right-looking direction.

These results are reasonable since they reflect the natural behavior of a landslide that is moving toward the toe of a hill, in this case, toward the coast of the Black Sea. For further investigation, the landslide area was divided into two areas, Kranevo and the Southern Golden Sand Beach area. Their total LOS displacements during the monitoring period are shown in Figures 5.24 and 5.25, respectively. The transitions of the LOS displacement in some landslide areas are also presented.

As can be seen from Figure 5.24, P14 has the largest LOS displacement. It has been increasing linearly since the beginning of the monitoring period. This means that the ground surface in that area is continuously sliding toward the Black Sea. At other points such as P1, P2, P3, P8, and P9, the speed of the detected ground surface movement is seen to be decreasing. This LOS displacement interpretation should be true if there is no change in the real displacement direction. The spatial distributions of the landslide areas and their transition behaviors have been presented clearly.

Very interesting LOS displacement behavior was found at the landslide area in Southern Golden Sand Beach, as seen at all points in Figure 5.25. Firstly, the LOS subsidence is negative and then turns positive. This could be caused by the changing direction of the real displacement. Thus, the projected LOS displacement also changes. The ground displacement at Southern Golden Sand Beach can be illustrated as in Figure 5.26. Firstly, the land masses move vertically, so that the LOS displacement becomes negative. Then, the land masses move horizontally, so that the LOS displacement becomes positive.
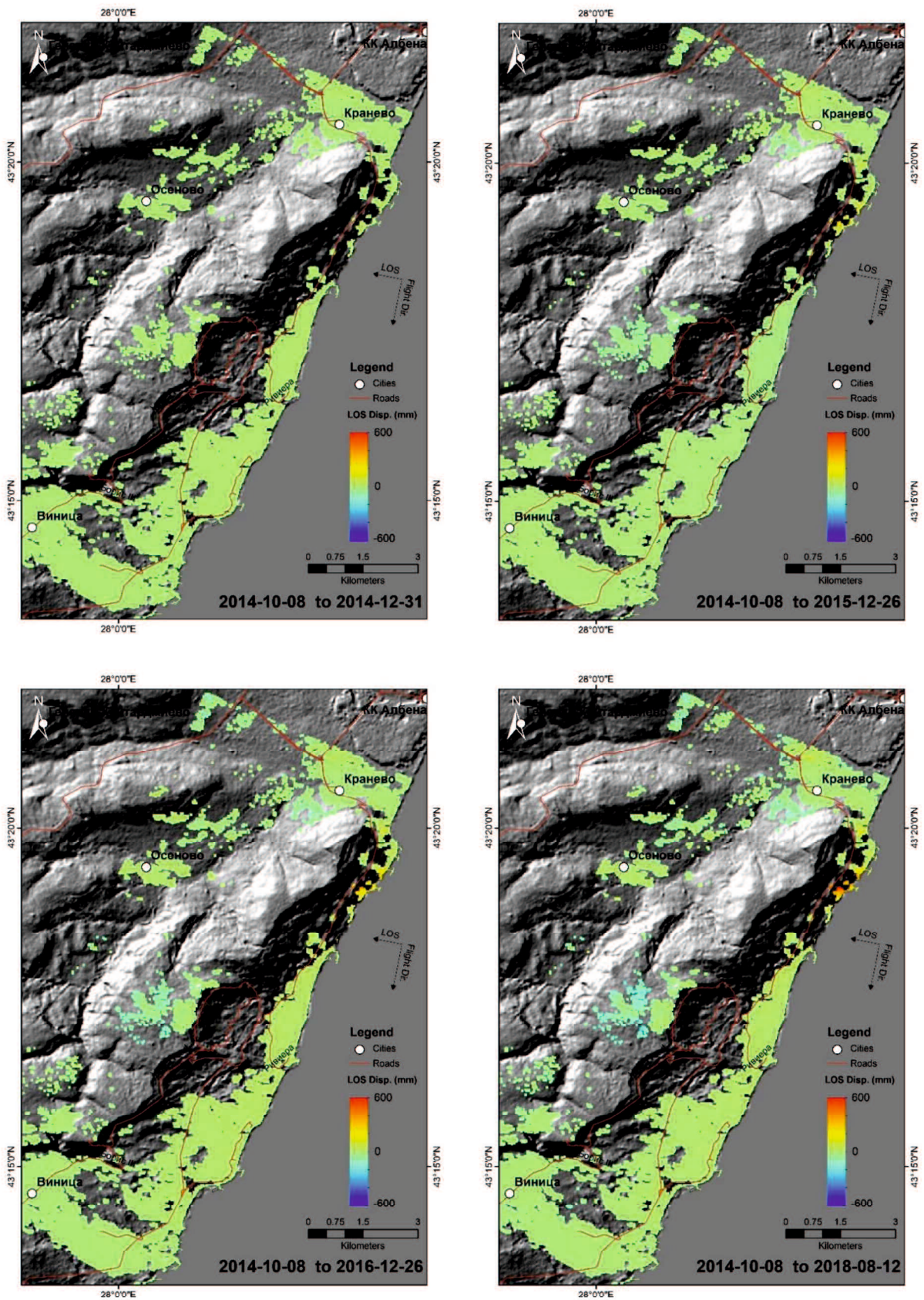
Figure 5.23 Time-series LOS displacement map for period of October 2014 to August 2018.
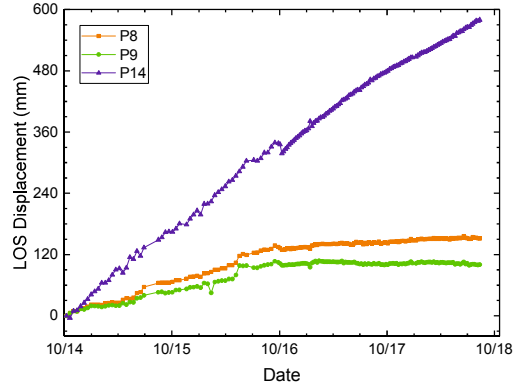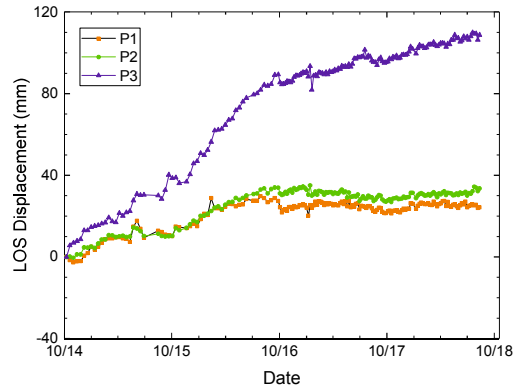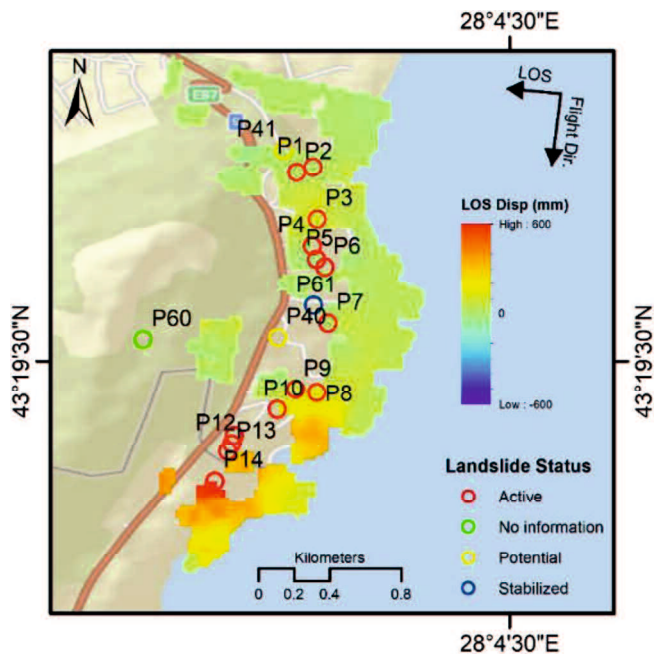
Figure 5.24 Transition of LOS displacement in Kranevo landslide area.
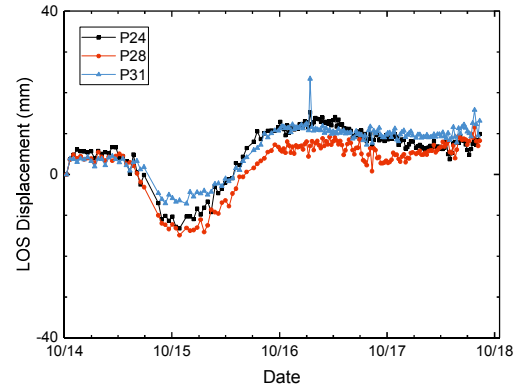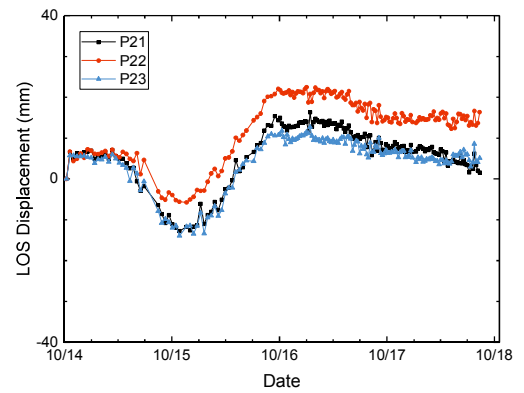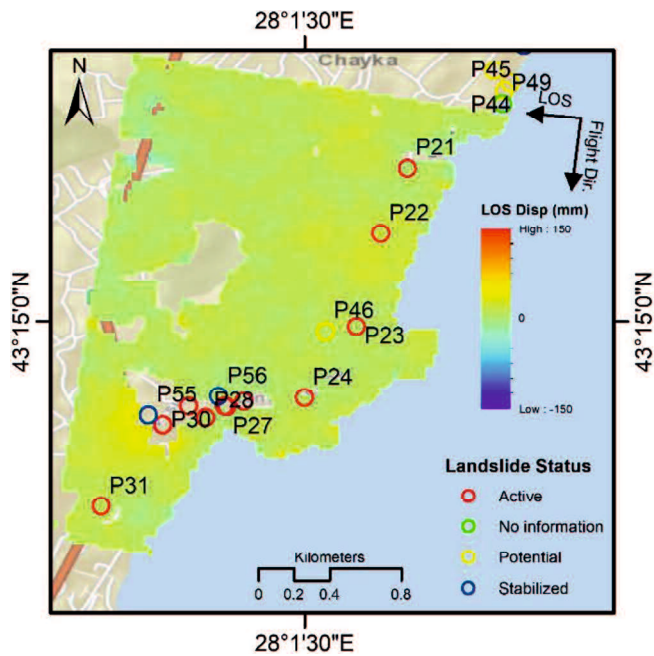
Figure 5.25 Transition of LOS displacement in Southern Golden Sand Beach.
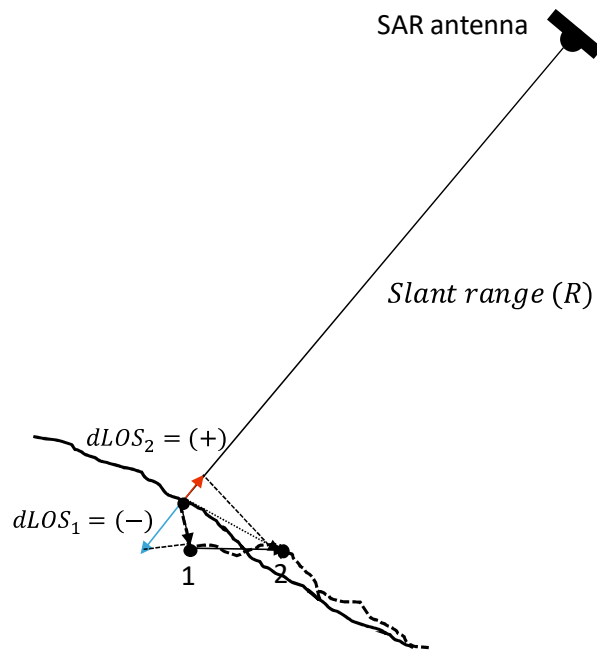
Figure 5.26 Illustration of relationship between real ground displacement and LOS displacement.

This study has been successful in utilizing SBAS for landslide monitoring. It has shown the potential of SBAS DInSAR to monitor landslide areas, especially for large slopes (few hundred meters) such as the Kranevo case. Therefore, further study for the LOS displacement interpretation should be conducted, since the geometry of each slope in question affects the projection of the real displacement along the LOS.

5.2.3 Landslide of small slope at Yabakei, Japan

a. Study area

The last study area in this chapter is the Yabakei slope. Yabakei slope is located in Oita Prefecture, Japan (Figure 5.27 (a)). A landslide is reported to have occurred there on 11 May 2018 with a length about 220 m. Yabakei slope is a steep slope covered with heavy vegetation, as shown in Figures 5.27 (b)-(c). The aim of this study is to know whether SBAS DInSAR can detect the slope behavior prior to a landslide event. The challenges for applying SBAS DInSAR at this site are its size, the steepness of the slope, and the vegetation that covers the slope.
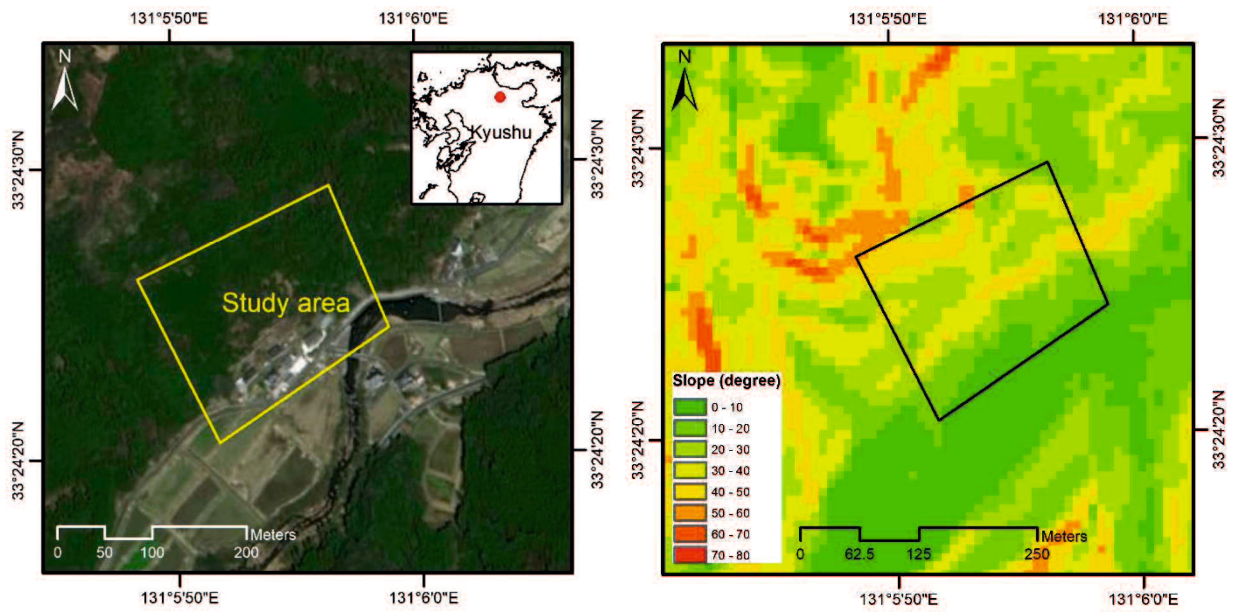
(a)   (b)

(c)

Figure 5.27 (a) Location of study area (Yabakei slope), **(b)** steepness of Yabakei slope derived from DEM data by GSI Japan, and **(c)** Google street photo of Yabakei landslide.

b. Data collection and processing
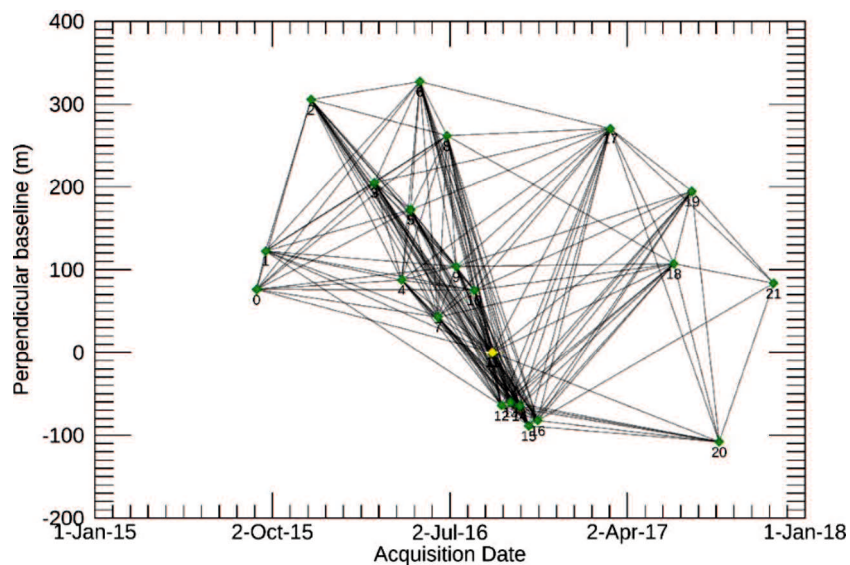
Figure 5.28 Baseline table of SBAS DInSAR for Yabakei slope.

87

To conduct the time-series analysis, 22 images of ALOS2-PALSAR2 data are used. The acquisition dates are 7 September 2015 to 13 November 2017. The SAR data were taken during the descending passage and in a right-looking direction. Details on the parameter setting for SBAS DInSAR can be found in appendix 3. Accordingly, 176 interferograms were generated. Figure 5.28 shows the baseline table of SBAS DInSAR for Yabakei slope.

c. Results and discussion
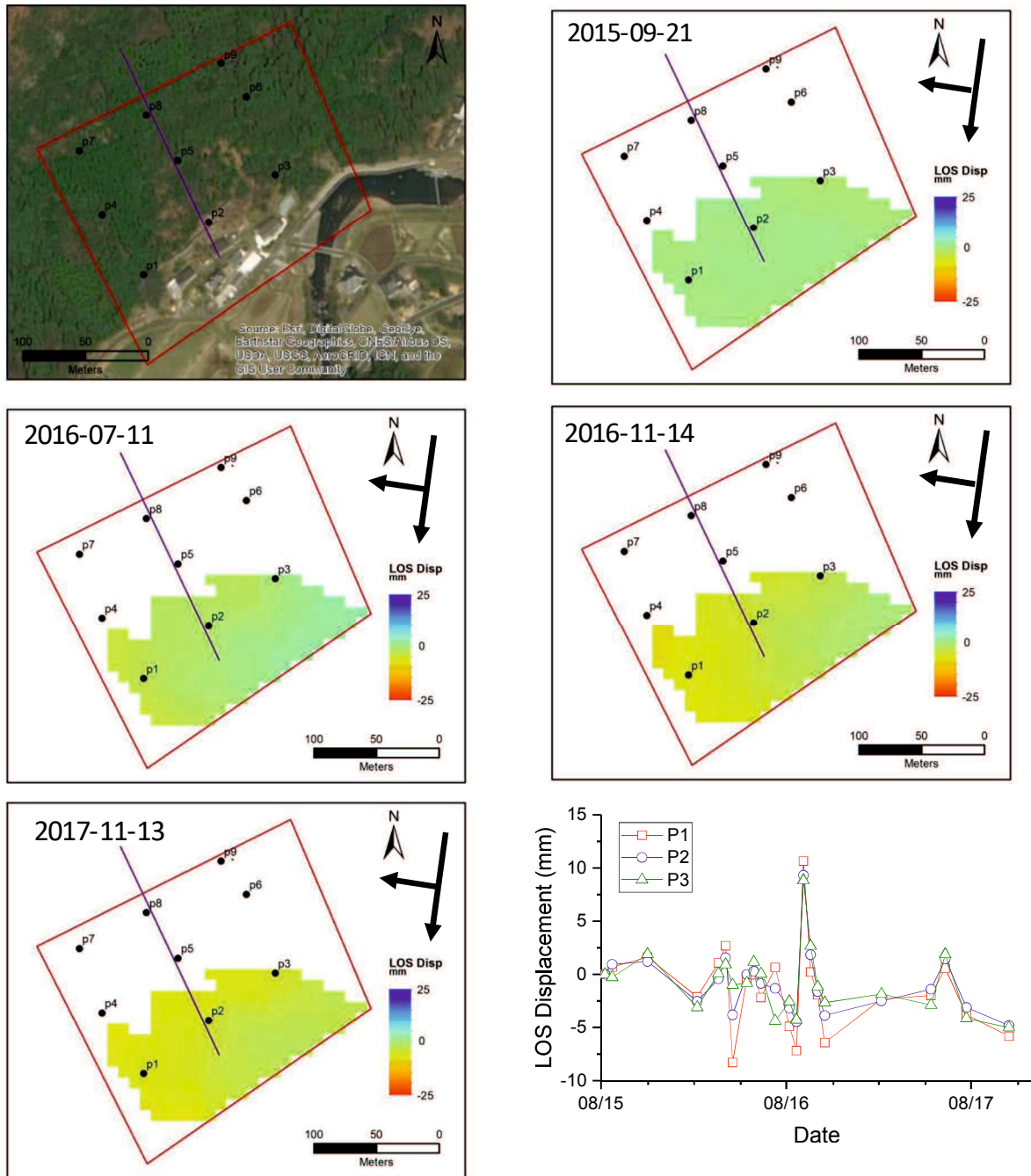
Figure 5.29 LOS displacement transition map at Yabakei slope from September 2015 to November 2017.

Figure 5.29 shows the time-series LOS displacement map and the LOS displacement transition at three points of interest. As shown in Figure 5.29, results cannot be obtained over a slope body which is highly vegetated. This condition is predictable since the InSAR coherence over a vegetated area is generally low even for L-Band SAR data. However, small displacement was detected at the toe of the slope which is less vegetated. Nine points of interest, distributed over the study area, were set. Only results at points P1, P2, and P3 were obtained. The cumulative LOS displacement at all points in each period are distributed at -10 to 10 mm. This means that SBAS DInSAR detected no remarkable displacement during the monitoring period. However, these results need to be validated against ground truth data such as GPS or other measurement results.

From these results, it is found that vegetation is the main limitation for applying SBAS DInSAR to a vegetated slope. Although the longer radar wavelength (L-Band) was used, the coherence of the SAR data cannot be preserved. In addition, SBAS DInSAR is not able to detect the behavior of small displacements (within 1 cm).

5.3 Summary for chapter 5

This chapter has demonstrated the various applications of SBAS DInSAR to six different study sites. The size of the sites varied from the large megapolitan city of Seoul, South Korea to the local slope of Yabakei, Japan. Also, the ground conditions and factors that lead to ground deformation are different for each site. This variation creates different challenges for applying SBAS DInSAR. The results of SBAS DInSAR for the city areas of Seoul, Denpasar, and Sidoarjo were found to be very useful for screening the subsidence areas over vast urban areas. This information can be used as a warning to stakeholders and help in making decisions on prevention activities.

The application of SBAS DInSAR to detect sinkholes and subsidence in an abandoned underground mining area was carried out. The study area was in Mitake, Japan. Some displaced areas were detected, but the mechanism that drove the detected displacement is still not clear. This is due to the limitation of the ground truth data. Further investigation is needed to clarify this issue.

The last two applications were for the monitoring of landslide areas. In this study, it was found that SBAS DInSAR can be useful for monitoring the large slope displacement along the Black Sea coast in Bulgaria. However, DInSAR is limited in that it only provides displacement measurements along the satellite line of sight (LOS) and the slope geometry will affect the LOS

measurement results. Therefore, further study is needed to interpret those results. In addition, the vegetation is still the main problem in the application of SBAS DInSAR. Results cannot be obtained for heavily vegetated areas, such as Yabakei slope, even when using a longer radar wavelength, such as the L-Band. However, in less vegetated areas, such as at the toe of Yabakei slope, SBAS DInSAR was able to yield results. It was found that there was no remarkable displacement prior to the slope collapse. These results need to be validated against ground truth data such as GPS or other measurement results.

Over all, from the results of these six cases, it was found that SBAS DInSAR shows good applicability if the total amount of displacement becomes larger than a few cm. In such cases, SBAS DInSAR can detect the time transition of the displacement and its distribution over the whole area. On the other hand, the application of SBAS DInSAR will be limited if the total amount of displacement is within about one cm. In this case, it is difficult to detect the behavior of that displacement. In areas with vegetation, it is difficult to obtain any results due to the low coherence of the SAR data even when the longer radar wavelength (L-Band) is used.

Since the conditions of each case are different, it is important to define the ideal parameter setting for SBAS DInSAR in each case. The number of SAR looks, the method of interferogram filtering, the window size of the filter, the method of unwrapping, and the baseline length will effect the results. Determining the ideal parameter setting of SBAS DInSAR is another issue to be addressed in a future study.

References

Aoki, Y., Sidiq, T.P., 2014. Ground deformation associated with the eruption of Lumpur Sidoarjo mud volcano, east Java, Indonesia. J. Volcanol. Geotherm. Res. 278–279, 96–102. https://doi.org/10.1016/j.jvolgeores.2014.04.012

Aydan, O., Ito, T., 2015. The effect of the depth and groundwater on the formation of sinkholes or ground subsidence associated with abandoned room and pillar lignite mines under static and dynamic conditions. Proc. Int. Assoc. Hydrol. Sci. 372, 281–284. https://doi.org/10.5194/piahs-372-281-2015

BPS, 2016. Bali Province in Figures. BPS-Statistic of Bali Province, Denpasar.

Davies, R.J., 2017. The cause of the 2006 Lusi mud volcano (Indonesia): Please let's not rewrite history. Mar. Pet. Geol. 8172. https://doi.org/10.1016/j.marpetgeo.2017.07.013

_____, 2018. http://varna.geozashtita.bg/ (accessed 18 August 2018)

Manga, M., Brumm, M., Rudolph, M.L., 2009. Earthquake triggering of mud volcanoes. Mar. Pet. Geol. 26, 1785–1798. https://doi.org/10.1016/j.marpetgeo.2009.01.019

Richards, J.R., 2011. Report into the Past, Present, and Future Social Impacts of Lumpur. Sidoarjo Rep., 162 pp.

Rudolph, M.L., Karlstrom, L., Manga, M., 2011. A prediction of the longevity of the Lusi mud eruption, Indonesia. Earth Planet. Sci. Lett. 308, 124–130. https://doi.org/10.1016/j.epsl.2011.05.037

Sawolo, N., Sutriono, E., Istadi, B.P., Darmoyo, A.B., 2009. The LUSI mud volcano triggering controversy: Was it caused by drilling? Mar. Pet. Geol. 26, 1766–1784. https://doi.org/10.1016/j.marpetgeo.2009.04.002

World Population, 2018. http://worldpopulationreview.com/countries/south-korea-population/cities/ (Accessed 5 May, 2018)

<center>**Chapter 6**</center>

<center>**Dissertation findings and conclusions**</center>

6.1 Dissertation findings and conclusions

This dissertation has dealt with the use of multi-temporal DInSAR for long-term displacement monitoring in relation to geological hazards. However, it is limited by the SAR satellite lifespan. Thus, the utilization of multi-sensor SAR data sets is necessary. Each SAR data set is processed independently, and the hyperbolic method (HM) is used to connect the unlinked results. In this way, continuous long-term subsidence monitoring can be achieved. The HM is usually used to assess the subsidence behavior in the geotechnical engineering field. By employing multi-temporal DInSAR along with the HM, this dissertation has bridged the fields of remote sensing and geotechnical engineering.

Multi-temporal DInSAR with the HM has been applied to subsidence monitoring in Semarang, Indonesia. The Small Baseline Subset (SBAS) method, which is one type of multi-temporal DInSAR, was applied to data obtained by Envisat-ASAR (2003-2007), ALOS-PALSAR (2007-2011), and Sentinel-1A (2015-2017), respectively. The validity of the results was discussed from the viewpoints of both spatial distribution and temporal transition using GPS displacement measurement results and the geological conditions of the ground. The subsidence behavior was classified into three types: (1) Type A: subsidence with an increasing rate (accelerated subsidence), (2) Type B: subsidence with a constant rate, and (3) Type C: very small subsidence. It was found that Type A and Type C are seen mainly in the north and northeast parts of the coastal area and the south and southwest parts of the hilly area. Type B is seen at the boundary between these two parts. This study verified that SBAS DInSAR with the HM can be a useful tool for long-term continuous subsidence monitoring in Semarang.

Another limitation of multi-temporal DInSAR is that the periodic behavior caused by tropospheric delays severely affects the results. This typically happens when it is applied to areas with rugged topography, such as volcanoes. To overcome this limitation, two methods have been proposed in this dissertation. Method 1 is an empirical method, while method 2 is a semi-empirical method using a physical model called the Hopfield model. Both methods were able to successfully reduce the periodic behavior. These methods were applied to the Sakurajima Volcano in Japan using Sentinel-1 SAR data taken from 2014 to 2017. It was found that both of the proposed

<center>92</center>

methods were successful in improving the multi-temporal DInSAR results. The deformation transition of Sakurajima Volcano during the monitoring period was clearly seen from the multi-temporal DInSAR results. Further study is needed to investigate the validity of the proposed methods.

Multi-temporal DInSAR i.e., SBAS DInSAR, was also applied to various sites in this dissertation. Those areas are: Seoul and its surrounding area in South Korea, Denpasar and its surrounding area in Indonesia, Mitake and its surrounding area in Japan, Sidoarjo mud flow area in Indonesia, Black Sea coast in Bulgaria, and Yabakei slope in Japan. The geotechnical issues of these areas can be categorized into two different types, namely, land subsidence and land mass movement. The results of SBAS DInSAR for city areas, such as Seoul, Denpasar, and Sidoarjo, will be very useful for screening the subsidence over vast urban areas. This information can be used as a warning to stakeholders and can help in making decisions related to prevention activities. However, SBAS DINSAR is still difficult to use for monitoring small areas of sinkholes and subsidence, for example, in Mitake, Japan.

The last two applications were for monitoring landslide areas. In this study, it was found that SBAS DInSAR can be useful for monitoring the large slope displacement along the Black Sea coast in Bulgaria. However, due the limitation of DInSAR that only provides displacement measurements along the satellite line of sight (LOS), thus slope geometry will also affect the LOS measurement results. Therefore, there is a need for further study in order to interpret those results. In addition, vegetation cover is still the main problem in the application of SBAS DInSAR. Results cannot be obtained for heavily vegetated areas, such as Yabakei slope, even when employing a longer radar wavelength such as L-Band. The issues raised in this dissertation comprise research issues and challenges to be addressed in the future.

6.2 The future role of multi-temporal DInSAR for ground deformation monitoring

Monitoring the land subsidence in Semarang and monitoring the deformation of Sakurajima Volcano should be continued using the newly proposed SAR for a better understanding of their behavior. The same procedure as that used for Semarang could be applied to monitor the long-term subsidence that is derived from the consolidation process in other cities around the world. DInSAR is a unique tool for land surface monitoring that would be useful for these purposes. As a remote sensing method, it does not require the installation of any devices on the ground. This is a great benefit of DInSAR beyond other methods in geotechnics. Furthermore,

SAR, as an active microwave sensor, can retrieve data day and night regardless of the weather conditions. These advantages make DInSAR applicable anywhere and under any conditions, such as an erupting volcano or other dangerous circumstances. Thus, the application of multi-temporal DInSAR should be extended for various cases.

However, the accuracy of multi-temporal DInSAR still needs to be improved. In particular, the correction of tropospheric delays is mandatory whenever it is applied to monitor a volcano's deformation. The development of methods for its practical use is still ongoing. In addition, several issues remain to be solved, such as those raised in chapter 5 of this dissertation. Characteristic of multi-temporal DInSAR, and particularly for SBAS DInSAR, the results for various cases need to be more closely investigated. An evaluation is needed for the effects of site geometries, ground conditions of the site, etc. The revisiting time of the SAR satellites also needs to be considered. Guidelines for the standard setting of SBAS DInSAR for each case need to be established. Therefore, there is still much work to be done.

Appendixes

Appendix 1. Photo gallery during field observation to Semarang

Field observations to Semarang have been conducted in March and August 2017. The aims are to know the present situation and effects of the subsidence, how the local community adapt to subsidence, and to know the ground condition of GPS point. The observation track is presented in Figure A1.2. Some photos were taken and presents in Figures A1.1 and A1-3. The sky photos at several GPS antennas' overhead are also taken and presents in Figure A1.4.

Figure A1.1 Photographs taken during first field observation in March 2017.

Figure A1.2 Second observation track during August 2017 superimposed on Google Earth.

Figure A1.3 Photographs taken during second field observation in August 2017, GPS campaign was being conducted by the colleagues during those dates.

| DRI1 | RMPA | CTRM | PMAS |

| BM05 | BM11 | MTIM | PRPP |
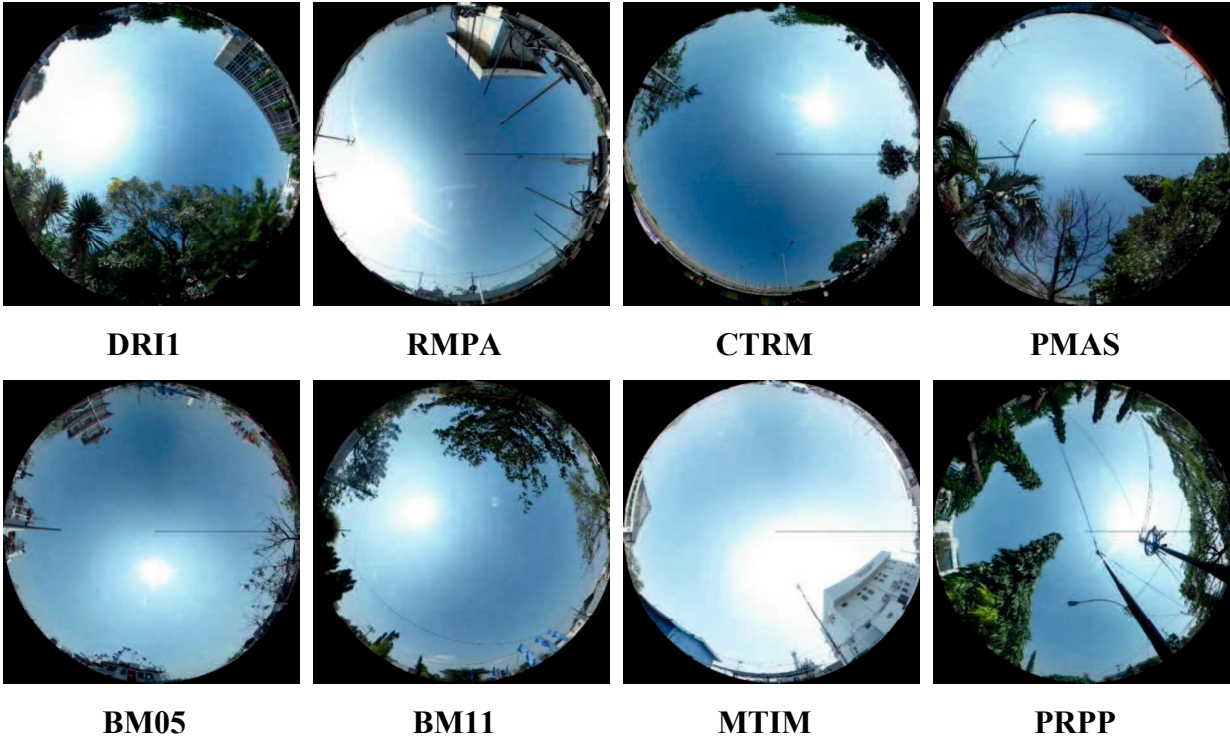
Figure A1.4 Sky photos at several GPS points as taken in August 2017 using theta camera.

Appendix 2. Photo gallery during field observation to Sakurajima Volcano

The field observation to Sakurajima Volcano was conducted on 18 September 2018, with the purposes to know the real ground condition of Sakurajima Volcano and seeking for a collaboration for the future research.
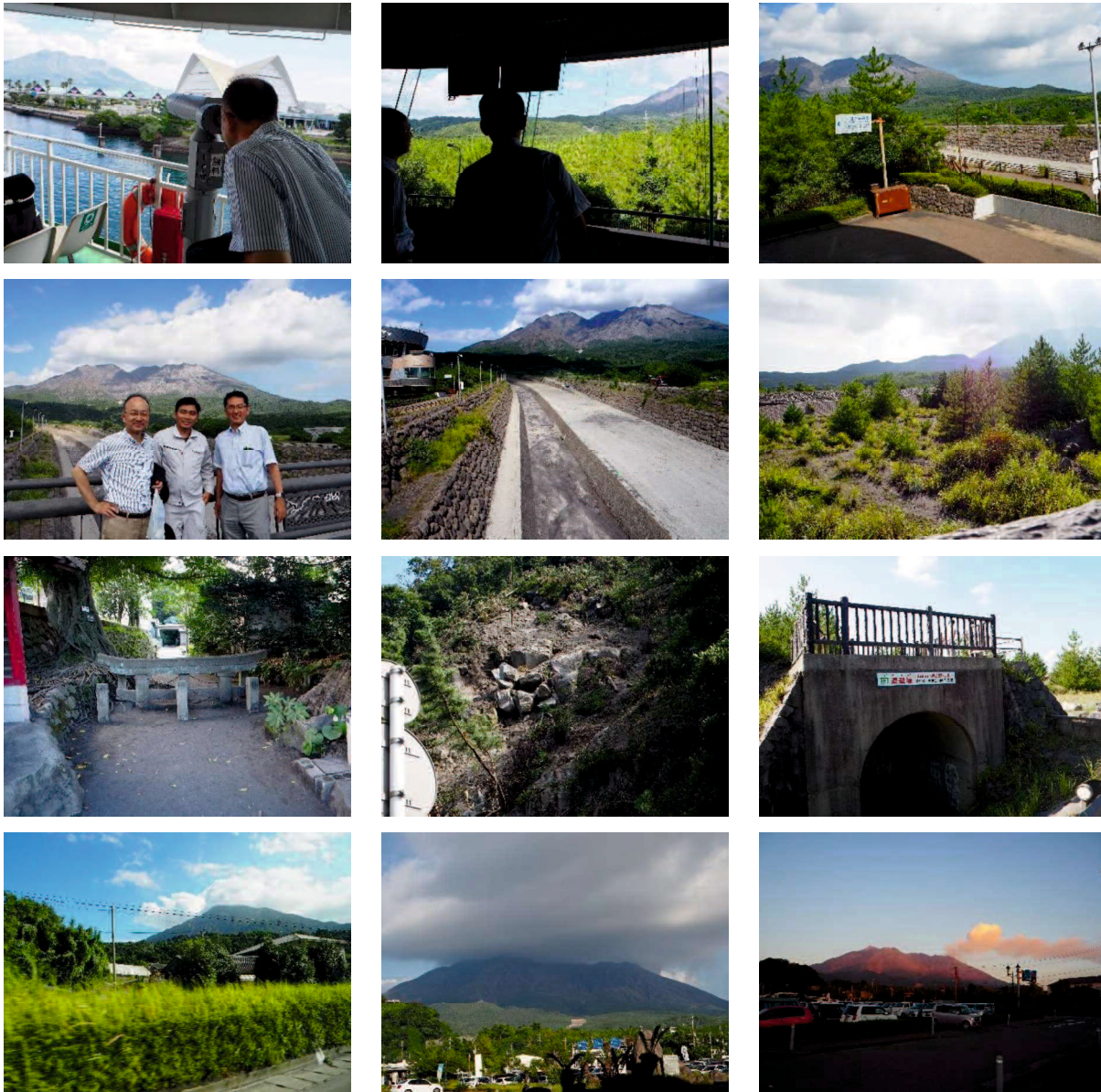
Figure A2.1 Photos around the Sakurajima Volcano taken during 18 September 2018.

Appendix 3. SBAS processing parameters setting

Table A3.1 The parameters setting for SBAS processing of each case.

Parameter	Seoul	Denpasar	Mitake	Lusi	Kranevo (2014-2016)	Kranevo (2016-2018)	Yabakei
	Setting	Setting	Setting	Setting	Setting	Setting	Setting
Allowed Max Perp. baseline	20% of Bc	45% of Bc	45% of Bc	45% of Bc	20% of Bc	20% of Bc	45% of Bc
Allowed Max Temp. baseline	120 days	100 days	120 days	100 days	48 days	18 days	365 days
Range looks	5	5	5	5	5	5	4
Azimuth looks	1	1	1	1	1	1	4
Filtering method	Goldstein	Goldstein	Goldstein	Goldstein	Goldstein	Goldstein	Goldstein
Unwrapping method	MCF	MCF	MCF	MCF	MCF	MCF	MCF
Unwrapping coherence threshold	0.25	0.2	0.2	0.25	0.2	0.2	0.2
Refinement method	Residual Phase	Residual Phase	Residual Phase	Residual Phase	Residual Phase	Residual Phase	Residual Phase
Phase poly degree	3	3	3	3	3	3	3
Displacement model	Linear	Linear	Linear	Linear	Linear	Linear	Linear
Atmosphere low pass size	1200 m	1200 m	1200 m	1200 m	1200 m	1200 m	1200 m
Atmosphere high pass size	365 days	365 days	365 days	365 days	365 days	365 days	365 days
Final product coherence threshold	0.4	0.4	0.4	0.4	0.4	0.4	0.25
Final spatial resolution	25m x 25m	25m x 25m	25m x 25m	25m x 25m	25m x 25m	25m x 25m	10m x 10m
Number of interferogram to analyze	91	100	512	150	256	330	176
Max absolute Perp. baseline found	128.3m	232.5m	171m	205m	186.8	194.7	415.8
Max absolute Temp. baseline found	120 days	96 days	120 days	100 days	48 days	18 days	365 days

Appendix 4. List of SAR data used in this dissertation

Sakurajima	: Sentinel-1, path 163
Seoul	: Sentinel-1, path 127
Bali	: Sentinel-1, path 156
Mitake	: Sentinel-1, path 112
Lusi	: Sentinel-1, path 3
Kranevo	: Sentinel-1, path 36
Yabakei	: ALOS2-PALSAR2, path 23, frame 2940

Table A4.1 List of the acquisition date of all SAR data used in the studies.

No	Acquisition date							
	Sakurajima	**Seoul**	**Bali**	**Mitake**	**LUSI**	**Kranevo**	**Kranevo (Continued)**	**Yabakei**
1	11/21/2014	10/26/2014	10/16/2014	5/5/2015	11/10/2014	10/8/2014	3/8/2017	9/7/2015
2	12/3/2014	12/13/2014	10/28/2014	5/29/2015	12/4/2014	10/20/2014	3/14/2017	9/21/2015
3	12/15/2014	1/6/2015	11/21/2014	6/22/2015	12/28/2014	11/1/2014	3/20/2017	11/30/2015
4	12/27/2014	1/30/2015	12/15/2014	7/16/2015	1/21/2015	11/13/2014	3/26/2017	3/7/2016
5	1/8/2015	2/23/2015	1/8/2015	8/9/2015	2/14/2015	11/25/2014	4/1/2017	4/18/2016
6	1/20/2015	3/19/2015	2/25/2015	9/2/2015	2/26/2015	12/7/2014	4/7/2017	5/2/2016
7	2/13/2015	4/12/2015	3/21/2015	9/26/2015	3/22/2015	12/19/2014	4/13/2017	5/16/2016
8	2/25/2015	6/23/2015	5/8/2015	10/20/2015	4/15/2015	12/31/2014	4/19/2017	6/13/2016
9	3/9/2015	7/17/2015	6/1/2015	11/13/2015	5/9/2015	1/12/2015	4/25/2017	6/27/2016
10	3/21/2015	9/3/2015	6/25/2015	12/7/2015	6/2/2015	1/24/2015	5/1/2017	7/11/2016
11	4/2/2015	9/27/2015	7/19/2015	12/31/2015	8/13/2015	2/5/2015	5/7/2017	8/8/2016
12	4/14/2015	10/21/2015	8/12/2015	1/24/2016	9/6/2015	2/17/2015	5/13/2017	9/5/2016
13	4/26/2015	11/14/2015	9/29/2015	2/17/2016	9/30/2015	3/1/2015	5/19/2017	9/19/2016
14	5/20/2015	12/8/2015	10/23/2015	3/12/2016	10/24/2015	3/13/2015	5/25/2017	10/3/2016
15	6/13/2015	1/1/2016	11/16/2015	4/5/2016	11/17/2015	3/25/2015	5/31/2017	10/17/2016
16	7/7/2015	2/18/2016	1/3/2016	4/29/2016	12/11/2015	4/6/2015	6/6/2017	10/31/2016
17	7/31/2015	4/6/2016	1/27/2016	5/23/2016	1/4/2016	4/18/2015	6/12/2017	11/14/2016
18	8/24/2015	4/30/2016	2/20/2016	8/3/2016	1/28/2016	4/30/2015	6/18/2017	3/6/2017
19	9/17/2015	7/11/2016	4/8/2016	8/27/2016	3/16/2016	5/12/2015	6/24/2017	6/12/2017
20	10/11/2015	8/4/2016	5/2/2016	9/20/2016	4/9/2016	5/24/2015	6/30/2017	7/10/2017
21	11/4/2015	10/15/2016	5/26/2016	10/14/2016	5/3/2016	6/5/2015	7/6/2017	8/21/2017
22	11/28/2015	11/8/2016	7/13/2016	11/7/2016	5/27/2016	6/17/2015	7/12/2017	11/13/2017
23	12/22/2015	12/26/2016	8/6/2016	11/13/2016	7/14/2016	6/29/2015	7/18/2017	
24	1/15/2016	2/24/2017	10/17/2016	11/25/2016	8/7/2016	8/16/2015	7/24/2017	
25	2/8/2016	3/8/2017	11/10/2016	12/7/2016	8/31/2016	8/28/2015	7/30/2017	
26	3/3/2016	3/20/2017	12/28/2016	12/19/2016	9/24/2016	9/9/2015	8/5/2017	

Table A4.1 (Continued)

27	3/27/2016	4/13/2017	1/21/2017	12/31/2016	10/18/2016	9/21/2015	8/11/2017
28	4/20/2016	4/25/2017	2/26/2017	1/12/2017	11/11/2016	10/3/2015	8/17/2017
29	5/14/2016	5/19/2017	3/22/2017	1/24/2017	12/5/2016	10/15/2015	8/23/2017
30	6/7/2016		4/15/2017	2/5/2017	12/29/2016	10/27/2015	8/29/2017
31	7/1/2016		5/9/2017	2/17/2017	1/22/2017	11/20/2015	9/4/2017
32	7/25/2016		6/2/2017	3/1/2017	2/15/2017	12/2/2015	9/10/2017
33	8/18/2016		6/26/2017	3/13/2017	3/11/2017	12/14/2015	9/16/2017
34	9/11/2016		7/20/2017	3/25/2017	3/23/2017	12/26/2015	9/22/2017
35	10/5/2016		8/13/2017	4/6/2017	4/16/2017	1/7/2016	9/28/2017
36	10/29/2016			4/18/2017	5/10/2017	1/19/2016	10/4/2017
37	11/22/2016			4/30/2017	6/3/2017	1/31/2016	10/10/2017
38	12/16/2016			5/24/2017	6/15/2017	2/12/2016	10/16/2017
39	1/9/2017			6/5/2017	6/27/2017	2/24/2016	10/22/2017
40	2/26/2017			6/17/2017	7/9/2017	3/7/2016	10/28/2017
41	3/10/2017			6/29/2017	7/21/2017	3/19/2016	11/3/2017
42	3/22/2017			7/11/2017	8/14/2017	3/31/2016	11/9/2017
43	4/3/2017			7/23/2017		4/12/2016	11/15/2017
44	4/15/2017			8/4/2017		4/24/2016	11/21/2017
45	4/27/2017			8/16/2017		5/6/2016	11/27/2017
46	5/9/2017			8/28/2017		5/18/2016	12/3/2017
47	5/21/2017			9/21/2017		5/30/2016	12/9/2017
48	6/2/2017			10/3/2017		6/11/2016	12/15/2017
49	6/14/2017			10/15/2017		7/5/2016	12/21/2017
50	6/26/2017			10/27/2017		7/17/2016	12/27/2017
51	7/8/2017			11/8/2017		7/29/2016	1/8/2018
52	7/20/2017			11/20/2017		8/10/2016	1/14/2018
53	8/1/2017			12/2/2017		8/22/2016	1/20/2018
54	8/13/2017			12/14/2017		9/3/2016	1/26/2018
55	8/25/2017			12/26/2017		9/15/2016	2/1/2018
56				1/7/2018		9/27/2016	2/7/2018
57				1/19/2018		10/3/2016	2/13/2018
58				1/31/2018		10/9/2016	2/19/2018
59				2/12/2018		10/15/2016	2/25/2018
60				2/24/2018		10/21/2016	3/3/2018
61				3/8/2018		10/27/2016	3/9/2018
62				3/20/2018		11/2/2016	3/15/2018
63				4/1/2018		11/8/2016	3/21/2018
64				4/13/2018		11/14/2016	3/27/2018
65				4/25/2018		11/20/2016	4/2/2018
66				5/7/2018		11/26/2016	4/8/2018
67				5/19/2018		12/2/2016	4/14/2018
68				5/31/2018		12/8/2016	4/20/2018
69				6/12/2018		12/14/2016	4/26/2018
70						12/20/2016	5/2/2018
71						12/26/2016	5/8/2018

Table A4.1 (Continued)

72					1/1/2017	5/14/2018	
73					1/7/2017	5/20/2018	
74					1/13/2017	5/26/2018	
75					1/19/2017	6/1/2018	
76					1/25/2017	6/7/2018	
77					1/31/2017	6/13/2018	
78					2/6/2017	6/19/2018	
79					2/12/2017	6/25/2018	
80					2/18/2017	7/1/2018	
81					2/24/2017	7/7/2018	
82					3/2/2017	7/13/2018	
83						7/19/2018	
84						7/25/2018	
85						7/31/2018	
86						8/6/2018	
87						8/12/2018	